# The Behaviour of Bed Ripples on Sheltered Beaches

Master Thesis


| | |
|---|---|
| Floris van Dijk | 4672399 |


| Committee Members | Role |
|---|---|
| Matthieu de Schipper | Chair |
| Marlies van der Lugt | Daily Supervisor |
| Claire Chassagne | Independent Supervisor |

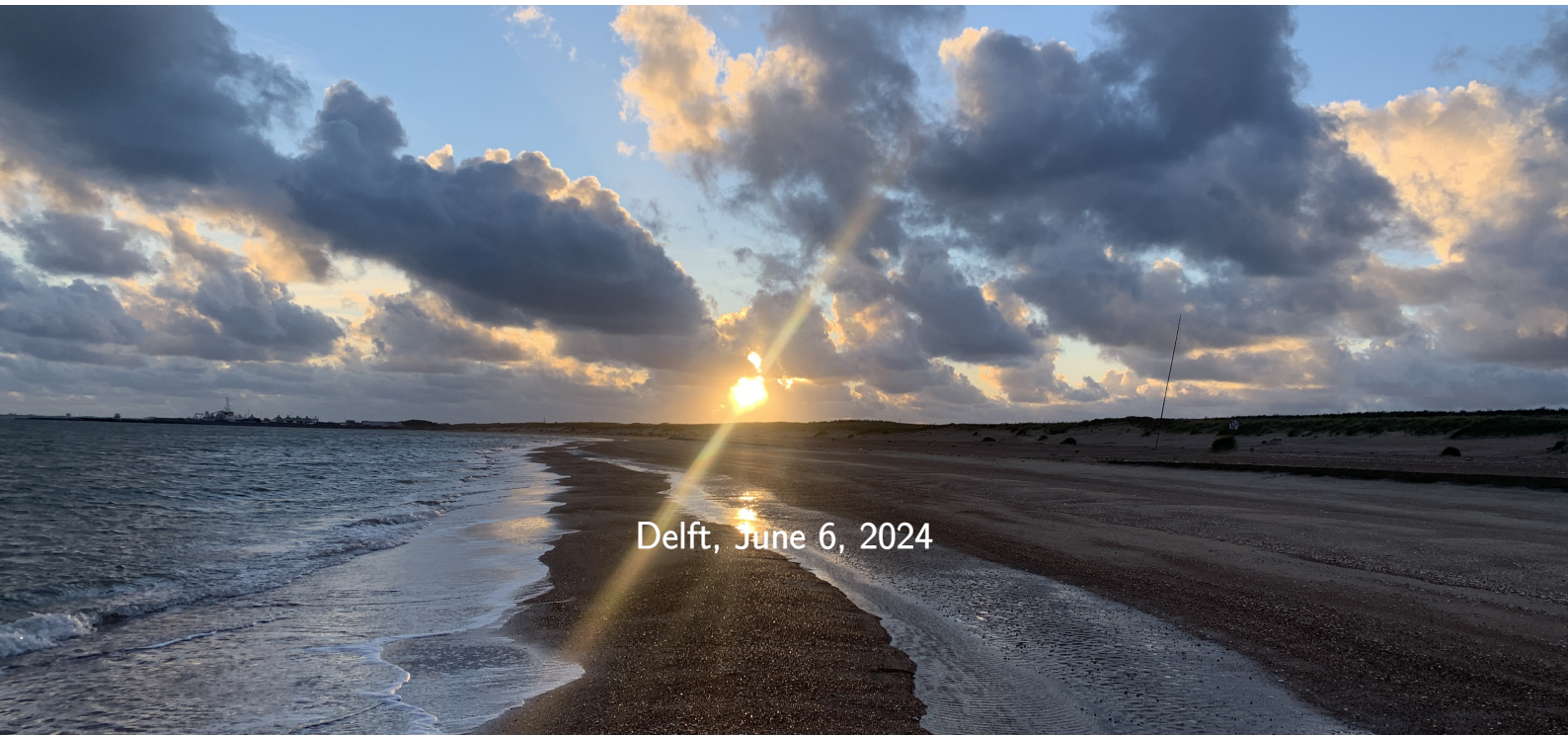

Delft, June 6, 2024

# Acknowledgements

The document before you is the culmination of a master thesis project that took almost nine months. Before reading, I would like to express my gratitude towards my supervisors: Matthieu de Schipper, Marlies van der Lugt and Claire Chassagne. You have been essential in the completion of my master's thesis and the reason that I can look back on a joyful period of my study. I would especially like to thank Marlies for her close support. Your door was always open and our weekly coffee meetings helped a lot in keeping me motivated and on track.

# Contents

# List of Abbreviations

## Symbols

$As$ wave asymmetry. 24

$H_{m_0}$ significant wave height. 24

$S_b$ bed load transport. 3

$S_s$ suspended transport. 3

$S_{mig}$ migration distance. 27

$Sk$ wave skewness. 24

$T_{m_{01}}$ mean period. 24

$Ur$ Ursell number. 24

$V_{mig}$ migration rate. 27, 28

$\bar{u}_w$ average absolute orbital velocity. 24

$\delta_{x_b}$ phase offset between the bedform shape and the function for transport. 28

$\epsilon$ bed porosity factor. 28

$\eta$ ripple wave height. 25, 26, 28

$\lambda$ ripple wave length. 25, 28

$\phi_c$ current direction. 23

$\phi_{mig}$ migration direction. 27

$\phi_r$ ripple crest orientation. 25

$\psi$ mobility parameter. 6

$a$ the amplitude of the velocity at the waterline. 24

$d$ water depth. 24

$f_r$ dimensionless ripple shape factor. 28

$k$ wave number. 24

$q_b$ sediment flux. 28

$u$ cross-shore velocity. 23

$u_c$ current velocity. 4, 23

$u_w$ wave-orbital velocity. 4, 24

$u_{w;max}$ $90^{\text{th}}$-percentile orbital velocity. 24

$u_{w;rms}$ root-mean square orbital velocity. 24

$v$ long-shore velocity. 23

$x_b$ position along the bedform wavelength. 28

**2DFFT** Two-Dimensional Fast Fourier Transformation. 25

**A**

**ADV** Acoustic Doppler Velocimeter. 15, 16, 18, 19, 23–25, 28, 29, 57

**D**

**D50** median sediment grain size. 12, 15, 56

**K**

**KO** Khelifa and Ouellet (2000). 10, 12, 43–45, 50, 51, 54

**O**

**OD** O'Donoghue et al. (2006). 10, 12, 43, 44, 50, 51, 54, 55

**P**

**PHZD** Prins Hendrikzanddijk. 14, 52

**R**

**RMSE** root-mean-square error. 26, 43, 44, 50, 54

**S**

**SRPLS** Sand Ripple Profiling Logging Sonar. 2, 15–19, 22, 23, 25, 29, 33–35, 41, 49–51, 56, 57

**V**

**VR** Van Rijn (2007). 10, 12, 43, 44, 50, 51, 54

# 1 | Abstract

Over the past decades, the majority of research into coastal development has been carried out with a focus on open-sea beaches. However, sheltered beaches make up a larger part of the coastlines in the world. Recent studies have shown that the system of sheltered beaches cannot be approached as an open-sea beach with a lower wave energy climate. Doing so results in an inaccurate coastline development prediction. Understanding sheltered beaches and their coastline development is vital because the stresses on these beaches worldwide will increase due to climate change.

Due to the lower energetic wave climate, bed ripples are expected more often on sheltered beaches than on open-sea beaches. The possible presence of these is not yet incorporated in current models. Bed ripples can affect the sediment transport along the coast and can therefore have a substantial role in the necessary understanding of the different coastline development of sheltered beaches with respect to other beaches. Fieldwork data from the Prins Hendrikzanddijk was used to research the behavior of ripples on sheltered beaches. The research was divided into three categories: the formation and existence of ripples under varying hydrodynamic conditions, the performance of current ripple prediction formulas, and ripple migration-induced sediment transport.

Ripples were present with varying heights of 0.023 to 0.078 meters and wavelengths of 0.091 to 0.275 meters and the ripple dimensions responded to the changes in forcing on the sheltered beach. The parameter that related the best to the ripple dimensions was a mobility number that used the $98^{th}$-percentile wave-orbital velocity and not a current-related velocity part.

Three ripple predictors were used, of which the predictor by O'Donoghue et al. (2006) performed the best. This predictor relates hydrodynamic conditions to a representing ripple height and wavelength, allowing for changing dimensions and varying hydrodynamic forcing. However, this suggests a strong relation between the hydrodynamic conditions and the dimensions of the ripples. Overall, no strong correlation was visible between measured ripple dimensions and the mobility parameter. This supports the usage of the ripple predictor by Van Rijn (2007), which uses a constant ripple height until conditions become too energetic. This approach performs similarly to the best-performing predictor and could be more stable during varying conditions.

Lastly, ripple migration was measured and was shown to be driven by wave skewness and asymmetry. Both on- and offshore migrating ripples were measured. The source of either on- or offshore migration was not identified clearly. However, the offshore migrating ripples were accompanied by lower skewness and smaller asymmetry values than the onshore migrating ripples. The order of magnitude of the induced bedload transport by migrating ripples was of the same order as bedload transport predicted by the model XBeach without the inclusion of the existence of ripples.

# 2 | Introduction

Coastline development is predicted using models that calculate water flow and sediment fluxes over the domain. To predict these fluxes, the model uses the wave statistics of the area where the domain is located and various other variables such as sediment conditions. Recent studies on sheltered beaches have shown that the behavior of this beach type is different compared to normal beaches and that the models could not predict the correct cross-sectional development (McCall et al., 2018). A sheltered beach is a beach that is protected from ocean waves that arrive directly at the shore, and where the fetch for wind-generated waves is limited. The sheltered nature of these beaches leads to less energetic waves during storm conditions (Vila-Concejo et al., 2020). The incapability of the model results for sheltered beaches could lie in the presence of bed ripples during storm conditions and the effect they have on the sediment transport in the domain. Bed ripples are a bed form of the spatial order of $10^0 - 10^1$ centimeters in height (Bosboom & Stive, 2023). On normal beaches, the ripples are expected to be washed away by very energetic waves during storms. However, due to the less energetic conditions on sheltered beaches, bed ripples can be present during storms and will influence bed roughness and bed load sediment transport. The ripples induce turbulent vortexes that can bring additional sediment into suspension and provide for a bed load sediment transport mechanism, where higher onshore velocities can transport grains of sediment over the ripple crests, but the lower offshore velocities are incapable of doing the same. To incorporate the effect of ripples in a model, it can use prediction formulas to calculate the dimensions of the ripples. Models do not however always incorporate the influence of ripples and when they do, a faulty production of the dimensions could lead to larger or smaller effects of the ripples. The error in the model's cross-section prediction could therefore be caused by: a wrong prediction of the roughness caused by ripples, the existence or non-existence of these ripples and assuming otherwise, or a sediment transport inside these ripples that is not accounted for.

This report focuses on these ripple predictors and the migration of ripples. The goal is to test the accuracy of the ripple predictors by creating a dataset of bed ripples and hydrodynamic conditions and comparing these with predicted ripple dimensions during these conditions. Also, the migration and associated sediment transport in the ripples in investigated to see what the contribution of ripple sediment transport is.

The main research question for this research is:

"What is the behavior of bed ripples on sheltered beaches?"

This is guided by the following research questions:

- Under which conditions do ripples appear at sheltered beaches and what are the dimensions?
- How accurate are existing ripple predictors for the wave-current regime at sheltered beaches?
- What are the migration velocities and associated sediment transport rates of ripples on sheltered beaches?

This report will start with background information on sheltered beaches, bed ripples, and the modeling of coastline development in chapter 3. After that, the methods used to gather, process, and analyze the data are explained. This is followed by chapter 5, showing the results of data gathering and processing. Then, chapter 6 analyzes the results to answer the three research questions. The analysis is followed by the discussion in chapter 7. Chapter 8 answers the three research questions. At last, recommendations are made for future research in chapter 9.

# 3 | Background

To design coastline interventions, models that predict coastline development are needed. Models like Delft3D and XBeach (Roelvink et al., 2010) use hydrodynamic statistics to compute the response of a coastline. The model calculates flow patterns and sediment fluxes over the domain to predict erosion and accretion. Recent studies on sheltered beaches have shown that the model cannot accurately predict shoreline behavior for that beach type (McCall et al., 2018). This chapter, explains the presence of bed ripples, the definition of sheltered beaches, and gives a deeper look at recent research on a sheltered beach, before explaining why this research is useful.

## 3.1 | Sediment transport

### General

Morphological change of a coastline is driven by sediment transport, that either causes erosion or accretion (Bosboom & Stive, 2023). Sediment transport over the water column is divided into bed load transport ($S_b$) and suspended transport ($S_s$). Bed load transport consists of sand particles that roll over the bed and are limited to the boundary layer. The boundary layer is a small layer of turbulence above the bed, and below flow above that follows a logarithmic flow distribution. Suspended transport consists of particles elevated in the water column above the boundary layer. The buoyancy of these particles and forcing by the flow velocity are enough to keep the particles in suspension (Bosboom & Stive, 2023). The two sediment components can be expressed as a flow velocity that transports water with a certain sediment concentration, $C$. The flow velocity and sediment concentration are depended on the water depth. The general distributions of the velocity and concentration with respect to the water depth are shown in figure 3.1 below.

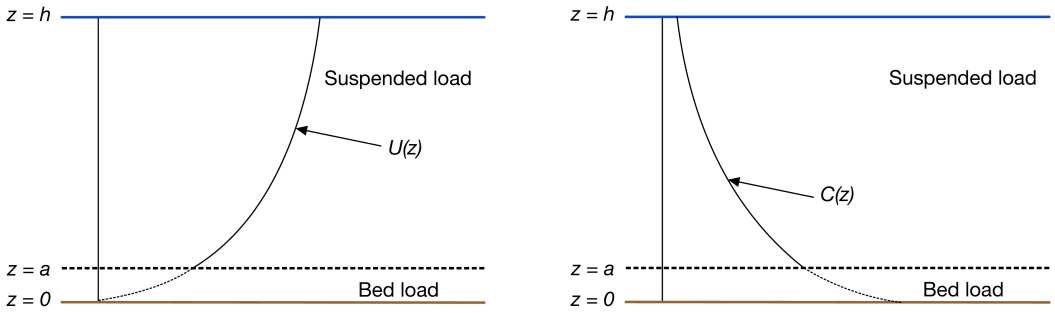


**(a)** Logarithmic flow distribution over the water column, based on (Bosboom & Stive, 2023).

**(b)** Distribution of the sediment concentration over the water column, based on (Bosboom & Stive, 2023).

**Figure 3.1:** Distribution of flow velocity and sediment concentration.

Here, the height of the boundary layer is shown at an elevation of $a$ above the bed. Due to the bottom friction, the flow is smaller closer to the bed than it is near the surface. The profile that it follows is a logarithmic distribution. The concentration is distributed the other way around. The concentration is higher closer to the bed since this is where sediment is brought into suspension from the boundary layer into the suspended load layer above. The total sediment transport can be defined as a product of these two components:

$$S = U(z)C(z) = S_b + S_s \tag{3.1}$$

Their combined distribution over the water depth is depicted in the following figure:

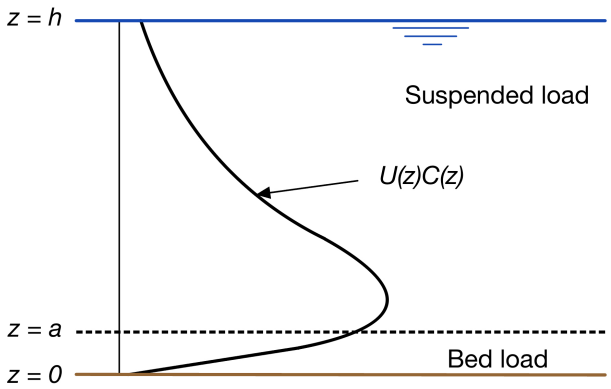


**Figure 3.2:** Bed load and suspended sediment transport over the water column (Bosboom & Stive, 2023).

The height of the boundary layer is not the same in all circumstances. It is dependent on the roughness of the bed. The thickness of the boundary layer is usually in the same order as the bed roughness. The bed roughness is determined using the sediment particle size, type, and bedforms that are present on the bottom. This is discussed in the next paragraph.
In the literature, there are several formulas for the two sediment components. The formulas predict the sediment transport rates using the hydrodynamic and soil conditions of the specific site. In general, for stationary flow over a smooth bottom, the following relations between flow velocity and Sediment transport hold (Bosboom & Stive, 2023):

$$\langle S_b \rangle \propto \langle u|u|^2 \rangle \tag{3.2}$$

$$\langle S_s \rangle \propto \langle u|u|^3 \rangle \tag{3.3}$$

$$\tag{3.4}$$

Here the brackets around the variables indicate time-averaging. The formulas state that the time-averaged sediment transport is proportional to the time-averaged flow velocity to a certain power. A higher flow velocity will yield a larger sediment transport.

### Coastal sediment transport

Near the coast, however, flow is not stationary. The flow consists of two components: the current velocity ($u_c$) and wave-orbital velocity ($u_w$). The current velocity varies with the tide and changes direction during low and high tide. The current transports the sediment as described in the paragraph above. The wave-orbital velocity is caused by the circular motion that water particles make during a wave. Figure 3.3 shows the circular motion of a water particle below a passing wave. Near the surface, the motion is almost completely circular. This shape changes as you move down in the water column towards the bed. The circular motion changes from nearly circular to an ellipse, and eventually to an almost completely horizontal motion near the bed (Bosboom & Stive, 2023). The horizontal amplitude also reduces, but since the water near the coast is not deep, water particles near the bed will still be affected by the passing waves and therefore a horizontal motion persists near the bed. When a wave passes, the horizontal flow velocities are positive below the wave crest and negative below the through.

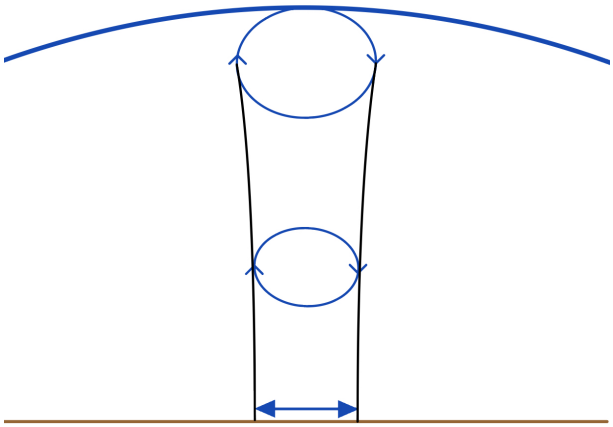

**Figure 3.3:** Movement of a water particle below a passing wave from the top of the water column to the bed (Bosboom & Stive, 2023)

For a completely symmetric wave, the velocity signal-induced sediment transport is net zero over one wave motion. The flow velocity amplitudes below a passing wave are equal for both directions, so the horizontal velocities transport sediment back and forth. However, waves that approach the coastline are not completely symmetric. As waves reach the coast they become skewed, as shown in figure 3.4. A skewed wave has a sharper crest and a flatter through. The wave asymmetry induces an asymmetric horizontal flow velocity amplitude.

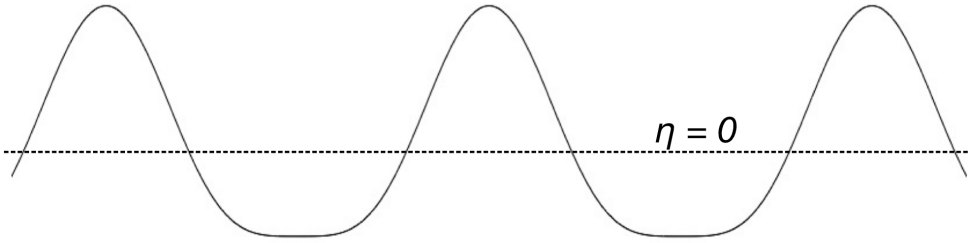


**Figure 3.4:** Skewed wave shape. With a longer trough and a sharper crest of the wave. The zero elevation is indicated with a dotted line (Bosboom & Stive, 2023).

A positively skewed wave has larger peak velocities in the propagation direction. Since the sediment transport does not react linearly to the velocity signal, see formula 3.2, this creates a net transport in the wave propagation direction ((Ribberink et al., 2008);(Bosboom & Stive, 2023)).

## 3.2 | Bed ripples

### 3.2.1 | Presence of bed ripples

So far, the bed has been assumed to be flat and smooth. However, the bed below the waterline is not always flat. On the contrary, for much of the time, different bed forms, like bed ripples or dunes, can exist. These are of different spatial and temporal scales. This research goes into the smallest bedform, bed ripples. Spatially they are of the order centimeters to meters and temporal of the order of hours (Bosboom & Stive, 2023). Orbital ripples are present due to the interaction of waves in shallow water and the bottom, which was first described by Bagnold and Taylor (1946). The wave-orbital velocity caused by a passing wave induces horizontal flow velocities over the bottom, figure 3.3. These flow velocities mobilize the sand grains on the bottom and cause them to move back and forth with the flow velocity below the waves. These rolling grains become organized and form small rolling grain ripples. These are ripples with a height of a couple of grain diameters. When

orbital velocities become higher, or a disturbance occurs on the bed, the rolling grain ripples become trapped and a larger ripple occurs. This initiates the vortex ripple, associated with the vortex-ripple effect. These ripples have a height in the order of centimeters to decimeters and a length in the order of decimeters to meters.
When conditions become too energetic (flow velocities become larger due to larger waves), these ripples are washed away. During these very energetic conditions, bed load transport is done in sheet flow. The high flow velocities keep a layer with very high concentration of sediment above the bed in suspension. Whether the local conditions stimulate sheet flow or vortex ripples can be determined with the mobility parameter ($\psi$), which expresses the mobility of the sediment for the flow conditions. This is a dimensionless parameter that increases when conditions become more energetic (Ribberink et al., 2008):

$$\psi \propto u^2 \tag{3.5}$$

There are several definitions of which velocity to use in the formulation of the mobility parameter. Ribberink et al. (2008) uses the following definition of the mobility number:

$$\psi = \frac{2u_{rms}^2}{(1-s)gD_{50}} \tag{3.6}$$

Here, $u_{rms}$ is the root-mean-square velocity of the combined current-wave-orbital velocity at the bottom $D_{50}$ is the median grain diameter, $s$ is the relative density of sand compared to water, $\frac{\rho_s}{\rho_w}$, and g is the acceleration due to gravity. Ribberink et al. (2008) made the following distinction between the sheet flow and vortex ripple states:

$$\text{vortex ripples: } \psi < 100$$
$$\text{sheet-flow: } \psi > 200$$

For mobility numbers between 100 and 200 the state is not clearly defined, and sediment transport by sheet flow and ripples is taken into account. An interpolation method between these two can be chosen.

### 3.2.2 | Sediment transport

The presence of bed ripples significantly impacts the motion of water and, therefore, sand motion over the bed (Ribberink et al., 2008). This influences both the bedload and suspended sediment transport. Figure 3.5 shows how ripples on the bed affect the flow over the bottom and the sand particle interaction with the flow.

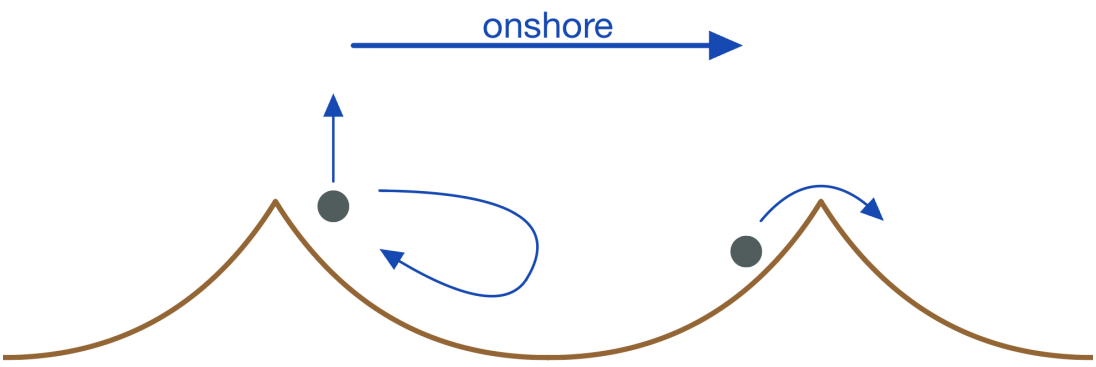


**(a)** Sand particle and flow interaction over a ripple for the larger onshore wave-orbital velocity.

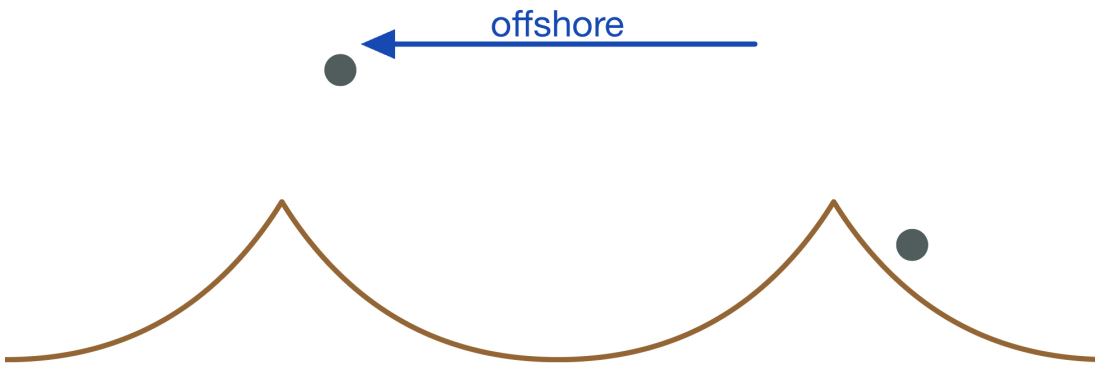


**(b)** Sand particle and flow interaction over a ripple for the smaller offshore wave-orbital velocity.

**Figure 3.5:** Wave-orbital velocity and sand sand particle interaction die to the ripple-vortex-effect ((Ribberink et al., 2008);(McCall et al., 2018)).

Previously, it was discussed that waves and their orbital velocity become skewed as they approach the coast. During a full cycle of the wave orbital motion over a ripple, two processes are present. The first process is the vortex shedding. During the higher onshore velocity, depicted in figure 3.5a, the high velocities create a turbulent flow over the ripple crest that stirs up sediment. These turbulent vertices behind the ripple crests are reflected upwards and bring additional sediment into suspension. When the flow reverses, figure 3.5b, these particles are transported offshore. Because the onshore velocities are higher, more sediment is brought into suspension during the passing of a wave crest, which is then transported offshore by the returning flow. During the reversed flow, sediment is also brought into suspension by the vortexes, and then transported onshore. However, due to the lower return velocities, this is less sediment. The result is a net offshore suspended sediment transport (Ribberink et al., 2008).
Secondly, the bedload transport is affected by rolling grains over the ripple crest. In figure 3.5a the onshore velocity, which is larger than the offshore velocity, picks up a sand grain at acceleration flow in the offshore facing side of the ripple, which is then deposited over the ripple crest. After flow reversal, the lower velocity cannot transport the sand grain back over the ripple crest. The ripples induce an onshore-directed bedload sediment transport (Ribberink et al., 2008).

### 3.2.3 | Ripple migration

Recent studies by Wengrove et al. (2017 & 2018) and Kalra et al. (2022), have focused on the migration of the ripples. The possible migration of ripples adds to the bedload transport. Ripple migration is the movement of the ripple volume due to sediment transport by hydrodynamic forcing, especially the skewness of the velocity signal below the waves. Research by Traykovski et al. (1999) showed that ripple migration was primarily onshore-directed, and since the suspended transport over ripples was found to be primarily offshore, this could not be the main driver behind ripple migration. Further investigation by Crawford and Hay (2001) and Hurther and Thorne (2011) showed that the skewness of the shoaling waves should be the main driver. This also follows from the previously explained bedload transport in figure 3.5.
The direction of ripple migration is mainly onshore, since shoaling waves develop a positive skewness, creating higher onshore velocities. However, Crawford and Hay (2001) discovered that during storm build-up, the velocity signal below waves could become negatively skewed, which triggered offshore ripple migration.

## 3.3 | Sheltered beaches

The existence, creation, and migration of bed ripples and coastal sediment transport have been extensively researched over the past decades. Bagnold and Taylor (1946) were one of the first to describe the formation and influence of orbital ripples. He performed flume experiments to observe the creation of ripples in a controlled environment. Over the past decades, a lot of research has gone into the prediction of coastal sediment transport at open ocean beaches, leaving out beaches that are sheltered from ocean waves in estuaries and bays, while the total length of sheltered beaches is much more than open ocean beaches ((Vila-Concejo et al., 2010); (Travers, 2007); (Vila-Concejo et al., 2020)). The term sheltered beaches is widely discussed in the mentioned research. To be classified as a sheltered beach, several categories can be met. The two most important for this research are a fetch limit and protection from ocean waves:

- Fetch, is the distance over which wind can act to form waves arriving at the beach ((Holthuijsen, 2007);(Bosboom & Stive, 2023)). A beach classifies as fetch-limited when this distance is too short for wind-generated waves to develop to their potential fully. This causes waves with less energy than without a fetch restraint (Jackson et al., 2002). It is suggested that a threshold for a fetch-limited beach is a fetch of $< 50$ km ((Cooper et al., 2007);(Nordstrom & Jackson, 2012); (Young & Verhagen, 1996)).
- Protection against ocean waves is the case with for example back barrier beaches. Ocean waves can penetrate the bay or estuary where that beach is located, but will not arrive directly at the shoreface (Vila-Concejo et al., 2020). The protection against ocean waves also causes a low-energetic wave climate.

Because of the limited fetch and the protection from ocean waves, waves are less energetic in both storms and calmer conditions. Jackson et al. (2002) made the first classification of the low-energy state of these beaches in four categories:

- During calm conditions, meaning little onshore wind, the significant wave height at the beach is minimal, $< 0.25$ m.
- During strong onshore winds, the significant wave height is limited due to the limited fetch, $< 0.50$ m.
- The beach width is small and has a width smaller than about 20 meters.
- Morphological features of the beach are inherited from storm conditions and the calmer conditions in between are incapable of reworking the beach.

Studies by Jackson et al. (2002), Travers (2007), and Vila-Concejo et al. (2020) have shown that the cross-shore profile of a sheltered beach differs from an open ocean coast. The coastline profile is highly dependent on the hydraulic conditions and sediment type, but overall the following distinction can be made between sheltered beaches and open ocean beaches:

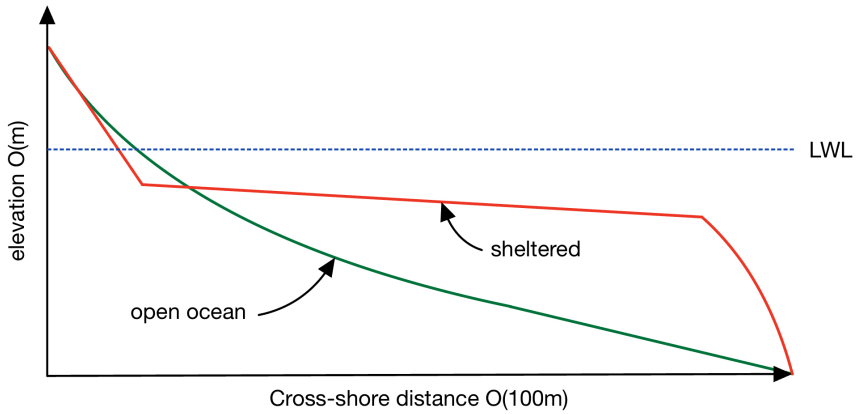


**Figure 3.6:** General difference between an open ocean coast and a sheltered beach.

Figure 3.6 shows that sheltered beaches have a sub-tidal platform combined with a relatively steep

slope at the waterline. The sub-tidal platform ranges in the order of 10 to 100 meters and can differ in slope, but is a consistent feature of a sheltered beach.

## 3.4 | Modeling

The understanding of sediment transport related to hydrodynamic conditions is used in the modeling of coastal development. One of the models used is the model XBeach (Roelvink et al., 2010). The wave- and tidal climate and measured bathymetry are used to determine sediment transport rates over a desired period. Erosion and accretion over the model domain are calculated and the development of the coastline can be predicted. A recent study by McCall et al. (2018) focused on a sheltered beach at the Houtribdijk in the Netherlands. In their research, they used the model XBeach to calculate the development of this beach between two profile measurements of the beach. Figure 3.7 shows the results:

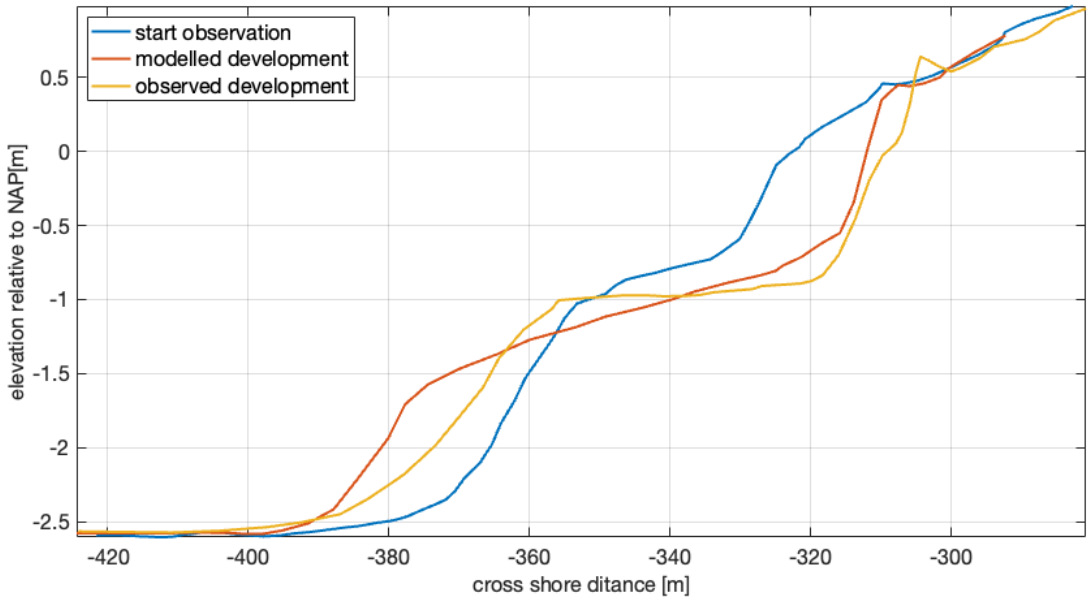


**Figure 3.7:** Measured and modeled cross-section development at the Houtribdijk (McCall et al., 2018)

In the figure, the characteristic horizontal plateau is visible in the profile after observation. However, the profile that was calculated using XBeach, does not have this feature. More sand is deposited lower in the profile and does not reach the upper part to form a sub-tidal plateau. It was also discovered, as previously assumed for sheltered beaches, that the beach was in the vortex-ripple regime for almost all of the time. The handling by the model of ripples and the effect on bedload and suspended transport could be one of the reasons why XBeach was not capable of reproducing the beach development. As standard, the model XBeach does not incorporate ripples. XBeach uses the principle of equation 3.1 to determine sediment transport. The sediment concentration, $C$, is calculated using the following formula:

$$C_{eq} = \max(\min(C_b, \frac{1}{2}C_{max}), \min(C_s, \frac{1}{2}C_{max}), 0) \tag{3.7}$$

Here, $C_s$ and $C_b$ are the equilibrium sediment concentrations for suspended and bedload transport. These are calculated using one of three formulations: Soulsby-Van Rijn (Soulsby, 1997)(L. C. v. Rijn, 1984), Van Thiel-Van Rijn (Van Rijn, 2007)(Van Thiel de Vries, 2009), or Van Rijn (L. C. V. Rijn et al., 1993). The last parameter, $C_{max}$, is the maximum allowed sediment concentration. The concentration is used with local flow velocities to calculate the sediment transport. McCall et al.

(2018) used an altered formulation of the sediment transport, where below a mobility number of 190, calculating using formula 3.6, the orbital wave motion would influence the transport velocity of sediment negatively. The bedload transport was not altered. The direction of the resulting net transport was calculated using the suspension parameter by Ribberink et al. (2008):

$$P_r = \frac{2\pi\eta}{w_s T} \tag{3.8}$$

Here, $\eta$ is the ripple height, $w_s$ is the fall velocity of a sand particle in water, and $T$ is the wave period. When this parameter was below 0.8 the onshore bedload transport was dominant and above 0.8 the offshore suspended transport was dominant. As said, these alterations did not suffice and XBeach was not able to predict the correct coastline development. To further investigate why the presence of ripples could be responsible for this, the method of incorporating ripples into models must be looked at. Ripples are a result of hydrodynamic forcing interacting with the sand particles on the bed. To predict the presence and dimensions of ripples on the bed. Ripple predictors have been developed for models.

## 3.5 | Ripple predictors

Ripple predictors are used to calculate dimensions for ripples under wave current forcing. In their computation, these predictors are used in models like Delft3D and XBeach to predict bed roughness (McCall et al., 2018)(Brakenhoff et al., 2020). This paragraph gives a closer look at three of these ripple predictors. The main focus is on the input parameters needed for the prediction of the ripples. These can vary from for example a depth-averaged to a maximum velocity near the bed. The ripple predictors used in this report are the predictors developed by, O'Donoghue et al. (2006) (OD), Van Rijn (2007) (VR), and Khelifa and Ouellet (2000) (KO). These predictors are chosen, because OD is used in the model XBeach in the research by McCall et al. (2018), VR is mainly used in Delft3D and KO is a predictor that uses similar input variables as these two predictors and is tested for a wave current regime. The predictors are discussed first and then their main differences are explained in an overview afterwards. How the necessary flow parameters are obtained will be discussed in the next chapter.

### O'Donoghue et al. (2006)

The first predictor that is discussed is the one by O'Donoghue et al. (2006). The general formulas to predicted ripple height, $\eta$, and wavelength, $\lambda$, are respectively:

$$\frac{\eta}{a} = 0.275 - 0.022\psi^{0.42} \tag{3.9}$$

$$\frac{\lambda}{a} = 1.97 - 0.44\psi^{0.21} \tag{3.10}$$

The equations use two variables, the mobility number, $\psi$, and the horizontal particle amplitude, $a$. The mobility parameter, as will be seen, is used in all of the three ripple predictors. The general formulation of it is the same. However, the specific velocity that is used, differs between the formulas. In this predictor, the mobility parameter is defined as:

$$\psi_{w;max} = \frac{u^2_{max;bed}}{(s-1)gD_{50}} \tag{3.11}$$

The velocity, $u$, is the maximum particle orbital velocity near the bed, as explained in section 4.3.2, $s$ is the sediment specific density, which is 2.65 for sand, $g$ is the acceleration due to gravity, and $D_{50}$ is the grain size that is smaller than 50% of the sediment.
The horizontal amplitude of the water particle displacement, $a$, is calculated by:

$$a = \frac{u_{max;bed}}{\omega} \qquad \text{with} \qquad \omega = \frac{2\pi}{T} \tag{3.12}$$

### Van Rijn (2007)

The second ripple predictor that is treated is created by Van Rijn (2007). The predictor calculates a ripple roughness, $k_r$, that is assumed to be equal to the ripple height. The predictor has a formula for the expected ripple height only. It is defined for three ranges of the mobility parameter:

$$\begin{aligned} k_r &= 150 f_{cs} D_{50} && \text{for} && \psi \leq 50 \\ k_r &= 20 f_{cs} D_{50} && \text{for} && \psi > 250 \\ k_r &= (182.5 - 0.652\psi) f_{cs} D_{50} && \text{for} && 50 < \psi \leq 250 \end{aligned} \tag{3.13}$$

The mobility parameter from equation 3.11 is used, but with a different definition of the velocity parameter. The velocity parameter as described by Van Rijn (2007) is:

$$U_{wc}^2 = U_w^2 + u_c^2 \tag{3.14}$$

Here, $u_c$, is the depth-averaged current velocity, and $U_w$ is the peak orbital velocity near the bed. This is calculated using the following set of equations:

$$U_w = \frac{\pi H_s}{T_r \sinh(2kd)} \tag{3.15}$$

with

$$T_r = \text{ relative wave period } = \frac{T_p}{1 - (u_c T_p / L)\cos(\phi)}$$

$$L = \text{ wave length from: } (L/T_p \pm u_c)^2 = \frac{gL \tanh(2\pi h/L)}{2\pi}$$

Here, $H_s$ is the significant wave height, $\phi$ is the angle between the current and wave propagation direction, and $T_p$ is the peak wave period. Factor $f_{cs}$ in formula 3.13 is a correction factor for a gradually decreasing bed roughness for coarser grain sizes:

$$\begin{aligned} f_{cs} &= 1 && \text{for} && D50 \leq 500 \ \mu m \\ f_{cs} &= (0.0005/D50)^{1.5} && \text{for} && D50 > 500 \ \mu m \end{aligned}$$

The ripple wavelength is determined based on an assumed constant ripple steepness, $\eta/\lambda = 0.16$ (Traykovski, 2007):

$$\lambda = \frac{\eta}{0.16} \tag{3.16}$$

### Khelifa and Ouellet (2000)

The last ripple predictor is developed by Khelifa and Ouellet (2000). This ripple predictor also uses the mobility number that consists of a wave and current velocity, $\psi$, and includes a term for the angle between the current and wave propagation, as does Van Rijn (2007). The two formulas for the ripple height and length are:

$$\frac{2\eta}{d_{wc}} = 0.32 + 0.017 \ln^2(1 + \psi_{wc}) - 0.142 \ln(1 + \psi_{wc}) \tag{3.17}$$

$$\frac{2\lambda}{d_{wc}} = 1.9 + 0.08 \ln^2(1 + \psi_{wc}) - 0.74 \ln(1 + \psi_{wc} \tag{3.18}$$

$$\tag{3.19}$$

Although the velocity variable for the mobility number consists of a current and wave contribution, it is differently formulated than equation 3.14. Here it is:

$$U_{wc} = \left(\frac{U_\delta}{\pi}\right) + \bar{\bar{u}}^2 + 2\frac{U_\delta}{\pi}\bar{\bar{u}}|\cos\theta| \tag{3.20}$$

The two unknown terms in this equation, $U_\delta$ and $\bar{\bar{u}}$, are the velocity amplitude at the edge of the boundary layer, and the depth-averaged current velocity respectively.
The last variable for this predictor is the effective fluid orbital diameter, $d_{wc}$. This is described as:

$$d_{wc} = T\sqrt{U_{wc}} \tag{3.21}$$

### Sediment grain size

All of the ripple predictors use the median sediment grain size (D50) in the calculation of the mobility parameter, see formula 3.11, while Van Rijn (2007) also uses it in the correction factor $f_{cs}$. The median sediment grain size (D50) is part of a sediment classification. On a beach, the sand grains will not have one size. Instead, the grain sizes are distributed over a range of smaller to larger grains. The sediment on a beach is therefore classified using a sediment grain distribution. Figure 3.8 shows an example of a grain size distribution in recent research by Van der Lugt et al. (2024).

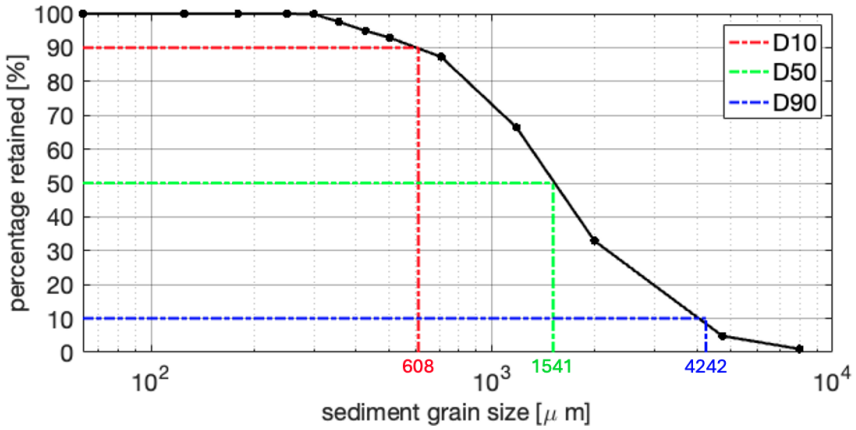


**Figure 3.8:** Example of a sediment grain size distribution from Van der Lugt et al. (2024)

The D50 that is used by the ripple predictors is highlighted in green. Of a sand mixture, 50 percent of the mass of the mixture is higher than this diameter and 50 percent is lower than this value. What the actual D50 is during this research is explained in the next chapter.

### Overview

The main differences between these predictors lie in the definition of the velocities used in the mobility parameter. These are explained in table 3.1.

| Predictor | Variable | Definition |
|---|---|---|
| KO | $U_\delta$ | Amplitude at the boundary layer |
| | $\bar{u}$ | Depth-averaged flow velocity |
| VR | $U_w$ | Maximum amplitude of the velocity near the bed. Calculated using the significant wave height and relative period. |
| | $u_c$ | Depth-averaged flow velocity |
| OD | $u_{max;bed}$ | Amplitude of the maximum velocity near the bed |

**Table 3.1:** Definition of flow variables for every ripple predictor.

## 3.6 | Importance of research

Understanding sediment transport in coastal areas is crucial to model coastline development, which is very important to design new measures to protect coastlines against the effects of climate change:

more severe storms and sea-level rise will increase the load on the coastline. Over the past decades, most of the research has been performed on open ocean coasts, while sheltered beaches make up a larger part of the coastlines in the world. Therefore, models have been developed calibrated on open ocean coasts. Recent research has shown that XBeach was not able to recreate measured cross-shore development for the Houtribdijk beach. The low-energetic wave climate of this sheltered beach meant that the beach was in the vortex-ripple sediment transport mode for almost the entire time of the measurements. In general, it is expected that sheltered beaches will be in the vortex-ripple regime more often than open ocean beaches, because of the low-energetic state of the waves (even during storms). A misunderstanding in the behavior of ripples on sheltered beaches could therefore be one of the reasons why the XBeach model was unable to create the correct cross-shore profile. The fact that a sheltered beach could feature a different sediment transport mechanic than open sea beaches that is not incorporated in current modelling, shows the need for additional research into sediment transport at sheltered beaches.

# 4 | Methodology

The behavior of ripples at a sheltered beach is researched using field data from the Prins Hendrikzanddijk (PHZD). The SEDMEX campaign in 2021 by Van der Lugt et al. (2024) collected data at this beach. This research uses this data together with field data from a new campaign in 2023, SEDRIP, performed to enlarge the SEDMEX data set, while slightly adjusting some of the equipment to perform better. This chapter first explains the sheltered beach at the PHZD. Secondly, the used equipment is explained. The settings for the SEDMEX campaign are then discussed together with alterations for the SEDRIP campaign. This concludes the method for the gathering of the field data. A new paragraph discusses how the data is processed into usable statistics, which is followed by a paragraph that discusses additional formulas necessary to answer the three sub-research questions.

## 4.1 | Prins Hendrikzanddijk

The PHZD and its adjacent beach are located on the southeast side of the island of Texel in the Netherlands facing the Wadden Sea. The beach is sheltered because it is protected from open sea waves by the island and the land surrounding the Wadden Sea provides a fetch limit for wave build-up. The PHZD is a sandy beach constructed in 2019 as a new coastal defense structure to protect the island against higher water levels and more frequent storms due to climate change (Perk et al., 2019).


**Figure 4.1:** Location of the fieldwork site on Texel highlighted in red. The zoomed-in figure shows the beach itself. The red dot shows the location of the devices (Google Earth, 2023).

During the SEDMEX and the SEDRIP campaign, devices were installed near the red dot in figure 4.1. The cross-section of the beach at this location is shown in figure 4.2. The red vertical line shows the position of the devices in the cross-section. The typical shape of a sheltered beach, a steeper slope near the water line, and a flat sub-tidal plateau are also visible: the steeper slope is visible between the high and low water levels, while the frame's location marks the beginning of the sub-tidal plateau.

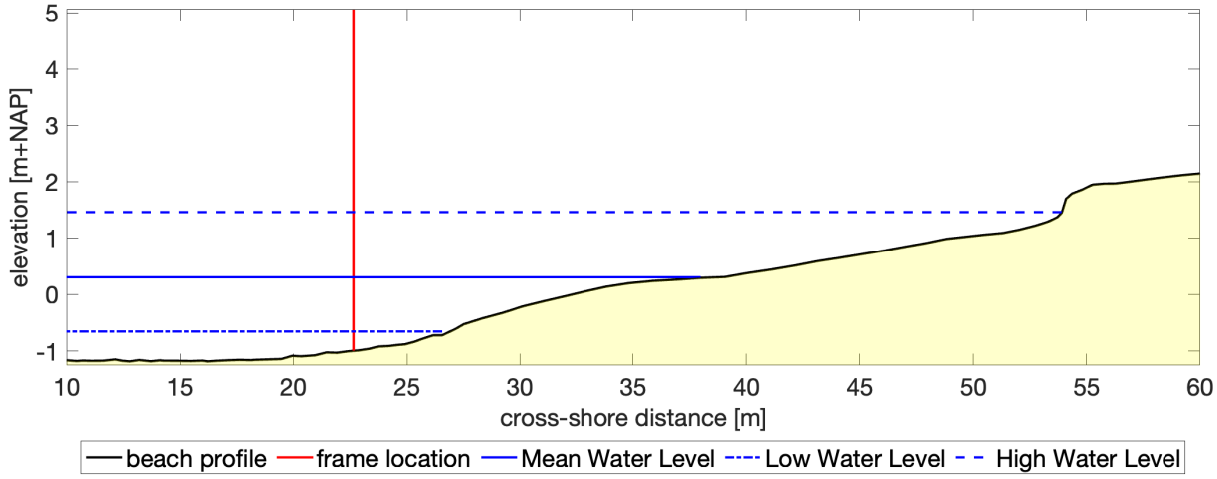


**Figure 4.2:** Location of the frame on the beach cross-section.

The sediment conditions on the beach are inconsistent. During the SEDRIP campaign, the sediment was inspected visually and consisted of a mixture of sand and pieces of broken shells. In the SEDMEX campaign, several sediment samples were collected at the frame's location. These were analyzed and the grain size distribution of each sample was determined. The measured D50 values, calculated by Van der Lugt et al. (2024) are displayed below:

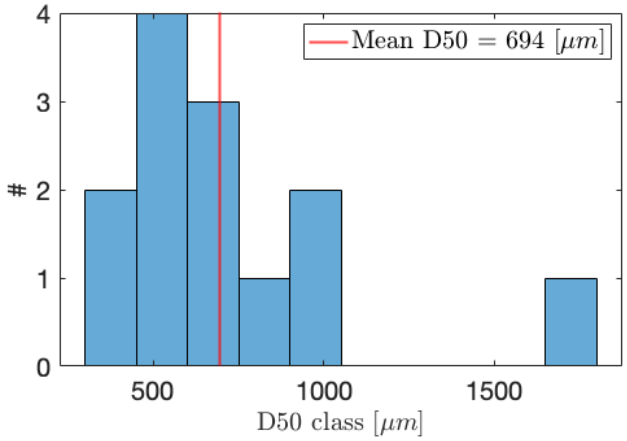


**Figure 4.3:** Histogram of the spread in D50 values for the sediment size.

Over the SEDMEX campaign different sediment sizes were measured at the beach. During the SEDRIP campaign, no sediment sizes were determined. Because of the variability in the data, the D50, necessary for the computation of the mobility number, is assumed to be the mean of the measured D50 values of all collected sediment samples from the SEDMEX campaign, 694 $\mu m$.

## 4.2 | Device setup

During the SEDMEX and SEDRIP campaigns an Acoustic Doppler Velocimeter (ADV) and a Sand Ripple Profiling Logging Sonar (SRPLS) were installed on a metal frame located at the red line in the cross-section in figure 4.2, which is located at the red dot in figure 4.1. This paragraph describes the metal frame, how the devices work, and what choices can be made in their setup. The chosen setup for the SEDMEX and SEDRIP campaigns is discussed after this.

### 4.2.1 | Frame

In both campaigns, a metal frame was installed using jet poles that were inserted in the bed and metal bears in between these, on which the devices were mounted. Figure 4.4 shows the general setup of the frame for the SEDRIP campaign. Two poles are installed parallel to the shoreline and one towards the coast so that a triangle pointing towards the beach is created. The two parallel poles are installed this way because they will be on the same depth contour. The Acoustic Doppler Velocimeter (ADV) and SRPLS are installed on these poles so that all of the measurements take place at the same depth. The third pole is added for stability.

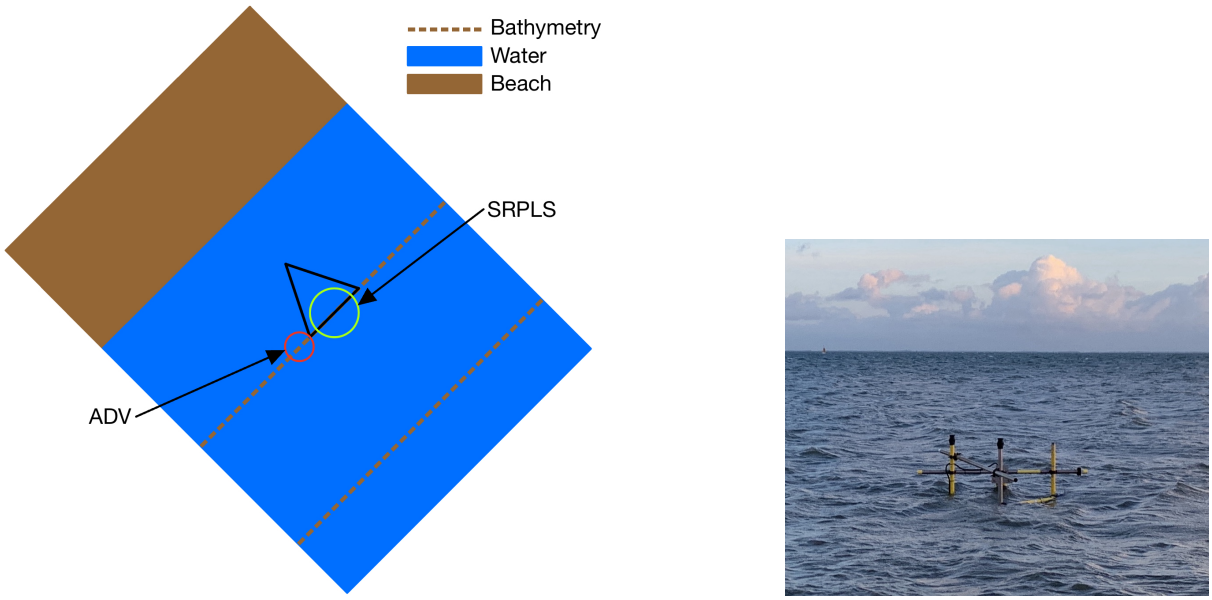


**(a)** Schematized image of frame setup

**(b)** Photo of the frame installed in the water.

**Figure 4.4:** Overview of the device setup on the frame.

The frame's dimensions are based on the operational requirements of the equipment installed on it. Only the width of the parallel seaward poles is important. To identify the orientation of the SRPLS bed image, the two poles of the frame have to be visible in the image. The width of these poles must therefore be slightly smaller than the diameter of the expected footprint.

### 4.2.2 | SRPLS

The SRPLS measures bottom profiles using acoustic sonar. A signal is emitted and the device measures the intensity of the backscatter after the signal (Marine Electronics, 2009). This provides the first limitation of the device: it must be submerged to conduct the measurements. A second limitation is the battery use. The device uses two small electric motors to rotate a sonar head over two degrees of freedom. Continuous measurements would drain the 1080 Wh battery in a little more than 2.5 days. Switching batteries every 2.5 days would be inconvenient and the battery usage could become very expensive over longer campaigns. The biggest challenge is the choice of device setup, for which a balance between time and accuracy has to be found. This is explained using figure 4.5, which schematizes the SRPLS.

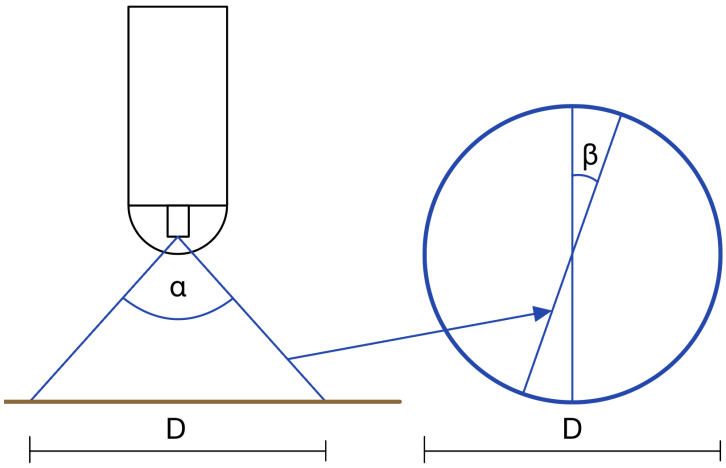


**Figure 4.5:** Overview of the SRPLS.

The SRPLS has two degrees of freedom, $\alpha$ and $\beta$, also called swath rotation and horizontal rotation respectively. To create an image of the bed, the device completes a full swath of $\alpha$-degrees and then rotates with $\beta$-degrees in the horizontal plane and repeats the swath rotation. This continues until the total horizontal rotation accumulates to 180 degrees and a footprint with diameter D is completed. The step sizes for $\alpha$ and $\beta$ can be set by multiples of 0.9 degrees. The total size of $\alpha$ can range from 30 to 180 degrees with steps of 30 degrees. With the total swath rotation, the diameter of the footprint can be set. The step sizes of $\alpha$ and $\beta$ influence the accuracy of the measurements and the total duration of the measurements. For a larger size of the swath rotation and a more accurate step size setting, the measurements will take longer. The objective of a bed geometry measurement is to obtain a snapshot in time. Therefore, the aim is to reduce the measurement time as much as possible without lowering the resolution too much. However, there is no documentation on durations concerning the device settings. Apart from the total swath arc and rotation settings, the time interval between each measurement has to be specified. This can be managed by two parameters: the interval between each wake-up, $\Delta t$, and the number of measurements at every wake-up, $n$. For example, a wake-up interval of 30 minutes together with two measurements at each wake-up, means that every 30 minutes two consecutive measurements are performed.

### SEDMEX

During the SEDMEX campaign, the following settings of the SRPLS were used:

| Parameter | Value | Description |
|---|---|---|
| $\alpha$ | $120°$ | The total swath arc is set to 120 degrees. Using this setting, the footprint has a diameter of almost 3.5 times the installation height. |
| $\Delta\alpha$ | $0.9°$ | The device was set up to be the most accurate as possible for the swath arc rotation. This will take the most time. |
| $\Delta\beta$ | $0.9°$ | The step size in the horizontal rotation is set to 0.9 degrees. This is also the most accurate setting and will result in a long measurement time |
| $\Delta t$ | 1 hr | The device starts a measurement cycle every hour. |
| $n$ | 2 | During every measurement cycle, two full measurements are made. This results in two consecutive bed images. |

**Table 4.1:** Settings of the SRPLS for the SEDMEX campaign.

The settings for the accuracy and swath arc size result in a single measurement cycle that takes about 13.5 minutes. Of these cycles, two were performed consecutively every hour. The SRPLS was

mounted at a height of about 75 centimeters, which resulted in a footprint diameter of about 2.6 meters.

### SEDRIP

Based on the SEDMEX campaign, the settings are changed. Firstly, the measurement time is reduced by lowering the total swath arc to 90 degrees. This will result in a footprint diameter of 2 times the installed height. Using a similar height of 75 centimeters, this will be 1.5 meters. This is still assumed to be sufficient because the wavelength of the bed ripples is expected to be in the order of 10 centimeters. A footprint of 1.5 meters will be able to capture the complete wavelength of a ripple. Secondly, the rotation step size, $\Delta\beta$, is increased to 1.8 degrees. This will also reduce the time necessary for a full measurement, while it was tested to be accurate enough for the measurement of bed ripples. The interval of the measurements is also changed. The wake-up interval is set to 15 minutes and only one measurement is performed on every wake-up. Table 4.2 summarizes the settings for the SEDRIP campaign:

| Parameter | Value | Description |
|---|---|---|
| $\alpha$ | $90°$ | The total swath arc is set to 90 degrees. This will lead to a footprint diameter of twice the installed height. |
| $\Delta\alpha$ | $0.9°$ | The swath arc step size is kept at the most accurate setting to keep a high resolution in a swath. |
| $\Delta\beta$ | $1.8°$ | The step size in the horizontal rotation is set to 1.9 degrees, because this leads to a relatively small reduction in resolution but half of the measurements, so a considerable reduction in time. |
| $\Delta t$ | 1 hour | The device starts a measurement cycle every 15 minutes. |
| $n$ | 1 | At every wake-up only one measurement is performed. |

**Table 4.2:** Settings of the SRPLS for the SEDRIP campaign

The time for one measurement was tested and amounted to 5.5 minutes. Bed geometry changes with a smaller timescale than that will not be captured. It is assumed that this is sufficient by looking at previous research by Wengrove et al. (2017 & 2018) since the time interval of interest has to be smaller than the migration rate of the ripples and this was measurable with measurement intervals of 12-20 minutes in their research.
The measurements create a dataset that consists of the backscatter intensity of the acoustic emission by the SRPLS over the water column for every vertical swath measurement. The method used to determine a bed profile out of every set of vertical swath measurements is explained after the settings of the ADV are discussed.

### 4.2.3 | ADV

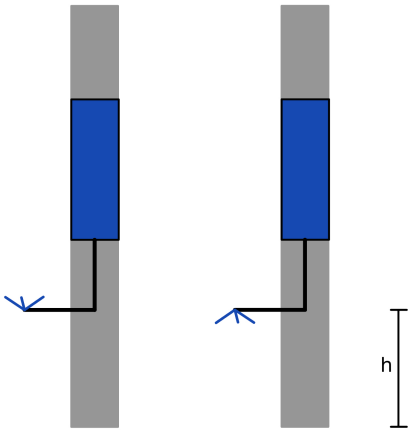


**Figure 4.6:** Installation of the ADV. On the left a head facing up and on the right a head facing down.

The ADV is installed on the same frame at the location of the red circle in figure 4.4. An ADV measures water particle movement in its control volume and water pressure using a pressure sensor. It measures the water particle movement using the Doppler effect of an acoustic signal from three probes (Nortek Group, 2023). The orientation of these probes at installation is measured. Using the orientation the water particle movement relative to the North can be calculated. The ADV can be installed in two ways: facing up or down. This is shown in figure 4.6. The ADV is installed with a down-facing head. The control volume where the device measures the particle velocities is located 15 centimeters away from the probes.
In both of the campaigns, the ADVs were set up to measure particle excursion in the control volume constantly. This offers the opportunity to construct a dataset with hydrodynamic statistics for desired periods later during the data processing. The installation height of the ADVs was different for both of the campaigns. In the SEDMEX campaign, the control volume was located 15 cm above the bed, while during the SEDRIP campaign, this height was 30 cm. This additional space between the bed in the control volume is left to accommodate accretion over the campaign.

## 4.3 | Data Processing

The raw data collected during the SEDMEX and SEDRIP campaigns consists of sonar backscatter of the SRPLS and particle excursion and pressure from the ADV. From the sonar backscatter bed images have to be constructed, while the ADV measurements are processed into wave statistics, wave orbital, and current velocities.

### 4.3.1 | SRPLS

The raw data from the SRPLS consists of 100 or 200, for the SEDRIP and SEDMEX campaign respectively, vertical plane measurements. Each swath measurement consists of columns with each 800 backscatter values. These columns represent the measurements after each step $\Delta\alpha$ as shown in figure 4.5, and the backscatter value is the incident energy per unit area, maximum range divided by 800 cells, in that column that is directed back to the SRPLS. Over the water column, the sea bed will have the highest backscatter since this is the part that will reflect most of the signal toward the transponder. This section will explain the algorithm that finds the maximum in every column and translates that into a 3D picture of the bed. The algorithm is a method produced by Ruessink et al. (2015). In short, the algorithm determines the bed geometry in the footprint using the following steps:

1. Determine the maximum backscatter points in every swath of a measurement.
2. Save the points as x- and z-coordinates in each swath. This results in a dataset with polar coordinates: x, $\alpha$, and z.
3. The polar coordinates are translated to Cartesian coordinates. This results in a matrix with dimensions x and y, with elevation values, z.
4. These values are interpolated over a regular grid using a loess-interpolation by Plant et al. (2002).
5. The interpolated regular grid now represents the bed, but still has a slope. This slope is removed using a leased squares plane fit. This results in a matrix with dimensions x and y with elevations of the bed geometry.

### Finding maximum backscatter

A single swath measurement is presented in figure 4.7. The backscatter values are represented with a color scheme, where bright yellow shows the maximum backscatter. The bed position can be determined by locating the highest backscatter point in each vertical. The location of the first highest backscatter point is saved as a bed point in an x and z-plane.

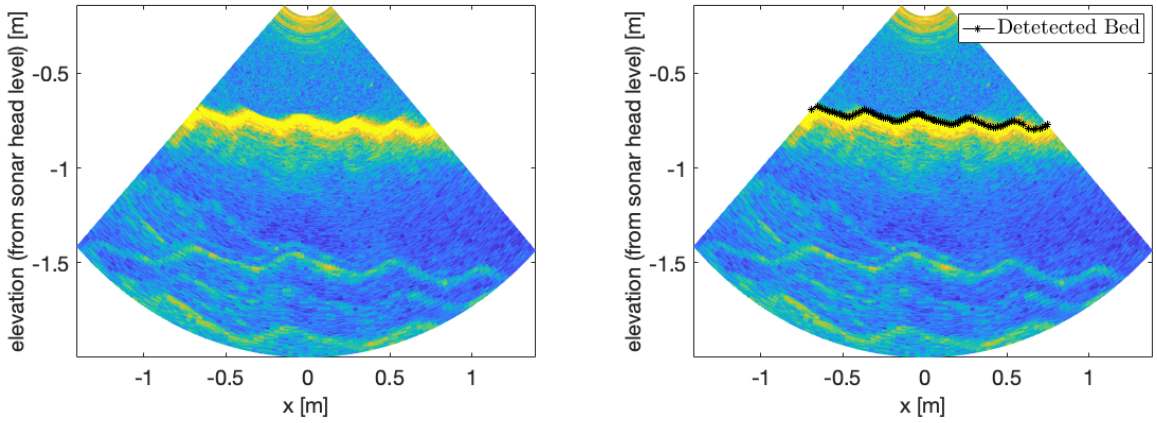


**(a)** Swath measurement showing backscatter values.

**(b)** Bed detected on maximum backscatter values in the swath.

**Figure 4.7:** Single measurement swath without and with the detected bed.

Figure 4.7 shows a measurement with no disturbance above the bed. This is visible by the bright blue color between the detected bed and the sonar head. However, very energetic conditions can cause disturbances between the bed and the sonar head, on which the transmitted sonar signal can reflect as well. This will cause higher backscatter values above the bed, sometimes even as high as backscatter levels from the bed. Using the highest backscatter level in every column will result in disturbances in the water column above the bed to be recognized as the actual bed, shown in figure 4.8a. This has to be corrected because otherwise false bed geometry will be used in the analysis.

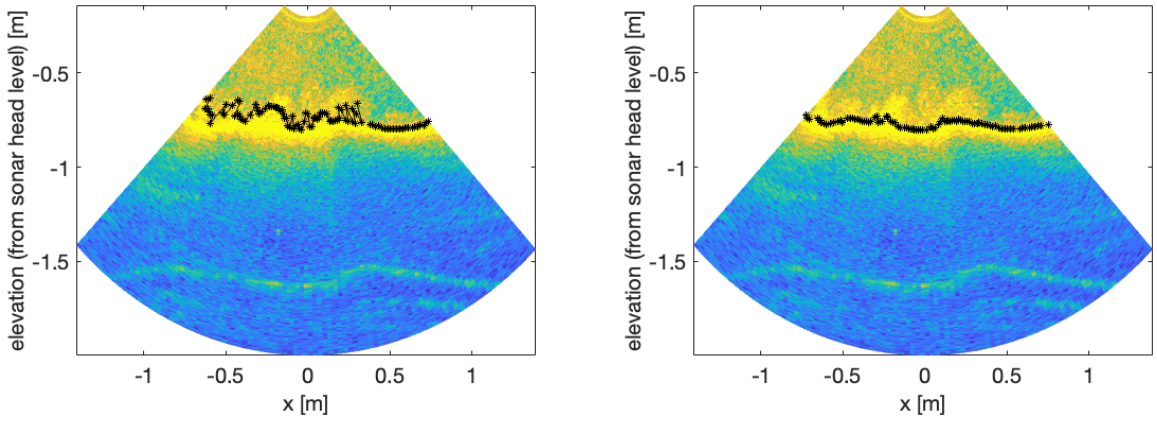


**(a)** Backscatter above the bed interpreted as the actual bed.

**(b)** The new algorithm recognizes the wrong bed points.

**Figure 4.8:** A swath measurement with a lot of backscatter above the bed.

Figure 4.8b is the bed detection after the improvements to the algorithm. Instead of taking the maximum and accepting this as the bed at that point, a check is performed. This check is schematized in figure 4.9.

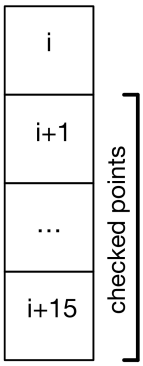


**Figure 4.9:** Addition to the algorithm.

Instead of only checking the first maximum backscatter point in each column of the swath. The algorithm now checks the following 15 points. If the found maximum backscatter at point $i$ is the actual bed, the following points must also contain an almost maximum backscatter. This feature is visible in figure 4.7: the bed consists of more than one layer of maximum backscatter points, while the wrongly detected bed points in figure 4.8a are followed by cells with less backscatter. When the algorithm finds the first cell with maximum backscatter and has checked the following 15 cells, it accepts the point as the actual bed if the average over those following points was very close to the maximum backscatter. When the average of those points is not high enough, it proceeds to find a new maximum lower in the column and repeats this process until it has found a point that satisfies the criteria.

### Creating leveled regular grid

For every measurement, the bed levels per swath are stored in a matrix. This contains an elevation for every x-coordinate in the swath that has an angle $\beta$ in the footprint, see figure 4.5. These coordinates are translated to Cartesian coordinates and are interpolated over a regular grid using a loess interpolation by Plant et al. (2002). This results in a regular grid with dimensions of $1D$ by $1D$ and a grid size of 1 by 1 cm. Figure 4.10 shows a resulting bed image from this method. The grid is

a square regular grid, while the footprint is circular. Therefore, the regular grid consists of elevation values, where the footprint is located, and NaN values where there are no measurements for the bed. Outliers after the interpolation are also passed as NaN.

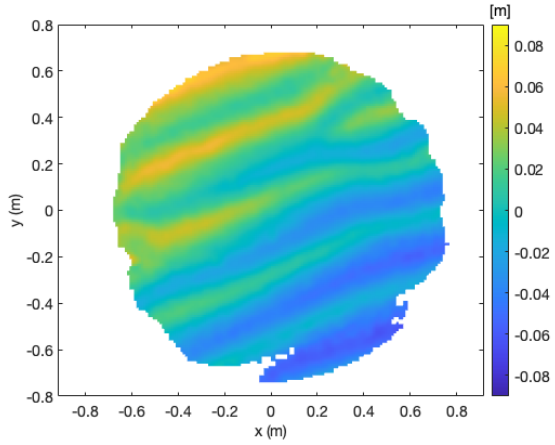


**Figure 4.10:** Bed geometry after the interpolation over the rectangular grid.

This is an image of the bed, corrected for outliers via the interpolation method, as it is seen by the SRPLS. The slope of the bed is still visible in this image. The data analysis requires this slope to be removed, so the only elevation change of the bed is the ripple geometry. This is achieved by fitting a plane to the data and subtracting it from the data. A 3D image and corresponding plane for the bed in figure 4.10 is given in figure 4.11

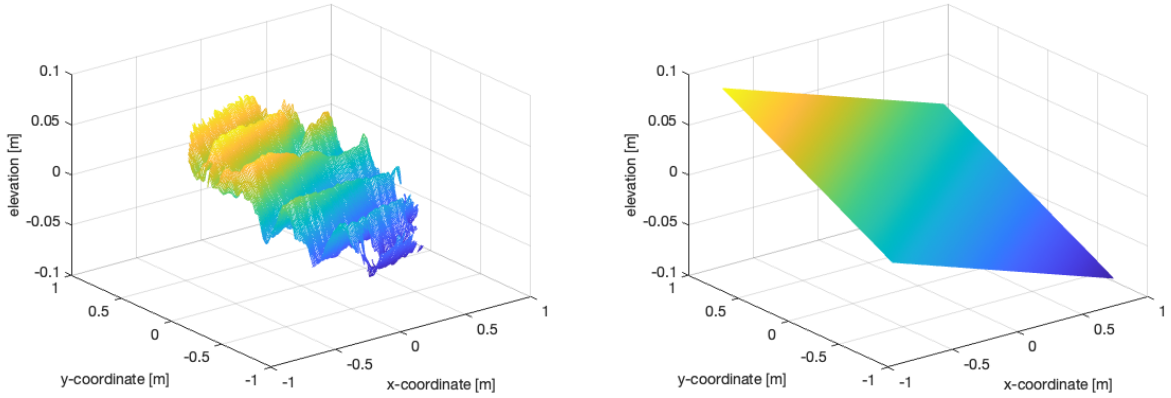


**(a)** 3D image of the measured bed.

**(b)** Fitted plane through the 3D data.

**Figure 4.11:** Leased squares plane fit for a bed image.

Subtracting the fitted plane from the 3D bed image, results in a leveled bed, which is shown in figure 4.12.

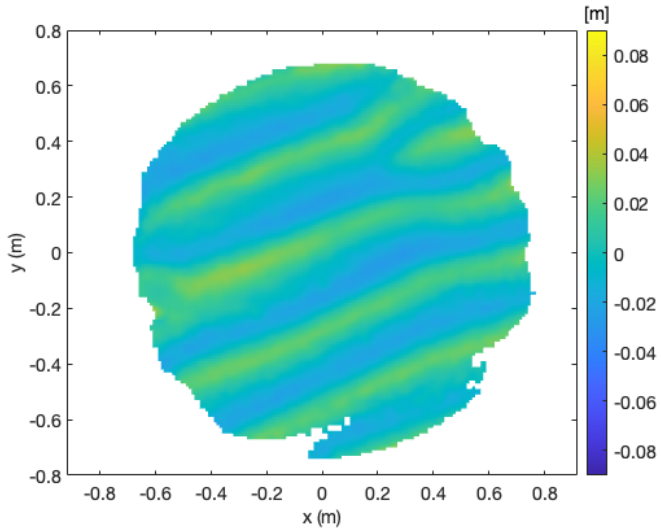


**Figure 4.12:** Leveled bed based on the bed in figure 4.10.

This sequence is performed for every 15-minute measurement and this results in a data set of regular grids with bed elevations that are corrected for the bed slope. These can be used for the data analysis later in the research.

### 4.3.2 | ADV

The ADV has measured particle velocities and water pressure continuously during the campaign. This paragraph explains how these continuous measurements are used to calculate hydrodynamics that are necessary for the ripple predictors that are discussed in paragraph 3.5. The calculation is done using the method by Van der Lugt et al. (2024) and the following types of flow and wave parameters are calculated:

1. Determine long- and cross-shore flow velocities using the known orientation of the ADV.
2. Flow velocity variables for the current and wave-orbital motion.
3. Calculate surface elevation for every block using the pressure data.
4. Wave statistics that describe wave height and period are determined using the wave spectrum.

#### Raw to usable data

The variables that are explained in the following paragraph are all calculated for 15-minute blocks coinciding with the SRPLS measurements. An overbar for the variables represents the 15-minute block average. The first step is to use the known orientation of the ADV to calculate the cross-shore velocity ($u$) and long-shore velocity ($v$) components of the velocity signal from the ADV measurements. These are used to calculate the current and wave orbital velocities.

#### Current velocity

The $u_c$ is the average velocity measured during 15 minutes in the block:

$$u_c = \sqrt{\bar{u}^2 + \bar{v}^2} \tag{4.1}$$

The current direction ($\phi_c$) is determined by the angle between the two velocity components:

$$\phi_c = \arctan\left(\frac{\bar{v}}{\bar{u}}\right) \tag{4.2}$$

### Orbital velocity

The $u_w$ can be determined by computing the deviation from the current velocity:

$$u_w = \sqrt{u^2 + v^2} - u_c \tag{4.3}$$

For the blocks different values are determined: average absolute orbital velocity ($\bar{u}_w$), root-mean square orbital velocity ($u_{w;rms}$), and 90$^{\text{th}}$-percentile orbital velocity ($u_{w;max}$). The following formulas define these:

$$\bar{u}_w = \overline{|u_w|} \tag{4.4}$$

$$u_{w;rms} = \sqrt{2}\sqrt{\overline{|u_w^2|}} \tag{4.5}$$

$$u_{w;max} = 98^{th}\text{-percentile}(|u_w|) \tag{4.6}$$

These are values for the orbital velocity in the control volume of the ADV. For the analysis, the flow velocity at different locations in the water column is needed. The flow velocity at a location z, zero at the waterline and negative downward, is calculated using formula 4.7 (Holthuijsen, 2007).

$$A = a\frac{\cosh(k(d+z)}{\sinh(kd)} \tag{4.7}$$

The variables are, the amplitude of the velocity at the waterline ($a$), wave number ($k$), and water depth ($d$). This value can be determined using the velocity amplitude at the ADV control volume. To calculate the flow velocity amplitude at the bed, equation 4.7 becomes:

$$A_{bed} = a\frac{\cosh(k(d+(-d))}{\sinh(kd)} = a\frac{\cosh(0)}{\sinh(kd)} = a\frac{1}{\sinh(kd)}$$

### Wave statistics

Apart from flow velocities, other variables, wave height and period, are necessary for the calculation. These are determined from the resulting spectrum of the ADV measurements. This spectrum is the variance density spectrum of the surface elevation (Holthuijsen, 2007). The significant wave height ($H_{m_0}$) and mean period ($T_{m_{01}}$) are determined using the following set of formulas:

$$H_{m_0} = 4\sqrt{m_0} \tag{4.8}$$

$$T_{m_{01}} = \frac{m_0}{m_1} \tag{4.9}$$

Here, $m_0$ and $m_1$ represent the zeroth and first moment of the variance density spectrum. A n$^{\text{th}}$ moment of the variance density spectrum is defined as:

$$m_n = \int_0^\infty f^n E(f) df \tag{4.10}$$

The zeroth order moment, $m_0$, is therefore the total variance of the surface elevation. Lastly, the wave skewness ($Sk$), wave asymmetry ($As$), and Ursell number ($Ur$). These are calculated respectively using the following formulas ((Van der Lugt et al., 2024), (Holthuijsen, 2007)):

$$Sk = \frac{\overline{p^3}}{\overline{p^2}^{2/3}} \tag{4.11}$$

$$As = \frac{\overline{\mathcal{H}\{p\}^3}}{\overline{p^2}^{\frac{3}{2}}} \tag{4.12}$$

$$Ur = \frac{3\text{Hm0}k}{8(kd)^3} \tag{4.13}$$

## 4.4 | Data Analysis

In the last paragraph, it was explained how the raw data is processed into usable datasets. These datasets consist of elevation data for all the SRPLS measurements and wave statistics for the ADV measurements. In this paragraph, it is discussed how the needed data for the research questions is calculated with these data sets. First, the derivation of bed geometry and migration rates from the bed images is explained, and then the usage of the wave statistics from the ADV measurements.

### 4.4.1 | Ripple geometry

A method similar to the method used by Wengrove et al. (2017) is used to quantify the necessary variables, ripple wave height ($\eta$), ripple wave length ($\lambda$), and ripple crest orientation ($\phi_r$). A Two-Dimensional Fast Fourier Transformation (2DFFT) is performed over the x and y-grid. This results in a two-dimensional spectrum, with wave numbers in the x and y-direction as domain, shown in figure The peaks of that spectrum and their corresponding wave numbers are the wave numbers of the dominant wave in the footprint. Equation 4.14 and 4.15 are then used to calculate the ripples' wavelength and direction.

$$\lambda = \frac{2\pi}{\sqrt{k_x^2 + k_y^2}} \tag{4.14}$$

$$\phi_r = atan\left(\frac{k_y}{k_x}\right) \tag{4.15}$$

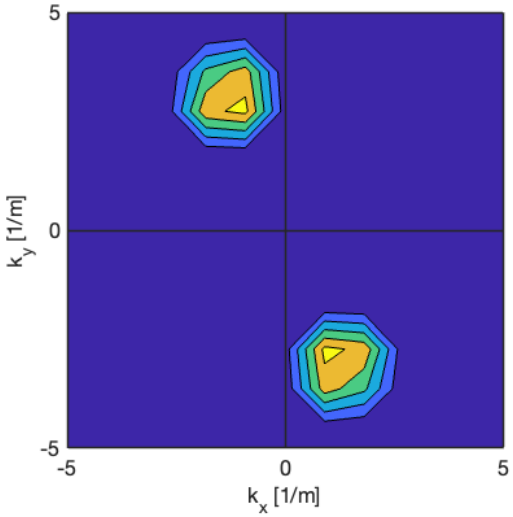


**Figure 4.13:** Spectrum resulting from a 2DFFT performed on the bed profile of figure 4.12.

To calculate $\eta$, equation 4.16 is used.

$$\eta = 4\sqrt{\iint \eta(k)^2 dk_x dk_y} \tag{4.16}$$

The spectrum of figure 4.13 can, however, not be used to determine $\eta$, because the 2DFFT is influenced by the lack of data around the circular footprint in the rectangular regular grid. This causes the volume underneath the spectrum to be smaller and that means that $\eta$ would be underestimated. Therefore, an additional 2DFFT is performed on a changed input grid. This input grid is now a square inside the footprint. To still have as many waves inside of this square, the image is rotated with the earlier calculated angle $\phi_r$ of the ripples. This results in the following input grid:

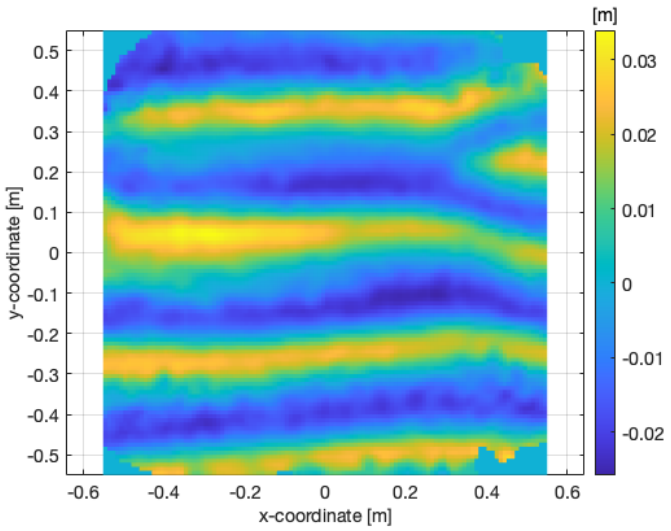


**Figure 4.14:** Rotated bed image for the computation of the spectrum for $\eta$. The ripples are now aligned horizontally, so that as many wavelengths are visible in this square.

The ripple geometry can now be determined for every measured footprint. This results in a dataset with ripple geometry for every 15-minute measurement.

#### Ripple predictor testing

The skill of ripple predictors from the Background will be tested in the analysis chapter. The accuracy is quantified using the root-mean-square error (RMSE). This is calculated with the formula:

$$\mathrm{RMSE} = \sqrt{\frac{\sum_{i=1}^{N} (x_i - \hat{x}_i)^2}{N}} \tag{4.17}$$

Here, $x$ is the measured variable, $\eta$ or $\lambda$, and $\hat{x}$ is the predicted variable by the ripple predictor for the same time, and $N$ is the total number of measurements.

### 4.4.2 | Ripple migration

The ripples can also migrate over the bed. This is again, visually not quantifiable, so a method is needed to determine a representative distance and direction that the ripples in the footprint have migrated in between two subsequent measurements. Figure 4.15 shows an example of two subsequent bed images where the ripples have migrated slightly to the upper left corner. The black line serves as a reference point in both of the images.

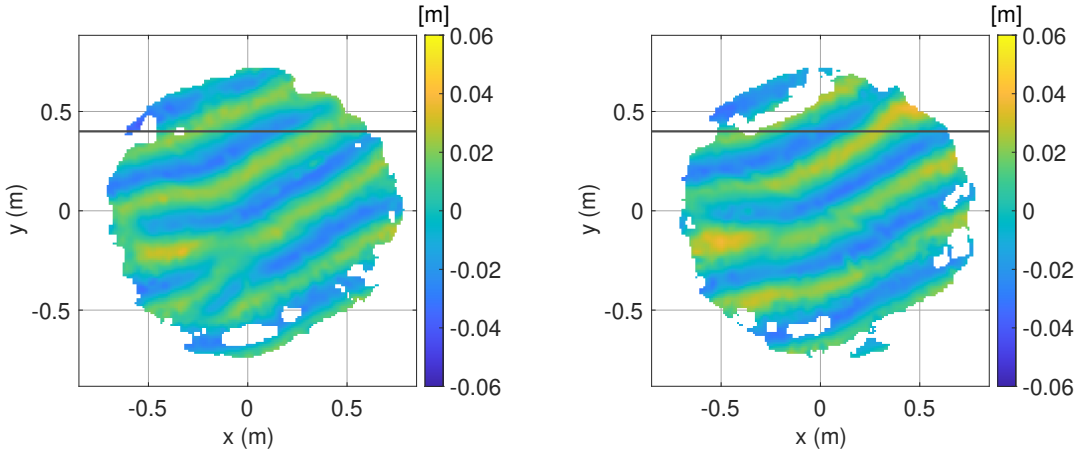


**(a)** First bed image **(b)** Subsequent bed image

**Figure 4.15:** Ripple migration. The black line is a reference point for both images.

The method that is used to quantify the migration is based on research by Wengrove et al. (2017; 2018). A cross-correlation between the two subsequent bed images, T0 and T1 is performed. The procedure of the cross-correlation is explained in Appendix C. The position of the highest cell in the cross-correlation matrix to its origin is the shifted distance of the ripples from T0 to T1, the migration. Since migration values will be in the order of $10^0 - 10^1$ cm (Wengrove et al. (2017; 2018)), only an area of 20 cm around the origin of the cross-correlation plot is investigated. For the images in figure 4.15, figure 4.16 shows the resulting cross-correlation matrix.

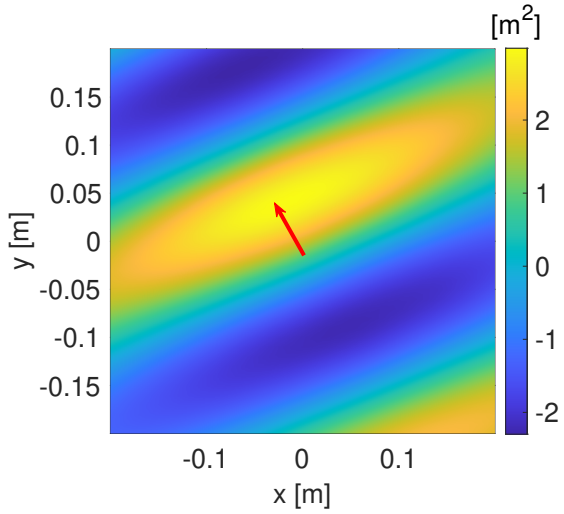


**Figure 4.16:** Cross-correlation values for the position of figure 4.15a over 4.15b

Using the coordinates, $x_m$ and $y_m$ of the peak of this matrix, the migration distance ($S_{mig}$), migration rate ($V_{mig}$), and migration direction ($\phi_{mig}$) can be determined using formulas 4.18 to 4.20:

$$S_{mig} = \sqrt{x_m^2 + y_m^2} \tag{4.18}$$

$$V_{mig} = \frac{S_{mig}}{t_s} \tag{4.19}$$

$$\phi_{mig} = \arctan\left(\frac{y_m}{x_m}\right) \tag{4.20}$$

### Sediment flux

The, sediment flux ($q_b$) can now be calculated. As formulated by Wengrove et al. (2018), the bed load transport equation, as the bed form itself, is assumed to have a sinusoidal shape. It is characterized using equation 4.21.

$$q_b = q_1 \cos\left[\frac{2\pi}{\lambda}\left(V_{mig}t - x_b\right)\right] + q_2 \sin\left[\frac{2\pi}{\lambda}\left(V_{mig}t - x_b\right)\right] \tag{4.21}$$

Here, $q_1$ and $q_2$ are estimated using:

$$n\eta\left[2\pi\left(\frac{t}{\lambda}\frac{\partial V_{mig}}{\partial t} + V_{mig}t\frac{\partial}{\partial t}\frac{1}{\lambda} + \frac{V_{mig}}{\lambda} - x_b\frac{\partial}{\partial t}\frac{1}{\lambda}\right)\right] = \frac{2\pi}{\lambda}q_1 \tag{4.22}$$

$$n\frac{\partial \eta}{\partial t} = \frac{2\pi}{\lambda}q_2 \tag{4.23}$$

The position along the bedform wavelength ($x_b$) and phase offset between the bedform shape and the function for transport ($\delta_{x_b}$) need to be determined. The phase offset is determined using formula 4.24:

$$\frac{\delta_{x_b}}{\lambda} = \frac{1}{2\pi}\tan^{-1}\left[\frac{\partial \eta}{\partial t}\Big/\left(2\pi\eta\left(\frac{t}{\lambda}\frac{\partial V_{mig}}{\partial t} + V_{mig}t\frac{\partial}{\partial t}\frac{1}{\lambda} + \frac{V_{mig}}{\lambda} - x_b\frac{\partial}{\partial t}\frac{1}{\lambda}\right)\right)\right] \tag{4.24}$$

When ripple height change is negligible the set of equations simplifies because, $q_2$ & $\delta_{x_b} \to 0$. However, this cannot be assumed beforehand, so initially a phase offset calculation is included. The change in migration rate $V_{mig}$ is also assumed to be nonzero and is determined between every subsequent bathymetry pair. Using equation 4.21 with equations 4.22 to 4.24 results in a method to find the bed load sediment flux at a position $x_b$ along the wavelength of the ripple with earlier determined characteristics $\eta$ and $\lambda$ and a time $t$. This time is a time in between the two subsequent bathymetry pairs. To calculate the average sediment flux of the migrating ripples, the sediment flux is integrated over time and then divided by the time. This leaves the variable $x_b$. Integrating over this variable and dividing results in a net zero sediment transport. The set of equations is developed to determine ripple growth or decay over time. The sediment transport flux over the bed is, therefore, zero and only locally nonzero to sustain growth or decay. To get an estimate of sediment transport in a ripple, the value of $x_b$ is set to zero. This means that the set of formulas only calculates the sediment flux at one point, the top of a ripple.

A different formulation of the sediment transport in a ripple is provided by Traykovski et al. (1999) and Kalra et al. (2022):

$$q_b = (1-\epsilon)f_r\eta_r V_{mig} \tag{4.25}$$

The bed porosity factor ($\epsilon$) is assumed to be 0.4 and the dimensionless ripple shape factor ($f_r$) is 0.5. This formulation is simpler and does not account for ripple height and length change during the subsequent bed images. The volume of ripple is calculated and multiplied with the migration velocity. Both of these formulas will be used to estimate the ripple sediment transport.
In chapter 3, the model XBeach was shortly introduced together with its incapability of producing the correct cross-shore profile of a sheltered beach. The model XBeach is used in this research to predict the cross-shore development during the SEDRIP campaign. The XBeach model was used without calibration in 1D surfbeat mode, (Halloween release 2023) (Roelvink et al., 2010). The hydrodynamic data from the ADV and a measured cross-section on the first day of the campaign are used as the model input. The sediment transport predictions from XBeach are then compared with the measured migration-induced sediment transport to see whether the sediment transport in ripple migration is of the same order as currently considered sediment transport mechanisms.

# 5 | Results

As described in the last paragraph, the ADV and SRPLS have carried out measurements. Before analyzing the results, the complete time series of measurements by both the ADV and SRPLS are discussed.

## 5.1 | Hydrodynamic measurements

The ADV has measured flow velocities in the cross-, long-shore, and vertical directions, together with the pressure sensor data the wave height, period, current-, orbital velocities, and water depth are computed.

### SEDRIP

Figure 5.1 shows the measurements over the SEDRIP campaign in November 2023.

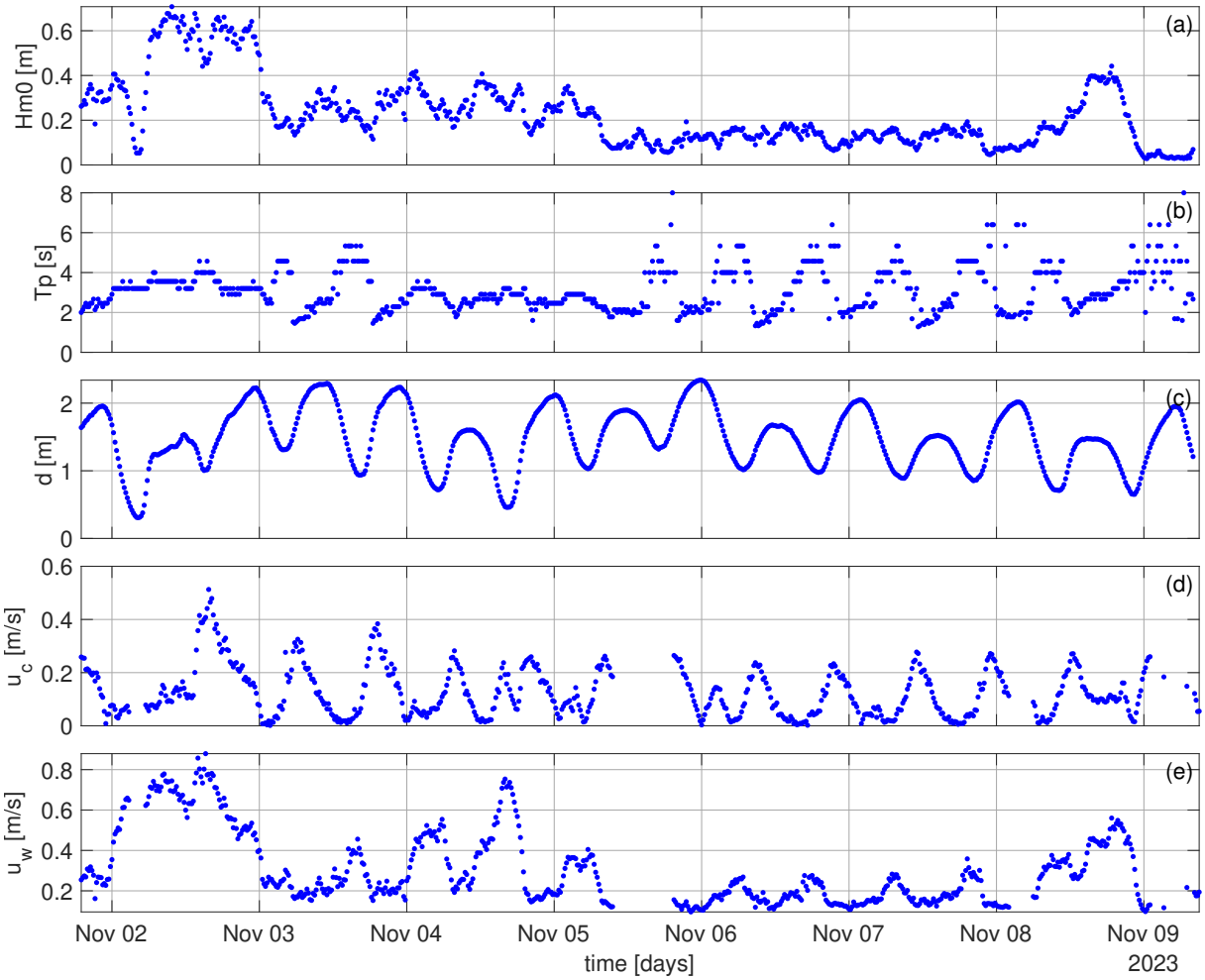


**Figure 5.1:** SEDRIP hydrodynamic results

The measurements were conducted when storm Ciarán took place (KNMI, 2023). During the storm, south-to-southeast wind velocities of up to 9 Bft. were reached. The storm occurred on 2nd November and is mainly visible in the high wave height and orbital wave velocities. Despite the high wind velocities, the maximum wave height was limited to 0.7 meters, which is around the first limit defined by Jackson et al. (2002) of 0.5 meters during storms. They also defined an upper limit to the significant wave height under non-storm conditions of 0.25 meters. This is, however, also exceeded

on multiple occasions. Indicating that the beach is a little more energetic than their description, but the conditions are of the same order.
Furthermore, two separate periods can be identified. From 2nd until 5th November, the waves are high and have a shorter period, and in the afternoon on the 5th this switches to lower waves with a longer period until the afternoon of the eighth. Both of these periods are still classified as gravity waves, indicating that only wind-generated waves arrived at the beach.

### SEDMEX

Figure 5.2 shows the hydrodynamic measurements during the SEDMEX campaign in September and November 2021. The period has been divided into four segments for better readability.

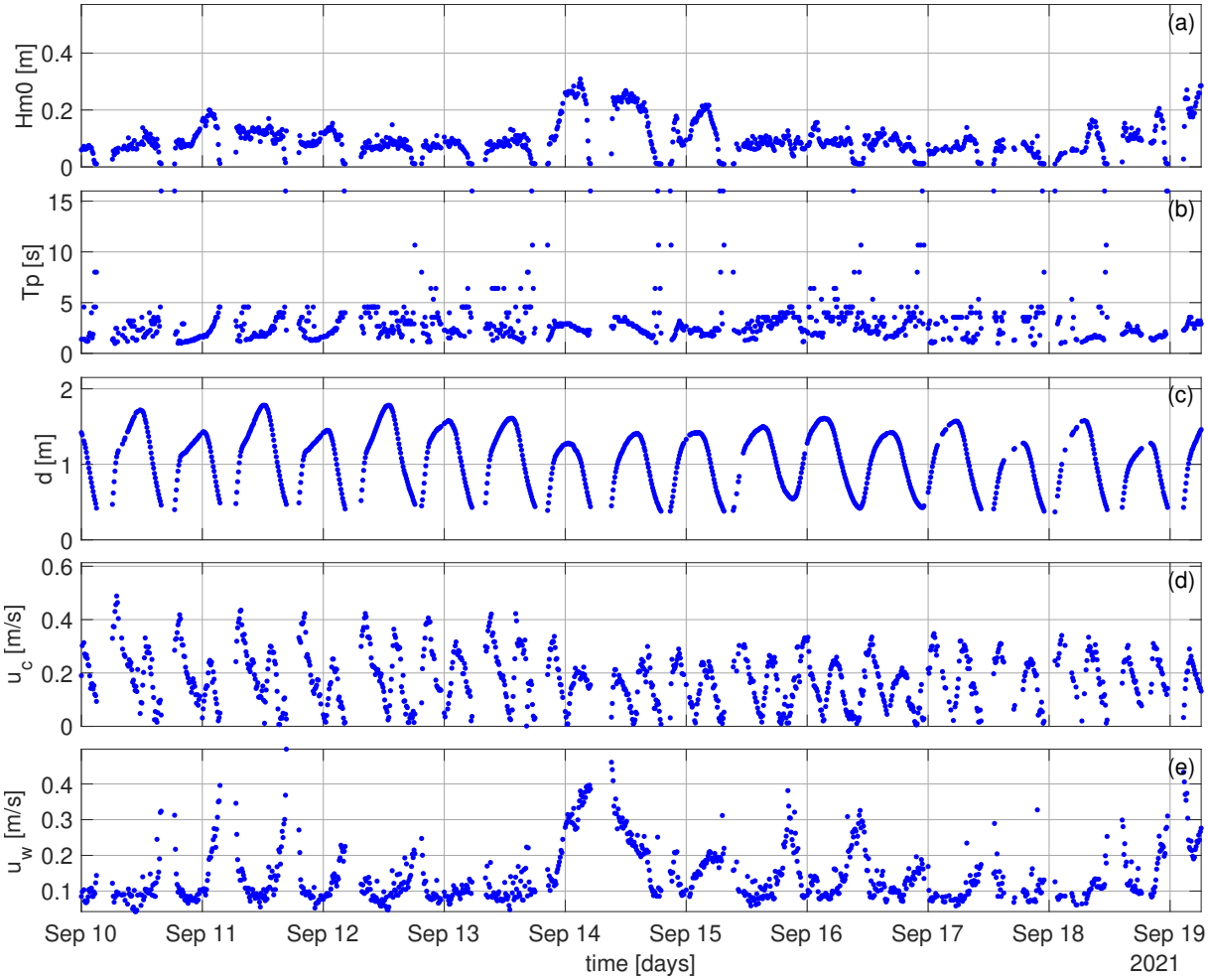


**(a)** First quarter of the SEDMEX results.

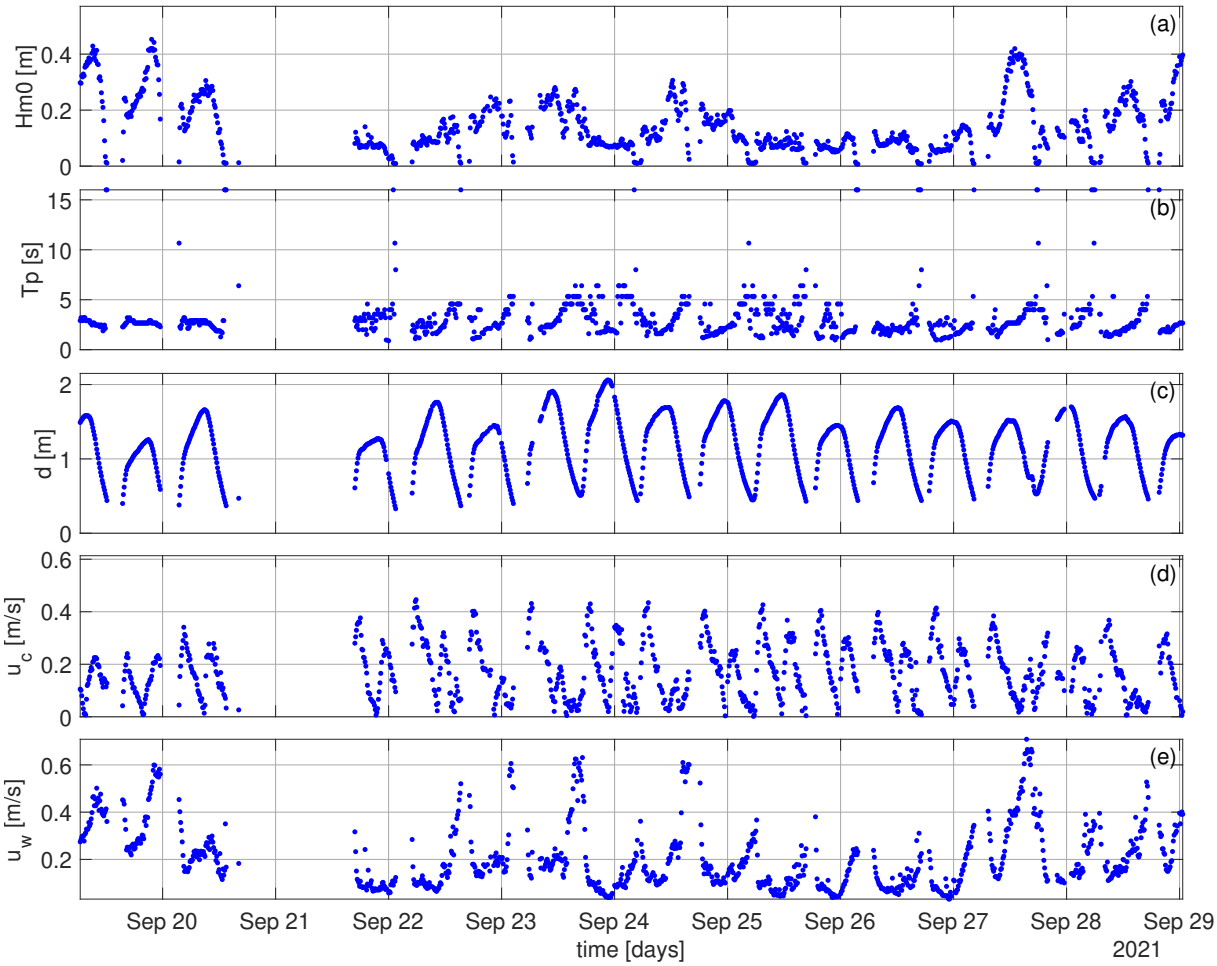


**(b)** Second quarter of the SEDMEX results.

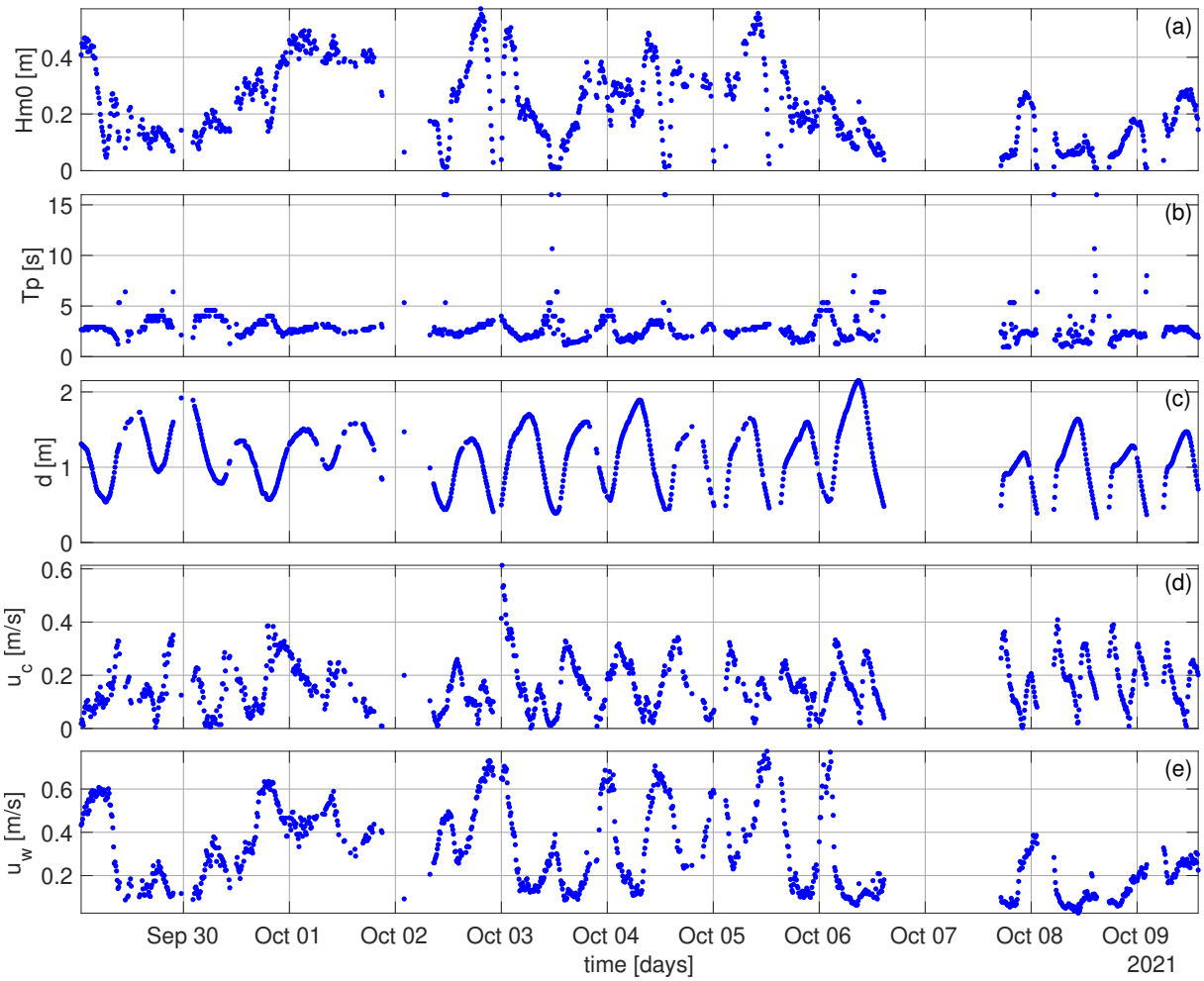


(c) Third quarter of the SEDMEX results.

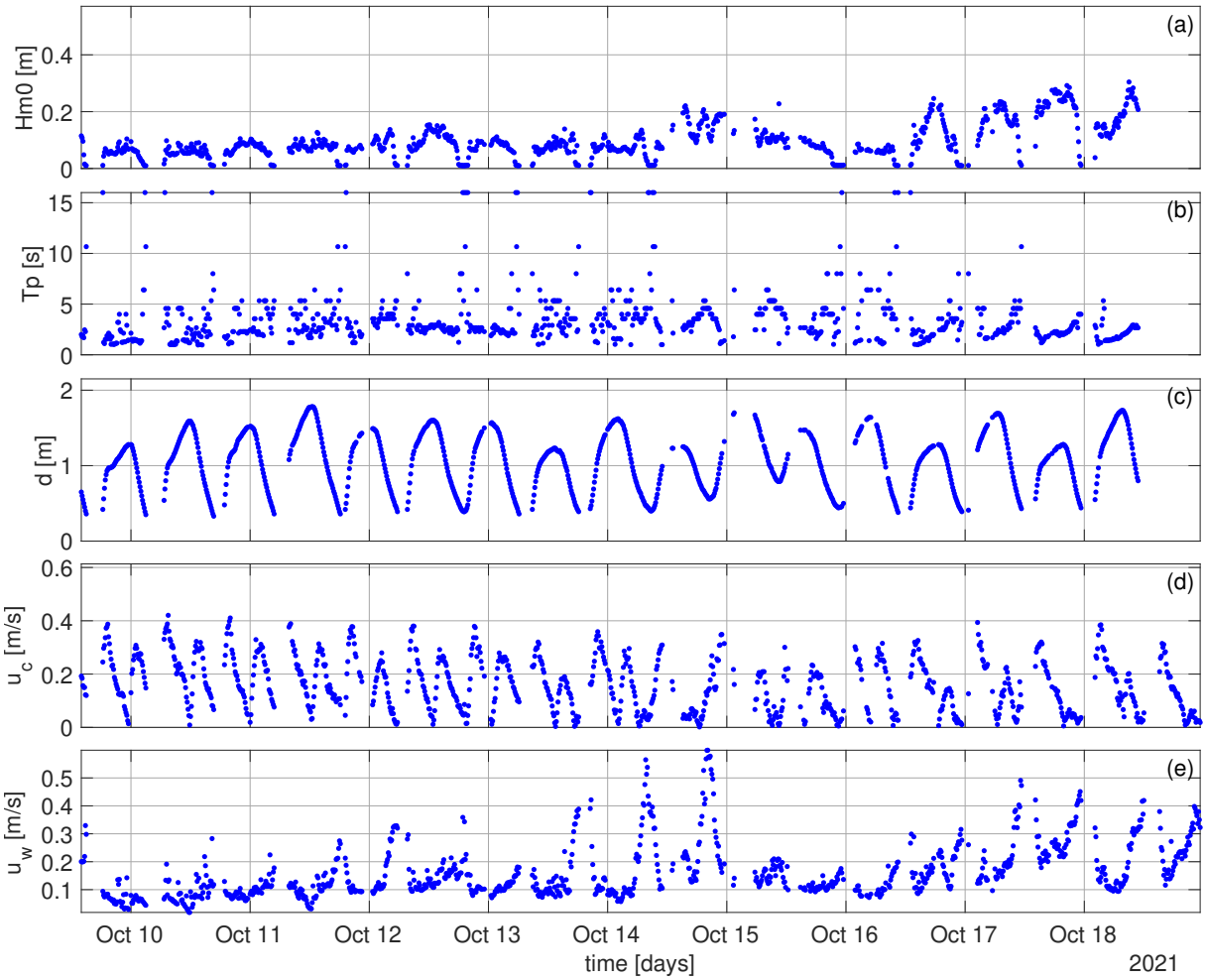


**(d)** Fourth quarter of the SEDMEX results.

**Figure 5.2:** SEDMEX hydrodynamic results.

The measurements during the SEDMEX show less energetic conditions, with wave heights of up to 0.57 meters. The maximum peak period that was measured was 16 seconds. These conditions are closer to the boundaries by Jackson et al. (2002) for storm and non-storm conditions. These conditions also indicate gravity waves, generated by wind.

### General

Overall, the relation between the orbital velocity and significant wave height is very visible. During higher wave heights, for example 14$^{th}$ September in figure 5.2a, the wave orbital velocity also increases. The higher waves cause a larger horizontal amplitude at the water surface, which also causes a larger horizontal particle excursion near the bed, see formula 4.7.
Also, the wave orbital shows a periodical trend that coincides with the tide. When the tide is lower, similar horizontal amplitude at the surface will also cause a larger horizontal particle excursion and velocity because of the relation of equation 4.7.

## 5.2 | Bed ripples

The sonar measurements from the SRPLS are used together with the method described in chapter 4, to develop a time series of ripple height and length for the SEDRIP and SEDMEX campaign. Figures 5.3 and 5.4 make a distinction between an absence of measurements and instances when the SRPLS has not measured ripples. When the device is not able to create an image of the bed, the plot is

marked in grey. This happens when the Sonar head is above the waterline or the combination of wave height and water depth caused the sonar head to not be submerged constantly. When the bed does not clearly show ripples the moment is marked in red. These markings remain the same throughout this report.

### SEDRIP

Figure 5.3 shows the measured ripple geometry by the SRPLS for the SEDRIP campaign.

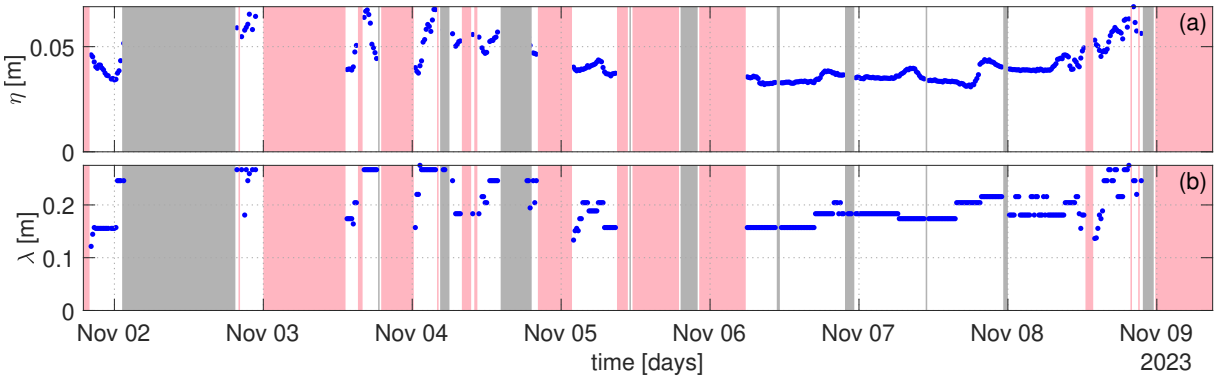


**Figure 5.3:** SEDRIP campaign ripple measurements

During the SEDRIP campaign, there was a significant amount of setup, which ensured that the sonar head was submerged most of the time, even during ebb. The large section without measurements on the 2nd November was caused by storm Ciarán. The wave height, significant wave height of about 60 cm, relative to the depth, about 1 to 1.5 meters, prevented the SRPLS from being constantly submerged. Also, measurements that were carried out while the device was submerged, did not show a bottom profile. This occurred on 2nd November when the highest waves of the SEDRIP campaign were present. It is assumed that the energetic conditions and wave breaking near the device, caused entrapped air in the water on which the sonar signal reflected as well. The other grey areas are caused by low waters due to ebb.

### SEDMEX

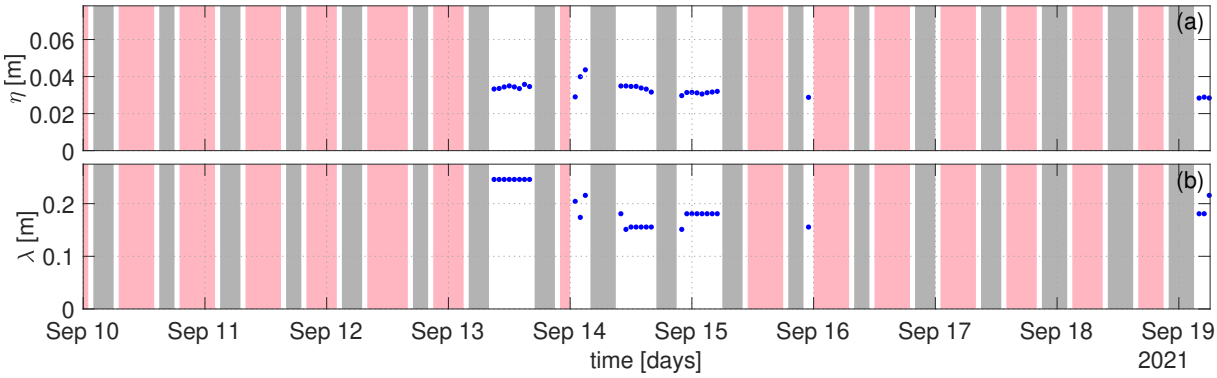


**(a)** First quarter of the SEDMEX SRPLS results.

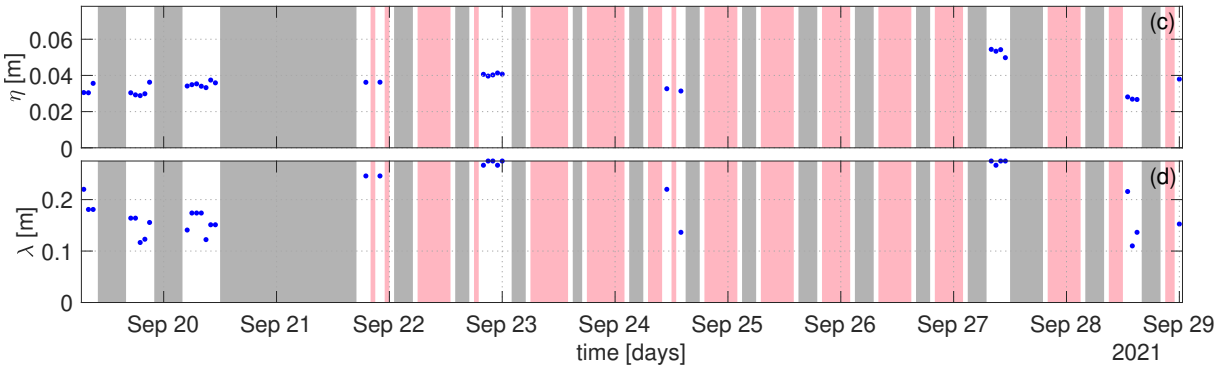


**(b)** Second quarter of the SEDMEX SRPLS results.

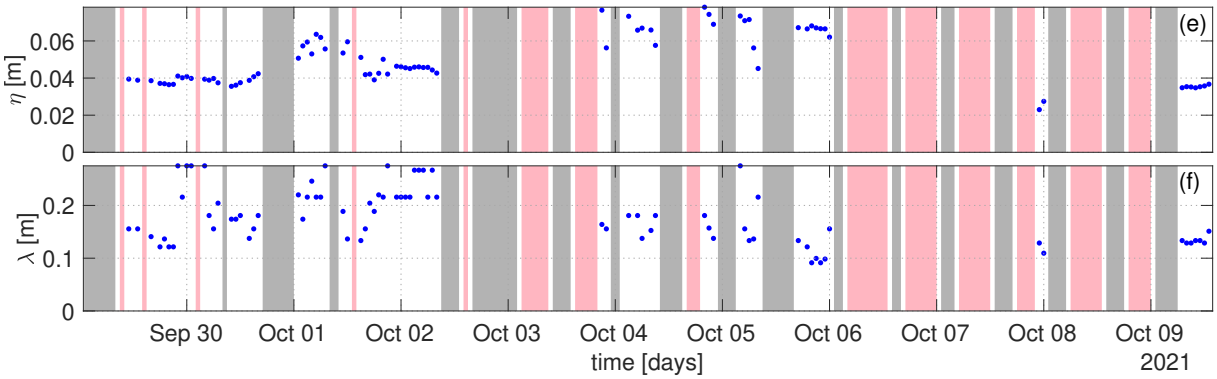


**(c)** Third quarter of the SEDMEX SRPLS results.

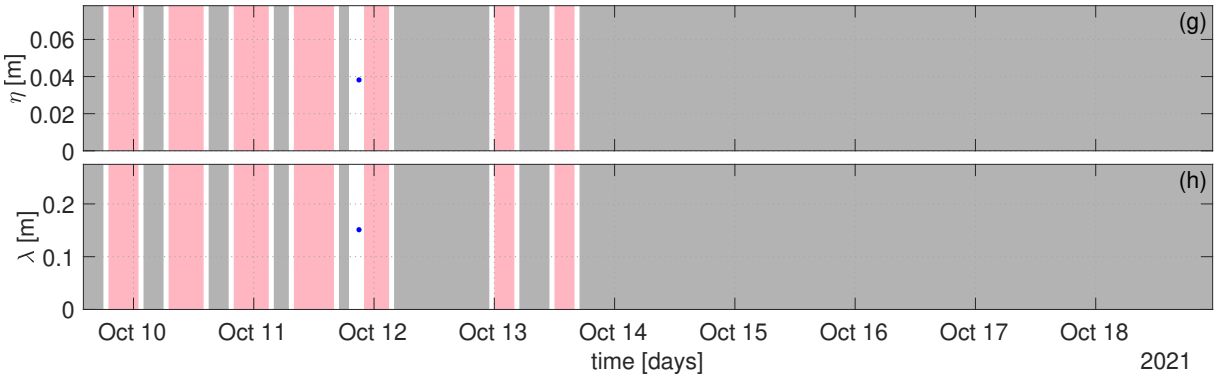


**(d)** Fourth quarter of the SEDMEX SRPLS results.

**Figure 5.4:** Measured ripple geometry over the SEDMEX campaign.

During the SEDMEX campaign, the sonar head was non-submerged more often. This has the effect that there are more times when it is unable to conclude whether there are ripples or not. Also, at the end of the time series, there are a couple of days where the device has not given output. The source of this is unknown.

Moreover, in general, during the SEDMEX campaign, the SRPLS measured fewer instances where ripples were visibly present on the bed. By observing the measurements in these periods more closely, it could be seen that an angle was present in the soil profile. This angle migrated in and out of the footprint. It could be that the frame where the device was located was close to a dynamic point of the cross-shore profile.

### General

Overall, ripples were present on the bed at multiple moments. The lowest measured ripple height was 0.023 and the highest was 0.0782 m. The shortest and longest ripple wavelengths were 0.091 and 0.275 m respectively. The presence of these ripples will be used in the next chapter to investigate whether the presence of the ripples can be related to the hydrodynamic conditions. Also, the discussed ripple predictors will be tested and the root-mean-square error of each three will be computed.

## 5.3 | Migration

Ripple migration was only measured during the SEDRIP campaign. The time interval between each measurement was 15 minutes, while its duration was about 5.5 minutes. During the SEDMEX campaign measurement time was longer, about 12 minutes, and two measurements were done back-to-back. Ripple migration during the 12-minute measurement time is therefore not visible, and back-to-back measurements do not have time in between to show any change. Figure 5.5 shows the 5 sets of migration that were noticed during the SEDRIP campaign.

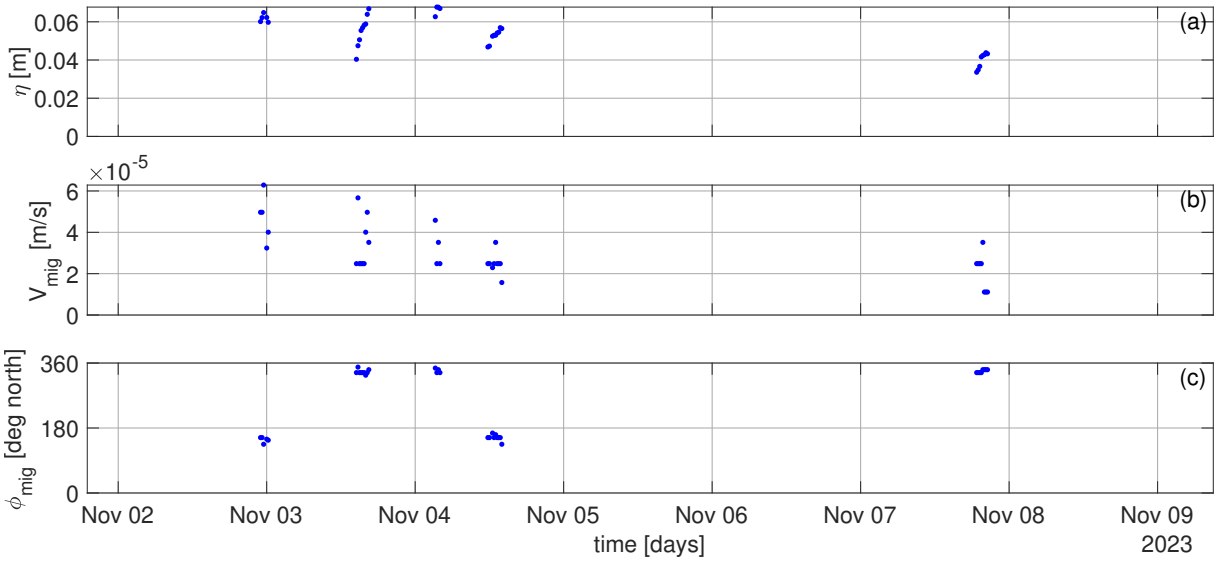


**Figure 5.5:** Migration during the SEDRIP campaign.

Over the SEDRIP campaign, ripple migration was noticed 5 times. In these cases, the ripple crests were visibly moving in the direction of the ripple orientation. The ripple migration velocity, $V_{mig}$, ranged from $1.11e^{-5}$ to $6.29e^{-5}$ m/s. These values fall into a lower range of migration velocities measured by Wengrove et al. (2017 & 2018). Their research was done on an open ocean coast in The Netherlands facing the North Sea. Measuring lower migration velocities on the sheltered beach at Texel is therefore expected.
In the next chapter, the presence of ripple migration and the driving mechanisms are discussed. Also, the measurements are used to estimate ripple sediment transport according to formulas 4.21 and 4.25, which are compared to the prediction of XBeach during the same conditions.

# 6 | Analysis

## 6.1 | Presence of ripples

### 6.1.1 | Driving mechanism

Bed ripples were present on the beach on multiple occasions. To forecast when there will be ripples and how large they will be, it is essential to determine what causes them and to which hydrodynamic parameter they respond best to. Instead of a time series, the measured ripples will be compared to the hydrodynamic conditions at the same time. In the literature, the mobility parameter is used widely to predict the presence and size of ripples. In chapter 3, three different mobility parameters were described:

$$\psi_{w;max} = \psi_{OD} = \frac{u^2_{w;max}}{(s-1)gD_{50}}, \qquad \psi_{VR} = \frac{U^2_{wc;VR}}{(s-1)gD_{50}}, \qquad \psi_{KO} = \frac{U^2_{wc;KO}}{(s-1)gD_{50}} \tag{6.1}$$

Here, the denoted $wc$ stands for the wave-current velocity. This is calculated differently for the $\psi_{VR}$ and $\psi_{KO}$ mobility parameters, see paragraph 3.5. The main difference between these three parameters is the absence of the current velocity in the parameter used by OD. This only uses the maximum orbital velocity near the bed. The relation between these three parameters and the dimensionless ripple dimension is shown in figure 6.1 This figure also shows a color grading for the fraction of the current velocity over the wave-orbital velocity.

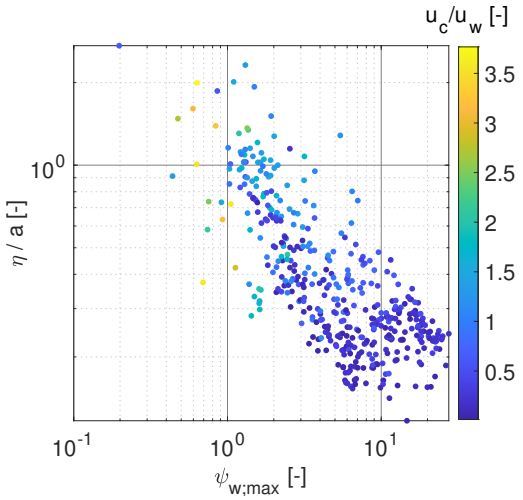


**(a)** Dimensionless ripple height for $\psi_{w;max}$, which leaves out the current.

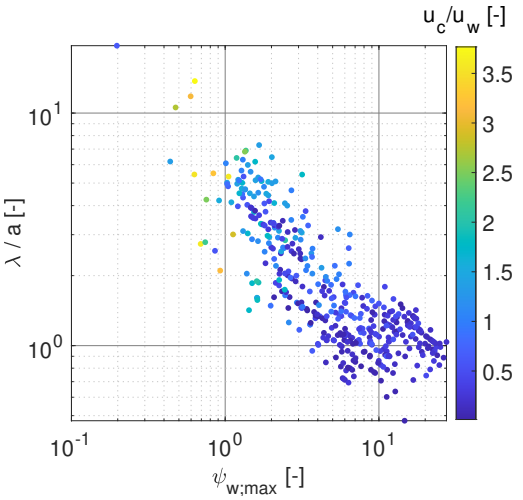


**(b)** Dimensionless ripple wavelength for $\psi_{w;max}$, which leaves out the current.

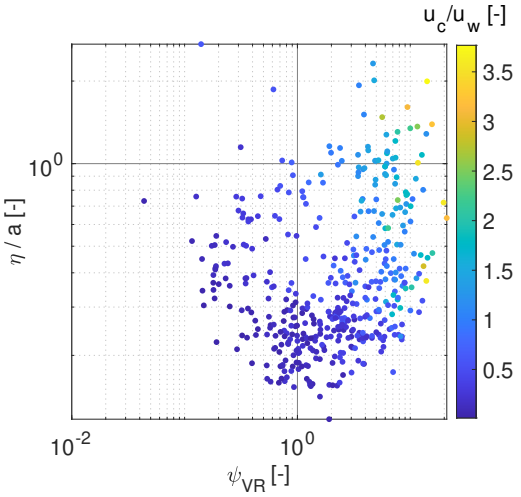


**(c)** Dimensionless ripple height for $\psi_{wc}$ by Van Rijn (2007), which includes the current.

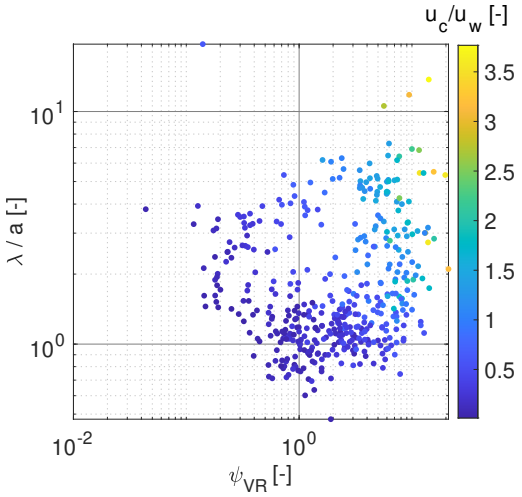


**(d)** Dimensionless ripple wavelength for $\psi_{wc}$ by Van Rijn (2007), which includes the current.

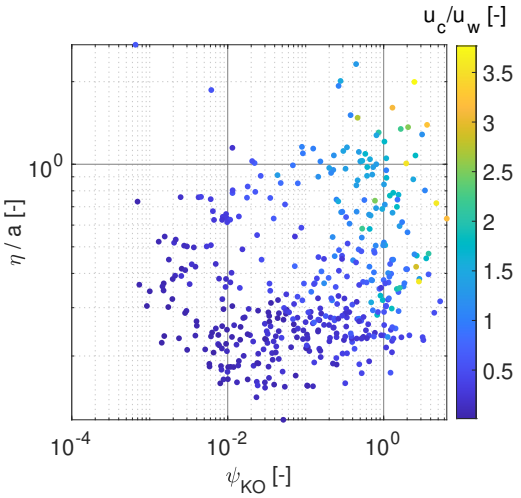


**(e)** Dimensionless ripple height for $\psi_{wc}$ by Khelifa and Ouellet (2000), which includes the current.

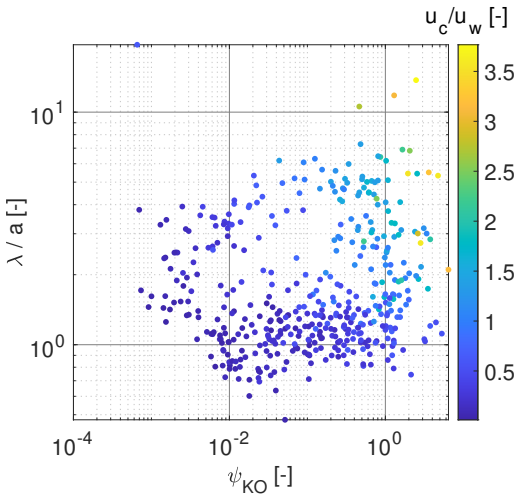


**(f)** Dimensionless ripple wavelength for $\psi_{wc}$ by Khelifa and Ouellet (2000), which includes the current.

**Figure 6.1:** Relation between the measured dimensionless ripple geometries and three different mobility numbers.

Figure 6.1 shows a difference between the mobility parameter that does not account for current velocities and the mobility parameters that do. The dimensionless ripple geometries do not follow a visible trend when relating them to the mobility parameters including current velocity, which is visible in figures 6.1c to 6.1f. Figures 6.1a and 6.1b show a trend for a declining dimensionless ripple height and wavelength with an increasing mobility number. For the lower values of $\psi_{w;max}$ higher dimensionless ripple height and longer wavelengths were measured. These values were accompanied by a higher fraction of current velocity over wave-orbital velocity. This could mainly be due to the fact that the current velocity varies periodically and that a lower wave-orbital velocity automatically means a high $u_c/u_w$ fraction at certain moments in the tidal range. Then, the larger dimensions are purely caused by lower wave-orbital velocities and a shorter particle excursion $a$. Figure 6.2 shows the dimensionless ripple geometry related to the fraction $u_c/u_w$ and uses a color grading to specify the wave-orbital velocity and the current velocity.

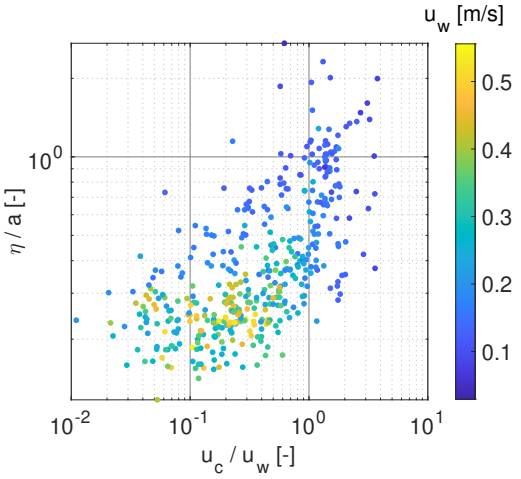


**(a)** Dimensionless ripple height, with a color grading for wave-orbital velocity.

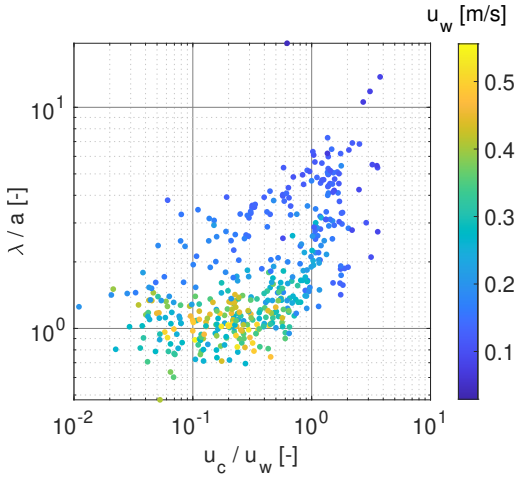


**(b)** Dimensionless wavelength, with a color grading for wave-orbital velocity.

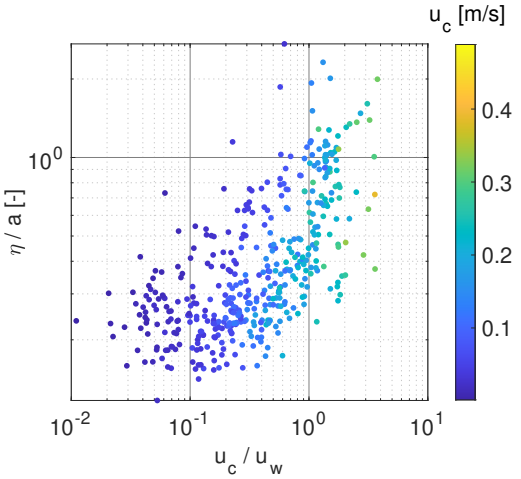


**(c)** Dimensionless ripple height, with a color grading for current velocity.

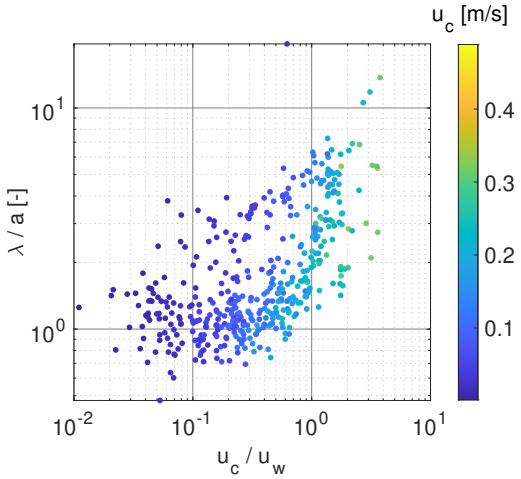


**(d)** Dimensionless ripple wavelength, with a color grading for current velocity.

**Figure 6.2:** Ratio of current velocity against orbital velocity for dimensionless ripple geometry. The color grading shows the value for the wave-orbital velocity and the current velocity to understand the ratio between the current and wave-generated velocity.

By comparing figure 6.2a with 6.2c and figure 6.2b with 6.2d, it is observed that a higher current velocity in combination with the absence of a wave-orbital velocity does not necessarily yield a larger dimensionless ripple geometry. In figure 6.2a and 6.2b it is visible that the color grading is mainly distributed over the y-axis. Here the wave-orbital velocity is distributed over the y-axis and does not seem to have a relation with the x-axis. There is a relation visible between the ripple dimension and the wave-orbital velocity. In figure 6.2c and 6.2d, the color grading mainly responds to the x-axis indicating a relation between the current velocity and the current-wave-orbital fraction.
The observations coincide with the conclusions drawn from figure 6.1. There is mainly a relation between the wave-orbital motion and the ripple geometry. The complete absence of a relation between the current velocity and ripple geometry is a conclusion that, however, cannot be drawn. It is observed that there are more values of larger dimensionless ripple height and wavelength for larger current velocities.
Other relations between ripple geometry and hydrodynamic forcing have been investigated. These were not found to add to the reasoning behind a conclusion. The associated graphs are included in Appendix A.

### 6.1.2 | Threshold for ripple formation

The best parameter to relate bed ripple geometry to was determined to be the mobility number that uses the maximum orbital velocity near the bottom. This mobility parameter is now used to identify whether clear thresholds can be found for the presence of bed ripples. Figure 6.3 shows the ripple height during the SEDRIP and SEDMEX campaign together with the $\psi_{w;max}$ for each measurement. The grey areas again show the absence of measurements, while the shaded red areas indicate that the algorithm has not detected ripples in the provided bed image.

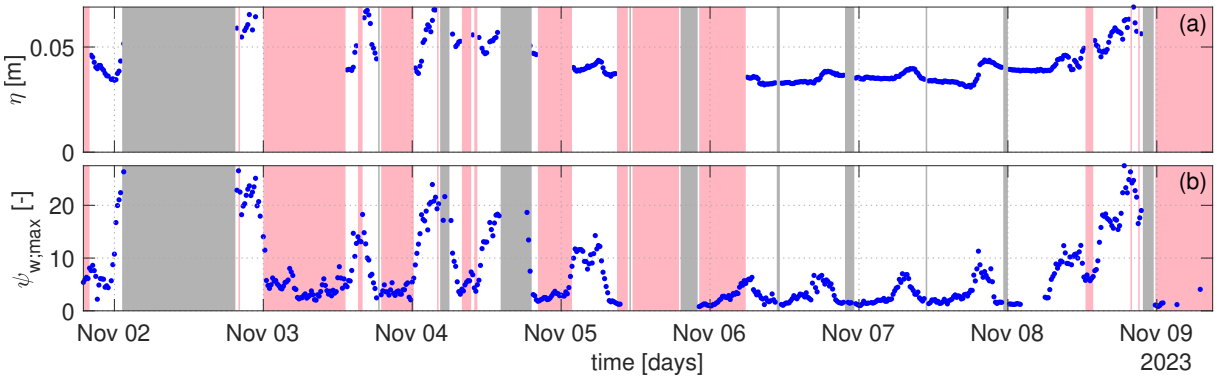


**(a)** Ripple presence during the SEDRIP campaign.

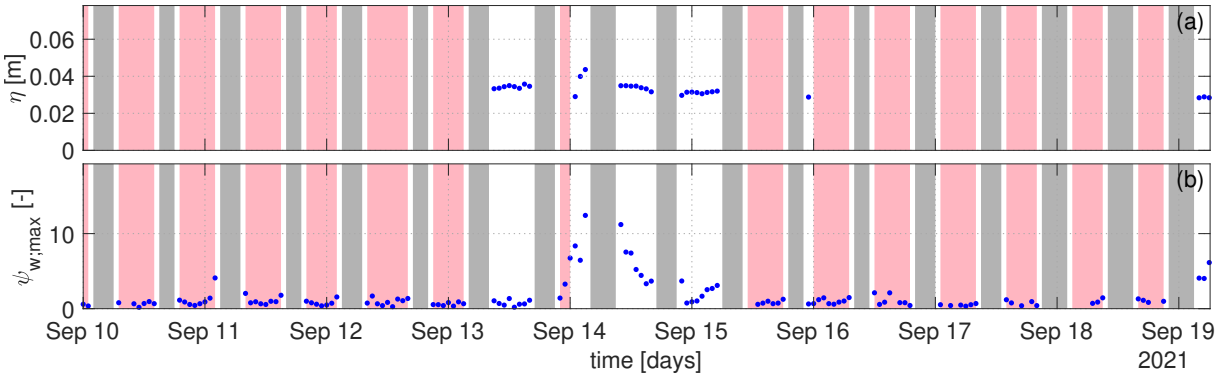


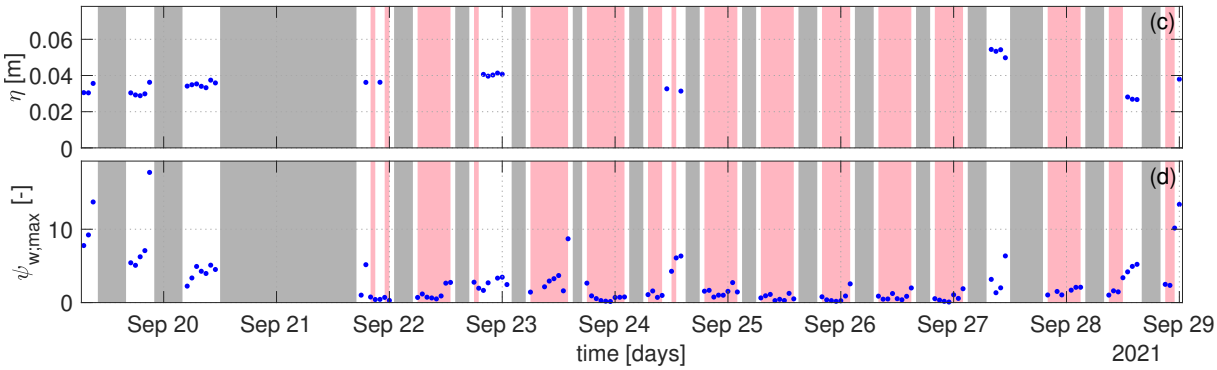

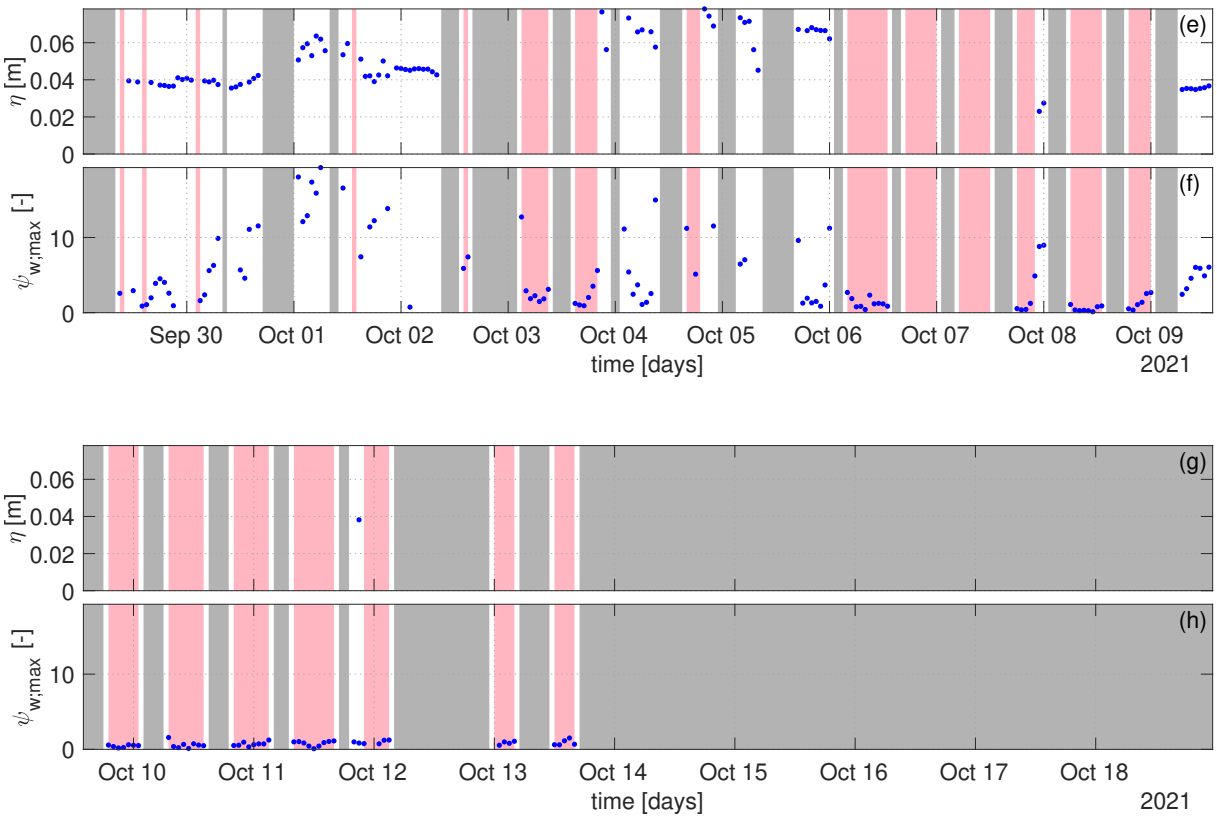


**(b)** Ripple presence during the SEDMEX campaign.

**Figure 6.3:** The ripple height is shown together with the mobility parameter $\psi_{w;max}$. The grey patches indicate the absence of data for the SRPLS. The red dots of the mobility parameter mark the instances where no ripples are present.

The first observation from these graphs is that the ripple's dimensions react to changing conditions. For example, during the period of 6$^{th}$ November through 9$^{th}$ November 2023, the ripples respond visibly to an increased mobility parameter with very little response time: For higher mobility numbers the ripple height increased accordingly. This shows that ripples are responsive to the forcing by the low-energetic wave climate on the sheltered beach.
Secondly, while the literature suggests that the beach is in the ripple-vortex regime when the mobility number, $\psi_{w;max}$, is below 100, ripples were not always measured on the bed. The hypothesis is that the low-energetic conditions can be so low that the sand grains on the bed are not mobile enough to form ridges and ripples. This is investigated by looking at four sub-samples from the presented SEDRIP and SEDMEX time series. These are highlighted in figure 6.3. The sub-samples all cover a period where the algorithm does not provide a ripple height, until, after a period of increasing mobility numbers, it suddenly does. Firstly, it must be identified how the bed looks like when the measurements show a lack of ripples. The bed is highly likely not completely flat, so what does it look like? Secondly, this question can be used to look at the development of the bed through increasing forcing by the waves. Does the increasing mobility number facilitate ripple formation? Figure 6.4 shows three bed profile images for each of these subsets that show the development of a rippled bed over time. The images show that indeed, ripples are not always present in an organized 2-dimensional form. The bed is in all of these cases not completely flat, but clear ripples are not visible. Throughout the sub-samples ripples are slowly formed.

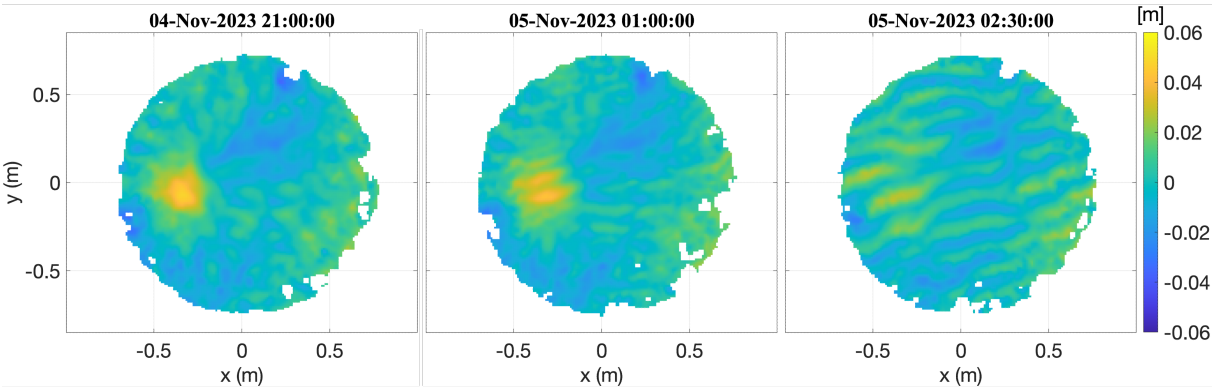


(a) Subset 1: 4 Nov 2023 19:30 - 5 Nov 2023 02:30

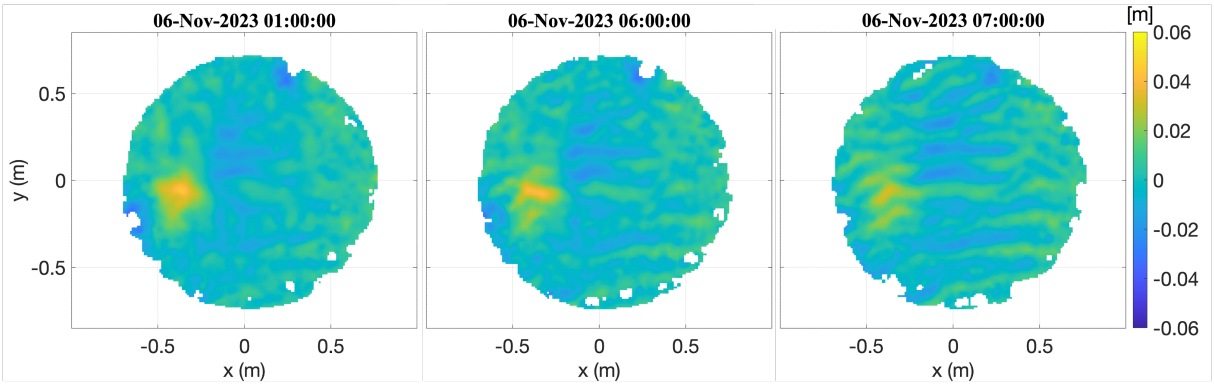


(b) Subset 2: 6 Nov 2023 00:00 - 6 Nov 2023 07:00

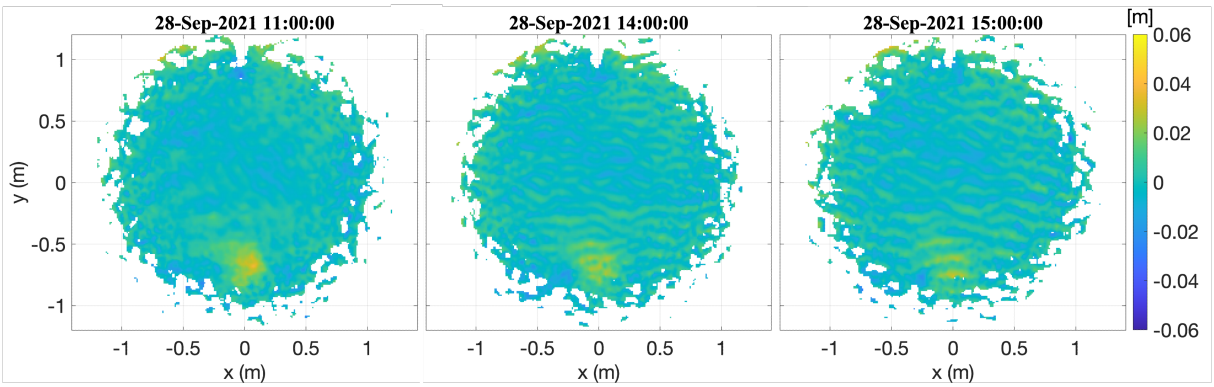


(c) Subset 3: 28 Sep 2021 11:00 - 28 Sep 2021 15:00

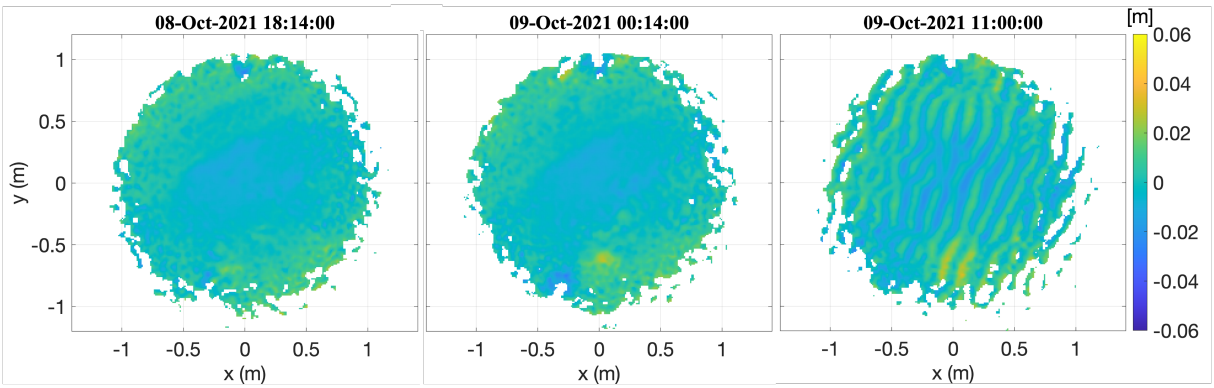


(d) Subset 4: 8 Oct 2021 18:00 - 9 Oct 2021 13:00

**Figure 6.4:** Ripple development over the 4 sub-samples. Notice the difference in the scale of the footprints. This is related to the different swath arc settings between the SEDMEX and SEDRIP campaigns.

The figure supports the literature that orbital forcing is necessary and that ripples are not formed instantly. It is a process where the sediment is organized in smaller pockets and ridges under wave-orbital forcing and eventually forms ripples. The algorithm recognizes the presence of ripples when the small pockets are connected and clear ripple crests are visible. The first image of the sub-samples represents the bed under the lower forcing. The second image shows a slightly changed bed with more organized spots of ripples when the mobility parameter has increased. The third and last image shows the developed rippled bed after the higher mobility number has allowed the sediment to organize itself into ripples. So, the low-energetic wave climate has enough energy to form and change ripples. Not once, but on multiple occasions.
Finally, it must be remarked that the two separate campaigns cannot be seen as equal. The measurements were done at the same location, however, for values of the mobility parameter that result in ripples at the SEDRIP campaign, there are no ripples present at the SEDMEX campaign. The inconsistency could be due to a different D50 that was present during the campaigns. This will be addressed in the discussion. Also, the time interval of the measurements was different.

## 6.2 | Ripple predictors

### 6.2.1 | Performance

When ripples are expected to be present, the discussed ripple predictors by OD, VR, and KO are used to predict the ripple geometry. For every measured ripple height and wavelength a predicted height and wavelength are computed using the simultaneous hydrodynamic conditions. Figure 6.5 shows the measured and predicted value for the ripple dimensions. If this value is above the black line it is an overestimation and below means an underestimation. Table 6.1 gives an overview of the accompanying RMSE-values for the predictors. In Appendix B, a full-time series of ripple predictions for both the SEDRIP and SEDMEX campaigns is shown.

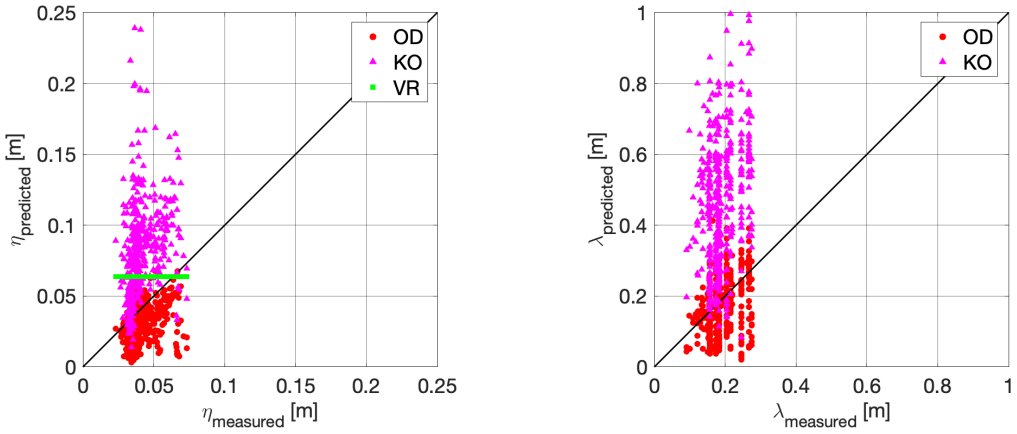


**(a)** Relation for the ripple height. **(b)** Relation for the ripple wavelength.

**Figure 6.5:** Measured ripple height and wavelength related to the predicted ripple dimensions. The VR predictor does not have a formula for the prediction of $\lambda$.

| Variable | $OD$ | $KO$ | $VR$ |
|---|---|---|---|
| $\epsilon_{\eta}^{rms}$ [m] | 0.019 | 0.053 | 0.024 |
| $\epsilon_{\lambda}^{rms}$ [m] | 0.080 | 0.36 | - |

**Table 6.1:** Root-mean-square errors of the ripple predictors.

From this graph, three observations can be made. Firstly, the predictor by Van Rijn (2007) results in a constant predicted ripple height of $0.0637\ m$. Equations 3.11, 3.13, and 3.14 show why this

happens. VR states that the ripple height is fully developed and constant for $\psi_{VR} \leq 50$. During all of the measurements the mobility number is smaller than 50, and, therefore, the predicted ripple height will be constant at $150 f_{cs} D_{50}$. Secondly, the predictor by KO almost constantly over-predicts the ripple height and wavelength., while the predictor by OD seems to underpredict the ripple dimensions, although this is less severe than the predictor by KO. This is also verified by the RMSE for the ripple height and wavelength. The predictor by KO has the largest error. This is understandable since figure 6.5 shows that KO suggests dimensions twice as high or even more than measured. Although the predictor by VR shows a constant ripple height, the error is less than half of the error for KO and is very similar to the error for OD.
Overall, the average measured ripple height is 0.042 meters and the average wavelength is 0.192 meters. This means that the RMSE of KO for the ripple height and wavelength is larger than the average values. The predictors from OD and VR have errors that are about half the average ripple dimensions. The predictor by KO performs worst out of the tested three ripple predictors.

### 6.2.2 | Impact of the current

In paragraph 6.1, it was discussed that the current did not have a clear relation with the ripple dimensions. The predictors from KO and VR both include the current in their mobility parameters. Since these parameters were proven to not show a visible trend with the dimensionless ripple height and wavelength, see figure 6.1c to 6.1f, it is tested whether the exclusion of the current in the calculation of the mobility parameters yields a smaller RMSE. In figure 6.6, the same comparison is made as in figure 6.5, but the current velocity is set to zero.

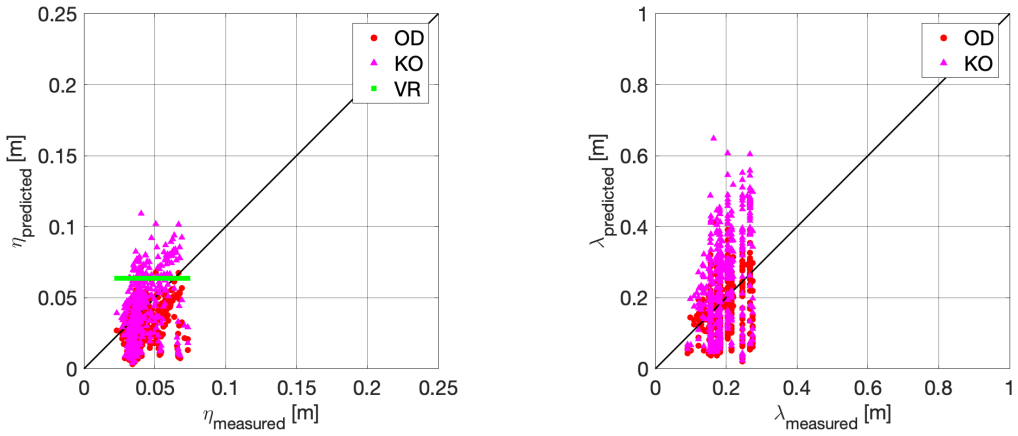


**(a)** Relation for the ripple height. **(b)** Relation for the ripple wavelength.

**Figure 6.6:** Measured ripple height and wavelength related to the predicted ripple dimensions. The VR predictor does not have a formula for the prediction of $\lambda$. The current is set to zero in the calculation of all mobility parameters.

| Variable | $OD$ | $KO$ | $VR$ |
|---|---|---|---|
| $\epsilon_{\eta}^{rms}$ [m] | 0.019 | 0.020 | 0.024 |
| $\epsilon_{\lambda}^{rms}$ [m] | 0.080 | 0.14 | - |

**Table 6.2:** Root-mean-square errors of the ripple predictors using a zero current velocity.

Firstly, the values for the VR predictor have not changed, since the mobility parameter will only become smaller when the current velocity is not included. This also means that the error remains the same. Secondly, the error for the KO predictor has reduced from 0.053 to 0.020 for the ripple height

and from 0.36 to 0.14 for the ripple wavelength. This indicates that the predictor by KO weighs in the influence of the current too much.

## 6.3 | Ripple migration

Ripple migration was noticed five times, see figure 5.5. First, this paragraph discusses the driving mechanism behind the migration. This is followed by a comparison between the measured bed load transport and the bed load transport calculated by XBeach at the same time.
Figure 6.7 shows six hydrodynamic values together with the measured sediment transport by ripple migration. The existence of ripple migration was related to the presence of wave skewness in literature, see chapter 3. Panel **b** shows the near-bed orbital velocity skewness. If this graph is compared to the first panel, **a**, it is clear that indeed there is skewness during the migration of ripples. On 6$^{th}$ and 7$^{th}$ November there is also an increased skewness in the velocity signal, but no measured migration. It is expected that this was caused by the very low mobility numbers that accompanied these skewed waves, which meant that the sediment grains did not have enough forcing to become mobile.
Ripple migration, therefore, seems to respond to wave skewness on the sheltered beach. However, a second observation of the migration time series was the difference in migration direction: three events had onshore migration, while two events had offshore migration. The difference in migration direction cannot directly be determined from the wave skewness time series. The hypothesis for the cause of different migration directions lies in the balance of forcing on the sediment particles on the bed. A net onshore total balance by wave skewness should yield onshore bed-load transport, as discussed in chapter 3. A net offshore balance of forcing should therefore cause offshore ripple migration. In the literature, negative wave skewness was pointed out as the driving mechanism, but during the SEDRIP campaign, little to no negative skewness was measured. It is observed that the offshore migrating ripples had lower wave skewness values than the onshore migrating ripples. The lower positive skewness causes less onshore forcing, which could leave the sediment particles vulnerable to offshore transport by for example an offshore directed current near the bottom, undertow.
Additional parameters are included in figure 6.7 to try and understand the forcing for the different migration directions. Several observations are made, with a focus on finding differences in the forcing between instances of offshore and onshore migration:

- The moments that migration was measured are those with higher mobility parameters, panel **c**. The higher mobility parameter enables particle mobility on the bed. There is not a clear distinction between the values of the mobility parameter during on- and offshore migration. It is therefore only seen as an enabler of ripple migration, but not as a mechanism that can either transport particles on- or offshore.
- Panel **d** shows the asymmetry of the waves. A distinction is noticeable between the instances with off- and onshore migration. While a significant negative asymmetry always accompanies onshore migration, offshore migration is not accompanied by similar asymmetry.
- The direction of the current, shown in panel **e**, does not have a trend with the direction of the ripple migration. For both on- and offshore migration instances, different current directions were measured.
- The same holds for the peak wave period in panel **f**. Various periods were found during both on- and offshore migration.
- At last the Ursell number in panel **g**. Again, a difference between on- and offshore migration moments is visible. During both offshore migration instances, the Ursell number was around 0.1, while this value was between 0.3 and 0.4 during onshore migration, which indicates that onshore migration is supported by more non-linear waves.

The two parameters skewness and asymmetry, together with the wave non-linearity parameter, the Ursell number, are identified to show the clearest relation with the direction of the migration. Where larger values of skewness, asymmetry, and the Ursell number accompany onshore migration, while values closer to zero are related to offshore migration. The hypothesis is that the smaller wave asymmetry, skewness, and Ursell number generate less onshore forcing, which is not enough to

overcome offshore forces, like undertow. The result is a net offshore bed load transport. This is a hypothesis and should be proven in future research.

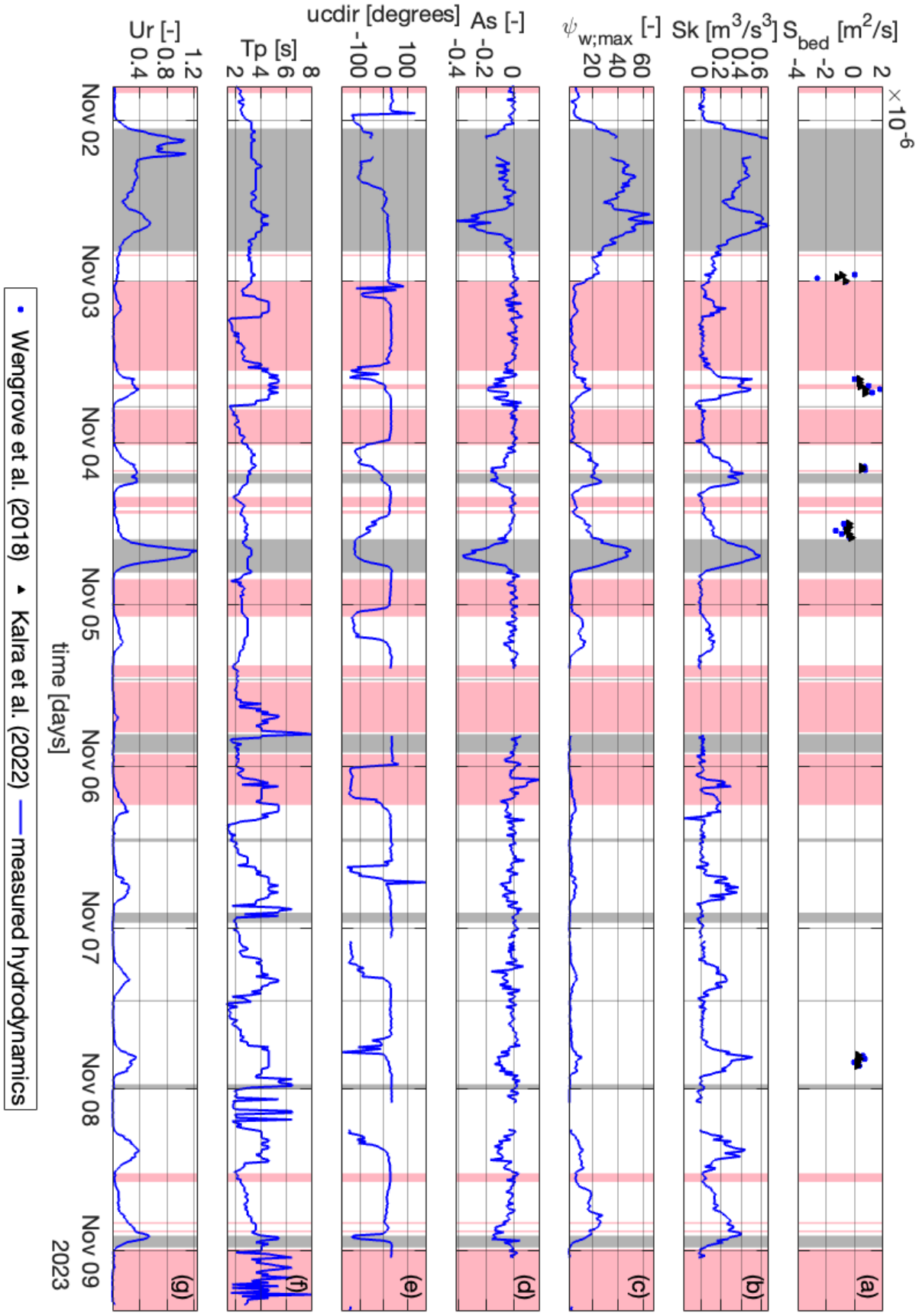


**Figure 6.7:** Migration during the SEDRIP campaign compared with several hydrodynamics statistics: **a**, bed load sediment transport; **b**, wave skewness; **c**, mobility parameter; **d**, wave asymmetry; **e**, current flow direction; **f**, peak wave period; **g**, Ursell number

Lastly, a comparison is made between measured bed load transport and calculated transport by XBeach. Figure 6.8 shows the resulting bed load transport calculated by the formulas from Wengrove et al. (2018) and Kalra et al. (2022). XBeach has computed sediment transport in the long- and cross-shore direction over the entire cross-section. 6.8 shows the calculated bed-load transport by the model at the location of the frame of the devices.

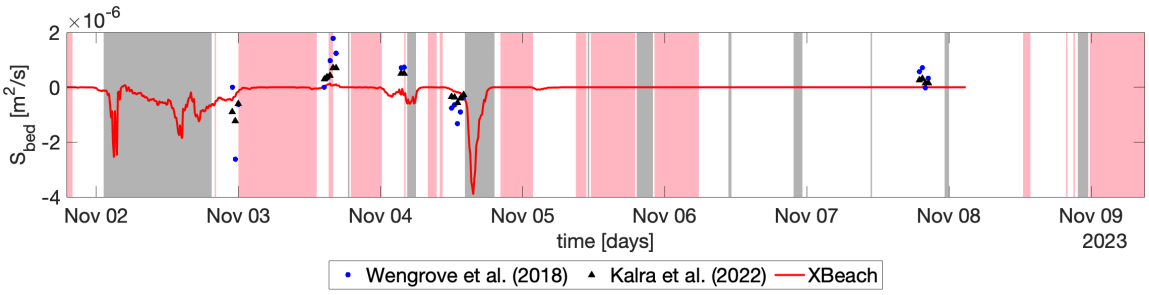


**Figure 6.8:** Cross-shore bed-load sediment transport at the frame's location calculated by XBeach compared with the measured ripple migration-related transport.

Of the 5 stretches of migration, 2 were directed offshore (negative) and 3 onshore (positive). The bed load transport that is measured is of the same order as the calculated bed load transport by XBeach. However, the bed-load transport that is computed by XBeach is almost always offshore. Only during the afternoon of 3$^{rd}$, the XBeach calculated transport is directed onshore. However, this is of a different order compared to the measured bed-load transport.
Considering the driving mechanism behind ripple migration, skewness, it is expected that the ripple migration takes place over a wider area, namely the underwater plateau of the beach. Waves become skewed when they arrive in shallow water. The underwater plateau at this sheltered beach is almost completely horizontal. So, if waves are skewed near the frame, which is on the plateau, the waves are also expected to show skewness over the other stretch of the plateau, and migration could be present over a larger part of the cross-section. Making this form of transport an integral part of sediment transport over the cross-section.
In general, migration was visibly related to the presence of wave skewness, asymmetry, and the Ursell number. The direction of the migration is a result of induced forcing by these parameters, but a clear cause was not found. The measured ripple migration rates and the induced sediment transport were of the same order as the computed bed load transport by XBeach.

# 7 | Discussion

In the previous chapter, the results were analyzed in three categories: ripple presence, predictors, and migration. Before concluding the research questions, this chapter provides explanations for certain sources of uncertainty and discusses the broader picture of this research and its relation to recent studies.

## 7.1 | Uncertainty

### 7.1.1 | Direction inaccuracy

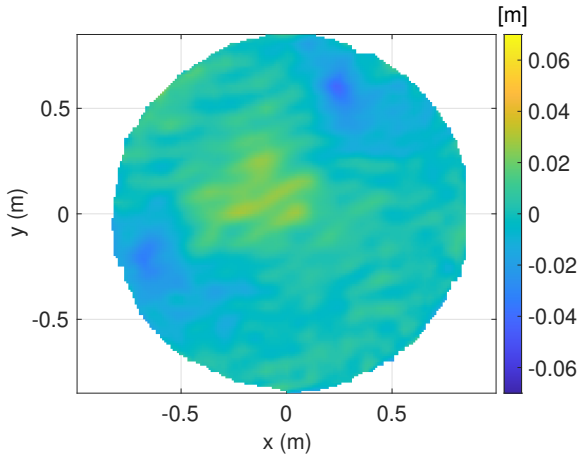


**Figure 7.1:** Visibility of poles in the cross section

The SRPLS does not have a visual zero-axis for the installation. This means that the correct orientation of a bed profile, as shown in figure 7.1, needs to be created by post-processing. The bed profile is rotated so that the upper part of the image corresponds with the 0 degrees North. The orientation of the device and rotation correction are performed by identifying known objects in the bed image. The blue circles at (-0.6; -0.2) and (0.3; 0.6) are the poles of the frame in between where the SRPLS is mounted. The location of these poles on the beach was known. By rotating and scaling the bed image correctly over these 2 points, the rotation and orientation of the SRPLS is determined. This is done for several images and averaged. However, the method is still visual. The position of the poles in the bed image is not entirely clear and identifying the correct position will be inaccurate with an order of centimeters.
By identifying a slightly wrong position of the poles in the bed image, an error in the orientation of the ripples and migration direction is induced. Therefore, in the analysis, the direction of the ripples is not considered, and the ripple migration direction is only interpreted as onshore or offshore.

### 7.1.2 | Impact of frame poles

Figure 7.2 again shows a bed image, in which the the poles of the frame are very visible, namely the white circles near the edge of the circular footprint. Another feature on the bed is the orange bump in the bed level northeast of the pole on the west of the image. This hump is not always present and is therefore not a consistent feature of the bed. It migrates into the images from the west pole and after some time migrates out of the picture to the west again.

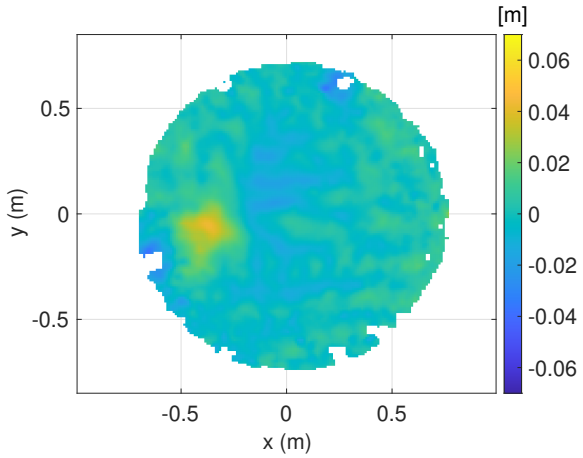


**Figure 7.2:** Visible disturbance on the bed by the southern pole

It seems that the existence of the bump is related to the current in combination with little to no wave-orbital forcing, because the bump is visible in the period when there are no ripples on 6$^{th}$ November, see figure 6.3a. During this period the wave forcing is also very low, see figure 5.1. Turbulence around the pole, caused by the current velocity, is expected to stir up sediment that is deposited in the footprint of the SRPLS. The bump is created during the higher currents associated with a rising tide. That is in the northeast direction in the figure. When the flow direction changes, the bump is washed away, and the northern pole does not influence the creation of a bump originating from that pole.

### 7.1.3 | Sediment grain size

The median diameter of the sediment in the beach varies a lot over the length and cross-section of the beach. The sediment size is used in the mobility parameter for all of the predictors and in the VR predictor it is also used in the correction factor for the grain size. Figure 7.3 shows how the RMSE of the predictors changes when a different D50 is assumed.

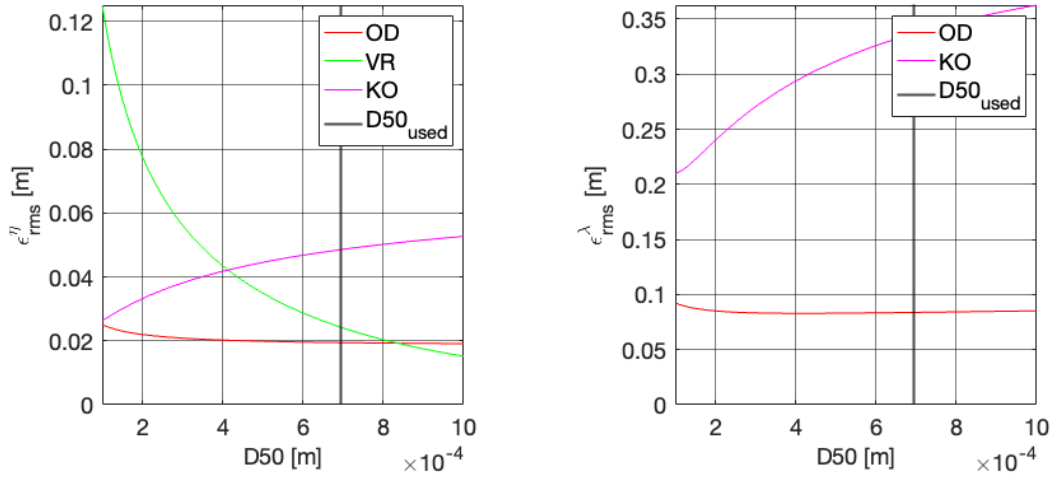


**(a)** D50 and the RMSE of the $\eta$. **(b)** D50 and the RMSE of the $\lambda$.

**Figure 7.3:** The influence of using a different value for D50 on the RMSE of the ripple height and wavelength prediction.

Firstly, the RMSE of the predictor OD is not affected and remains stable while different sediment sizes are used. The predictor by VR changes the most over a range of D50 values. The predictor KO

is also significantly impacted by the change in D50 input.
The performance of the ripple predictors was analyzed in chapter 6 and the conclusion was drawn that the KO predictor performed worst out of the three. Figure 7.3 shows, however, that the impact of a different choice for D50 impacts this conclusion. The choice for D50 was based on field measurements done during the SEDMEX campaign in 2021, while some of the ripple data was measured in 2023. Also, the sediment size varied over the beach. Both longshore and over the cross-section. During the week sediment conditions might also be impacted since more energetic conditions could transport a lot of sediment away or to the measurement location. This uncertainty in the sediment size at the beach and the impact that changing the sediment size in the computation has, must be taken into account when concluding the performance of a ripple predictor.

### 7.1.4 | Ripple predictors

The different ripple predictors are developed and tested during specific circumstances. The predictors can be developed using lab conditions or fieldwork data. Also, the sediment used in the lab or encountered at the fieldwork site can differ. The predictor by OD was developed using a flow tunnel in a laboratory. Their predictor was developed and verified for wave-orbital forcing, and three sizes of sediment: D50 = 220, 350, and 440 $\mu m$. The predictor by VR was fitted on a large set of field test data and has the widest range of validity. The tested sediment size ranges from D50 = 20 - 2000 $\mu m$. The last predictor, KO, was developed and tested for lab conditions. They used a basin where a current could be added to the wave-climate, as well as different angles between the current and the wave-orbital velocity. The sediment sizes that were used are D50 = 150 and 500 $\mu m$. Table 7.1 summarizes these conditions for the three used predictors:

| Predictor | Site | D50 [$\mu m$] | Additional comments |
|---|---|---|---|
| OD | Tunnel | 220, 350 & 440 | Only waves, no current |
| VR | Field | 10 - 2000 | Developed using a large set of fieldwork-obtained data. |
| KO | Basin | 150 & 500 | A basin used different angles between the current and wave-orbital motion. |

**Table 7.1:** Limitations of the used ripple predictors

These predictors are now used and verified for a fieldwork site with a different sediment type than the predictors OD and KO. Also, as described in the previous paragraph, the sediment class of the beach is very unpredictable. The answer to the second research question on the performance of the ripple predictors must be read with the notion that, mainly the predictors OD and KO, were used in circumstances that they were not verified for.

### 7.1.5 | Lack of data for ripple migration

During the SEDRIP campaign 5 periods were found when migration took place, see figure 5.5. The duration of the migration was in the order of several hours. So, in 8.5 days, a couple of hours of ripple migration was measured. The conclusion that these are the only times ripple migration is present is incorrect. At the location of the frame and when the SRPLS was able to collect a bed profile, these were the only times when migration was visible. However, during shallow water levels combined with a high skewness, the SRPLS was above the water, resulting in a lack of data. Also, migration could be present a little higher or lower in the beach profile, when none was measured at the frame. The conclusion that migration was present 5 times over the SEDRIP campaign proves that there is ripple migration at the sheltered beach and that it is driven by skewness. A more complete image could be made for the entire cross-section, this is discussed in the next chapter.

## 7.2 | Relation to previous research

In chapter 3 the distinction was made between open sea coasts and sheltered beaches. Sheltered beaches have been less well researched over the past decades than open sea coasts, while they make up a larger part of coastlines in the world. This begs the question of whether our current understanding of coastal processes is sufficient to understand the development of sheltered beaches. Further research indicated that was not the case, since models that were developed for the prediction of coastal development on open sea coasts, were not able to recreate measured coastal development of sheltered beaches. The reason for this inaccurate prediction was not directly identified, but an inaccurate coastal profile development must be the case of wrongly predicted sediment transport. One of the sources that could introduce uncertainty in sediment transport is the presence of rippled beds. The presence of a rippled bed is not taken into account in the models for open sea coasts, because during the high energy storms at open sea coasts, they are washed away. However, the low energetic wave climate at a sheltered beach creates an environment, where ripples can persist in the bed for longer periods. In this research, ripples were also present on the bed for significant periods of the research time series. Not taking these into account, while they have an impact on the sediment transport, discussed in chapter 3, could lead to wrong predictions in sediment fluxes.
If you want to take the presence of ripples into account, ripple predictors can be used to predict the presence and dimensions of ripples on the bed. There is a highly diverse collection of ripple predictors. This research has discussed three of these and tested their performance for the PHZD without adjusting them. Each of the predictors has a different definition of the mobility parameter that is best for the hydrodynamics concerning bed ripples. They are developed in different circumstances, for example, fieldwork or lab environment, different sediment classes, and regular or irregular waves. Overall, there is a consensus that the wave-orbital motion near the bed is the driving force behind ripple formation, but the differences between the setup of the different ripple predictors show the uncertainty that is currently still present in the literature.
This research has shown that directly applying a ripple predictor to a beach can lead to very large errors, see the KO-predictor in chapter 6, while this predictor performed well in their setup in the lab. Another predictor assumes a constant ripple height under a varying mobility number, while the third discussed predictor also uses the mobility number to predict varying ripple heights under varying hydrodynamic forcing. These last predictors by Van Rijn (2007) and O'Donoghue et al. (2006) respectively both have similar performance, while one assumes a constant height and the other a varying height. This demonstrates that currently, the best way to predict ripple dimensions might be assuming a constant height when it is determined that ripples are present and not trying to accurately predict changes in dimensions under varying conditions. Although there is still room for improvement, the RMSE of the best predictor was of the same order as the ripple height, it can be questioned whether it is possible to improve ripple prediction: Complex formulas that were developed using field data sets do not seem to perform for a different site, showing the high variety in ripple formation caused by circumstances that are left out of the formulation of the predictor. The predictors should be calibrated on a certain area with recent data before modeling.
An additional challenge in the understanding of ripple behavior is the migration of ripples. Current literature is limited to research on the understanding of driving mechanisms behind ripple migration. It can be questioned whether accurate ripple prediction together with migration prediction is a realistic goal. The current uncertainty of ripple prediction and the low relation between hydrodynamic parameters, the large point cloud in figure 6.1a and 6.1b, and the ripple dimensions, can support the argumentation that more accurate prediction is not attainable because ripples are simply not predictable enough.

Overall, there is a good understanding in the current literature of the formation of ripples. Ripples were expected to be present at the sheltered beaches very often, because of the lower energetic conditions and this was partly true. The formation of ripples takes time. This was very little discussed

in this research but has been researched in the past. The response time of ripples to changing hydrodynamic conditions was also not discussed, but it was shown that ripples responded to changing conditions on a timescale of less than an hour. This corresponds to recent research but could be looked into more. Also, this could shed light on the duration of the formation of ripples on the bed: How much time is necessary for ripples to form after sand grains have become mobile on the bed?
The prediction of ripples is still very uncertain, which suggests a lot of room for improvement. However, looking at the correlation between the ripple dimension and the mobility number there is serious doubt whether more improvement is possible. In the case of using the ripple predictors, especially those that incorporate a variable ripple height, they should be calibrated to the environment in which they are used. Moreover, the measured migration-induced sediment transport was of the same order as the predicted transport rates by XBeach. The model does not yet incorporate ripples and ripple migration, so the inclusion of bed load transport caused by migrating ripples could have a significant impact. Before this is possible, more understanding of migration rates related to hydrodynamic conditions is necessary, which than also requires a better understanding of ripple prediction. This all shows that research into sheltered beaches is necessary because different sediment transport mechanisms can be present at the beach than at open sea coasts. To accurately understand and predict coastline behavior under increasing loading due to climate change, a better understanding of these mechanisms is necessary.

# 8 | Conclusion

The measurements at the Prins Hendrikzanddijk have been carried out to answer the main research question of this report: "What is the behavior of bed ripples on sheltered beaches?". This research question has been divided into three sub-research questions with the following topics: the presence of ripples, ripple predictors, and ripple migration-induced sediment transport.

## 8.1 | Ripple presence

The first sub-question is: "Under which conditions do ripples appear at sheltered beaches and what are the dimensions?" To answer this question, the parameter that relates best to the ripples was determined. The presence of ripples on the beach has been related to three different formulations of the mobility parameter: $\psi_{w;max}$, $\psi_{VR}$, and $\psi_{KO}$. The first parameter does not take current velocity into account. It was found that the dimension of the ripples at the Prins Hendrikzanddijk responded best to this parameter, and no relation was found between a current-related mobility parameter and the dimension of ripples.
The occurrence of ripples related to the $\psi_{w;max}$ parameter was a threshold for $\psi_{w;max} = 100 - 200$ according to the literature. Above this threshold, the ripple regime is washed away by sheet flow. Where the exact threshold lies at the Prins Hendrikzanddijk was to be determined, since this limit was never reached during the measurements. This indicates, however, that ripples should always be present on the bed, but this was not the case. For very low mobility parameters no ripples were found either. Ripples can be formed by the wave orbital motion and need time to organize. This is a process that starts when sand grains become mobile. First small pockets of ridges are forged and eventually, longer crested ripples are formed on the bed. The most important takeaway was that the energy of the waves on the sheltered beach was energetic enough to form ripples, but also energetic enough for ripples to respond to changes in the forcing. High-energy events did not create the ripples for them to slowly dissipate, but ripples responded to the low-energetic waves by changing in dimension throughout the measurements.
The measured ripples during both of the campaigns had wave heights ranging from $\eta = 0.023$ to $0.078$ meters and the wavelength ranged from $\lambda = 0.091$ to $0.275$ meters.

## 8.2 | Ripple predictors

The second sub-question looked into the predictor formulas that can be used by models: "How accurate are existing ripple predictors for the wave-current regime at sheltered beaches?" Three ripple predictors have been investigated: O'Donoghue et al. (2006) (OD), Van Rijn (2007) (VR), and Khelifa and Ouellet (2000) (KO). It was previously concluded that the mobility parameter $\psi_{w;max}$ was most relatable to the ripple dimensions. This is the mobility parameter that is used in predictor OD. Therefore, it was also expected that this predictor formula would perform best when comparing predicted ripple dimensions with the measured ripple dimensions. This was indeed true. Without adjusting the formulas from the predictors, the order of performance for the ripple height was OD, VR, and KO. The order in the prediction of the ripple wavelength was OD over KO as well. Predictor VR does not include a formulation for the wavelength, so is not included in this comparison.
Since the current was proven to have less influence than assumed by the literature, an attempt was made to increase the accuracy of the KO predictor by excluding the current from their computation. This resulted in a new RMSE that was more than 2 times smaller than for the computation with the current for both the height and ripple wavelength.
All of the ripple predictors were tested without altering anything in their formulation. The fact that a ripple predictor that prescribes a constant ripple height, VR, performs similarly to a predictor that calculates a ripple height and length to the various conditions, shows the unpredictability of the ripples. Before using these ripple predictors, they should bed calibrated to the beach that they are used for and it should be considered that with the current understanding the method by VR looks

favorable.

## 8.3 | Ripple migration-induced sediment transport

The last sub-question that was investigated is: "What are the migration velocities and sediment transport rates of ripples on sheltered beaches?" Only during the SEDRIP campaign, ripple migration was measured. During the campaign, 5 sets of migration were noticed. In the literature, wave skewness is described as the driving mechanism behind ripple migration, which is indeed the case. During all of the migration sets, there was wave skewness.
The direction of the migration, off- or onshore was related to the severity of the wave skewness, asymmetry, and the Ursell number. When these parameters were smaller, the migration was offshore, and the migration was onshore when these were higher.
The measured sediment transport rates were of the order $10^{-6}$ $m^2/s$. Compared with XBeach the order was the same. However, XBeach mainly computed offshore bed load transport at the location of the frame. Looking broader at the entire cross-section, it is expected that the measured migration rates can take place over the entire sub-tidal plateau. Ripple migration was proven to be caused by wave skewness, which is a feature of waves entering shallow water. Since there is a large sub-tidal plateau on the sheltered beach it is expected that waves will be skewed over a large part of this plateau, causing ripple migration-induced bed load sediment transport on a large part of the cross-section.

## 8.4 | General

In general, ripple behavior is best characterized by a mobility number that only uses the maximum wave-orbital velocity near the bed. A clear threshold for ripple presence was not visible and the ripples needed time to build up once they had become mobile. The ripples' dimensions responded to changes in hydrodynamic conditions on the scale of hours. When ripples were present, the predictor by O'Donoghue et al. (2006) (OD) provided the best prediction for ripple height and wavelength. Ripple migration was present and is indeed driven by wave skewness. The associated sediment transport is comparable to a prediction by XBeach but is at some times directed onshore, while XBeach mainly predicts offshore transport.

# 9 | Recommendations

The conducted research has limitations that could be further investigated in future research. Also, missed opportunities during the SEDRIP campaign, such as a lack of sediment sampling, can be avoided in a new fieldwork trip. The most prominent limitations and future opportunities are discussed below.

## 9.1 | D50 verification

The D50 of the sediment was averaged over a set of measurements at the beach that were done in 2020 and 2021. Within this set the range of D50 was very large, 387.5 - 1752.0 $\mu m$. Firstly, the measurements for the SEDRIP campaign were done in November 2023. This is 2 years after the D50 measurements at the beach, so sediment conditions could have changed over this period. Verification of the sediment size during a next fieldwork campaign is advised. Secondly, because the sediment size was very dynamic over the different measurements in 2020 and 2021, it is advised that in a following campaign several sediment samples are taken during the campaign at the location of the frame.
The D50 has an impact on the performance of the ripple predictors and by using a wrong value for it a ripple predictor can be wrongly concluded to be bad. An accurate estimation of the D50 over the entire fieldwork campaign is advised.

## 9.2 | Lower SRPLS mounting

Migration was measured when wave skewness was present. However, during very low water, the skewness was highest. During these water levels, however, the SRPLS, was located above the waterline resulting in a lack of measurements at periods of most interest. The height of the SRPLS and the resulting diameter during the SEDRIP campaign were mainly based on the desire to have several wavelengths of a ripple inside of the footprint. Now that the ripple regime on the beach is known, the height of the SRPLS could be lower during a new deployment. The longest measured wavelength was 0.275 meters. A total footprint diameter to capture about two wavelengths would be 0.6 meters. If a total swath arc of 90 degrees is used, the required mounting height of the device would be 30 centimeters above the bed. At this height the SRPLS would have been submerged constantly during the SEDRIP campaign and almost constantly during the SEDMEX campaign, figures 5.1 and 5.2.

## 9.3 | Different migration measurement method

The migration was measured according to the method by Wengrove et al. (2017). A 2D cross-correlation was performed over two complete bed images. These bed images were constructed with sonar data collected over a 7.5 minute measurement time every 15 minutes. Bed form change during the 7.5 minutes of measuring are not taken into account. A different method could be used that is similar to the method used by Kalra et al. (2022).
Instead of using the entire footprint of the SRPLS, just the single swath measurement in the same direction of ripple orientation could be used. The full footprint is still used to determine the direction of migration and the orientation of the ripples. The correct swath then shows a cross section of the ripple profile. This measurement is taken much quicker. For example, the full measurement cycle took about 7.5 minutes. Within that time span 100 swaths were performed, so one swath takes about 4.5 seconds. By using two single swaths that are 15 minutes apart, you compare two measurements that have very little change within the a measurement. A 1D cross-correlation over the ripple profile of the cross-section then results in a migration that has only taken place within the 15 minutes in between the measurements and not within a longer measurement time of 7.5 minutes.

## 9.4 | Disturbance by the frame

Previously, it was discussed that the poles of the frame have an impact on the footprint below the SRPLS, see figure 7.2. If the same footprint is desired in future research, a different frame setup can be considered. Either a wider frame or a different frame setup, where the SRPLS is mounted on a cantilever could be considered. However, the last is undesirable, because the weight of the device in combination with additional hydrodynamic forcing will cause large forces on the structure. The wider frame seems a more reasonable option. Looking at figure 7.2, the impacted area around the west pole is about 20 to 30 centimeters. Poles that are placed about an additional 60 centimeters apart would be enough in this scenario to move the hump out of the footprint.
An implication that arises is the orientation determination of the SRPLS. The width of the frame was chosen based on the demand that the poles were just inside the footprint for the post-processing of the correct orientation of the bed image. When the poles are placed further apart, they will not be visible in the footprint. Placing additional poles inside the footprint during the first hours of the measurements and removing them a tidal cycle later could be done in this case. These could be used in the post-processing to determine the correct rotation of the device. If the device is retrieved during the measurement campaign this step needs to be done again after reinstalling the device.

## 9.5 | Additional measurements over the cross-section

A sheltered beach has a characterizing beach profile with a large sub-tidal plateau. In the conclusion it was already discussed that this plateau could mean that there is ripple migration over a substantial part of the beach profile. The behaviour of ripples on the Prins Hendrikzanddijk has now been investigated at a single location on the cross-section. The hypothesis that ripple migration is present on a larger part of the cross-section can only be proven by conducting measurements on a larger part of the cross-section. This implies that in the future frames must be installed further offshore, to measure the ripples and hydrodynamic conditions. The installation of the frame for the SEDRIP campaign was already done at the deepest point on the beach profile possible at the time. A deeper installation of the frame on the sub-tidal plateau would be more costly since different machinery would be used. A cheaper option would be to first do a study where only ADVs are installed at deeper points of the sub-tidal plateau. They could measure the wave skewness at these locations to identify whether waves are indeed skewed over a large part of the plateau. Without the presence of skewness, ripple migration is not expected.

# References


Bagnold, R. A., & Taylor, G. I. (1946). Motion of waves in shallow water. interaction between waves and sand bottoms. *Proceedings of the Royal Society of London. Series A. Mathematical and Physical Sciences*, *187*(1008), 1–18. https://doi.org/doi:10.1098/rspa.1946.0062

Bosboom, J., & Stive, M. J. F. (2023). *Coastal dynamics 1*. TU Delft. https://doi.org/10.5074/T.2021.001

Brakenhoff, L., Schrijvershof, R., van der Werf, J., Grasmeijer, B., Ruessink, G., & van der Vegt, M. (2020). From ripples to large-scale sand transport: The effects of bedform-related roughness on hydrodynamics and sediment transport patterns in delft3d. *Journal of Marine Science and Engineering*, *8*(11), 892. https://www.mdpi.com/2077-1312/8/11/892

Cooper, J. A. G., Pilkey, O. H., & Lewis, D. A. (2007). Islands behind islands an unappreciated coastal landform category. *Journal of Coastal Research*, 907–911. http://www.jstor.org/stable/26481711

Crawford, A. M., & Hay, A. E. (2001). Linear transition ripple migration and wave orbital velocity skewness: Observations. *Journal of Geophysical Research: Oceans*, *106*(C7), 14113–14128. https://doi.org/https://doi.org/10.1029/2000JC000612

Duffy, G. P., & Hughes-Clarke, J. E. (2005). Application of spatial cross correlation to detection of migration of submarine sand dunes. *Journal of Geophysical Research: Earth Surface*, *110*(F4). https://doi.org/https://doi.org/10.1029/2004JF000192

Google Earth. (2023). http://www.google.com/earth/index.html

Holthuijsen, L. H. (2007). *Waves in oceanic and coastal waters*. Cambridge University Press. https://doi.org/10.1017/CBO9780511618536

Hurther, D., & Thorne, P. D. (2011). Suspension and near-bed load sediment transport processes above a migrating, sand-rippled bed under shoaling waves. *Journal of Geophysical Research: Oceans*, *116*(C7). https://doi.org/https://doi.org/10.1029/2010JC006774

Jackson, N. L., Nordstrom, K. F., Eliot, I., & Masselink, G. (2002). 'low energy' sandy beaches in marine and estuarine environments: A review. *Geomorphology*, *48*(1), 147–162. https://doi.org/https://doi.org/10.1016/S0169-555X(02)00179-4

Kalra, T. S., Suttles, S. E., Sherwood, C. R., Warner, J. C., Aretxabaleta, A. L., & Leavitt, G. R. (2022). Shoaling wave shape estimates from field observations and derived bedload sediment rates. *Journal of Marine Science and Engineering*, *10*(2), 223. https://www.mdpi.com/2077-1312/10/2/223

Khelifa, A., & Ouellet, Y. (2000). Prediction of sand ripple geometry under waves and currents. *Journal of Waterway, Port, Coastal, and Ocean Engineering*, *126*(1), 14–22. https://doi.org/doi:10.1061/(ASCE)0733-950X(2000)126:1(14)

KNMI. (2023). Storm ciarán. Retrieved April 29, 2024, from https://www.knmi.nl/over-het-knmi/nieuws/storm-ciaran

Marine Electronics. (2009). *User manual for the 3d sand ripple profiling logging sonar* (Report). http://www.marine-electronics.co.uk/Manuals/3DLogging%20OM.pdf

McCall, R., Van der Lugt, M., Gawehn, M., & Vuik, V. (2018). Aanvullende metingen en modelering pilot houtribdijk.

Nordstrom, K. F., & Jackson, N. L. (2012). Physical processes and landforms on beaches in short fetch environments in estuaries, small lakes and reservoirs: A review. *Earth-Science Reviews*, *111*(1), 232–247. https://doi.org/https://doi.org/10.1016/j.earscirev.2011.12.004

Nortek Group. (2023). *Vector - 300m* (Report). Nortek Group. https://www.nortekgroup.com/products/vector-300-m/pdf

O'Donoghue, T., Doucette, J. S., van der Werf, J. J., & Ribberink, J. S. (2006). The dimensions of sand ripples in full-scale oscillatory flows. *Coastal Engineering*, *53*(12), 997–1012. https://doi.org/https://doi.org/10.1016/j.coastaleng.2006.06.008

Perk, L., van Rijn, L., Koudstaal, K., & Fordeyn, J. (2019). A rational method for the design of sand dike/dune systems at sheltered sites; wadden sea coast of texel, the netherlands. *Journal of Marine Science and Engineering*, *7*(9), 324. https://www.mdpi.com/2077-1312/7/9/324

Plant, N. G., Holland, K. T., & Puleo, J. A. (2002). Analysis of the scale of errors in nearshore bathymetric data. *Marine Geology*, *191*(1), 71–86. https://doi.org/https://doi.org/10.1016/S0025-3227(02)00497-8

Ribberink, J. S., van der Werf, J. J., O'Donoghue, T., & Hassan, W. N. M. (2008). Sand motion induced by oscillatory flows: Sheet flow and vortex ripples [doi: 10.1080/14685240802220009]. *Journal of Turbulence*, *9*(null), N20. https://doi.org/10.1080/14685240802220009

Rijn, L. C. v. (1984). Sediment transport, part iii: Bed forms and alluvial roughness. *Journal of Hydraulic Engineering*, *110*(12), 1733–1754. https://doi.org/doi:10.1061/(ASCE)0733-9429(1984)110:12(1733)

Rijn, L. C. V., Nieuwjaar, M. W. C., Kaay, T. v. d., Nap, E., & Kampen, A. v. (1993). Transport of fine sands by currents and waves. *Journal of Waterway, Port, Coastal, and Ocean Engineering*, *119*(2), 123–143. https://doi.org/doi:10.1061/(ASCE)0733-950X(1993)119:2(123)

Roelvink, D., Reiniers, A., van Dongeren, A., van Thiel de Vries, J., Lescinski, J., & McCall, R. (2010). *Xbeach model description and manual* (Report). Unesco-IHE Institute for Water Education, Deltares, Delft University of Technology. https://doi.org/1200116/1002266

Ruessink, G., Brinkkemper, J. A., & Kleinhans, M. G. (2015). Geometry of wave-formed orbital ripples in coarse sand. *Journal of Marine Science and Engineering*, *3*(4), 1568–1594. https://www.mdpi.com/2077-1312/3/4/1568

Soulsby, R. (1997). Dynamics of marine sands.

Travers, A. (2007). Low-energy beach morphology with respect to physical setting: A case study from cockburn sound, southwestern australia. *Journal of Coastal Research*, *232*, 429–444. https://doi.org/10.2112/04-0275.1

Traykovski, P. (2007). Observations of wave orbital scale ripples and a nonequilibrium time-dependent model. *Journal of Geophysical Research: Oceans*, *112*(C6). https://doi.org/10.1029/2006jc003811

Traykovski, P., Hay, A. E., Irish, J. D., & Lynch, J. F. (1999). Geometry, migration, and evolution of wave orbital ripples at leo-15. *Journal of Geophysical Research: Oceans*, *104*(C1), 1505–1524. https://doi.org/10.1029/1998jc900026

Van der Lugt, M. A., Bosma, J. W., de Schipper, M. A., Price, T. D., van Maarseveen, M. C. G., van der Gaag, P., Ruessink, G., Reniers, A. J. H. M., & Aarninkhof, S. G. J. (2024). Measurements of morphodynamics of a sheltered beach along the dutch wadden sea [ESSD]. *Earth Syst. Sci. Data*, *16*(2), 903–918. https://doi.org/10.5194/essd-16-903-2024

Van Rijn, L. C. (2007). Unified view of sediment transport by currents and waves. i: Initiation of motion, bed roughness, and bed-load transport. *Journal of Hydraulic Engineering*, *133*(6), 649–667. https://doi.org/doi:10.1061/(ASCE)0733-9429(2007)133:6(649)

Van Thiel de Vries, J. (2009). *Dune erosion during storm surges* [Thesis]. http://resolver.tudelft.nl/uuid:885bf4b3-711e-41d4-98a4-67fc700461ff

Vila-Concejo, A., Gallop, S. L., & Largier, J. L. (2020). Sandy beaches in estuaries and bays. In D. W. T. Jackson & A. D. Short (Eds.), *Sandy beach morphodynamics* (pp. 343–362). Elsevier. https://doi.org/10.1016/B978-0-08-102927-5.00015-1

Vila-Concejo, A., Hughes, M. G., Short, A. D., & Ranasinghe, R. (2010). Estuarine shoreline processes in a dynamic low-energy system. *Ocean Dynamics*, *60*(2), 285–298. https://doi.org/10.1007/s10236-010-0273-7

Wengrove, M. E., Foster, D. L., Lippmann, T. C., de Schipper, M. A., & Calantoni, J. (2018). Observations of time-dependent bedform transformation in combined wave-current flows. *Journal of Geophysical Research: Oceans*, *123*(10), 7581–7598. https://doi.org/https://doi.org/10.1029/2018JC014357

Wengrove, M. E., Foster, D. L., de Schipper, M. A., & Lippmann, T. C. (2017). Wave and current ripple formation and migration during storms. *Proceedings of Coastal Dynamics*, *129*, 955–965.

Young, I. R., & Verhagen, L. A. (1996). The growth of fetch limited waves in water of finite depth. part 1. total energy and peak frequency. *Coastal Engineering*, *29*(1), 47–78. https://doi.org/https://doi.org/10.1016/S0378-3839(96)00006-3

# A | Additional relations between hydrodynamics and bed ripples

Apart from the ones in chapter 6, other relations between the presence/behavior of bed ripples and hydrodynamic conditions have been investigated, but have not been found to have a visible correlation. The following figures show the scatter plots of these additional variables:

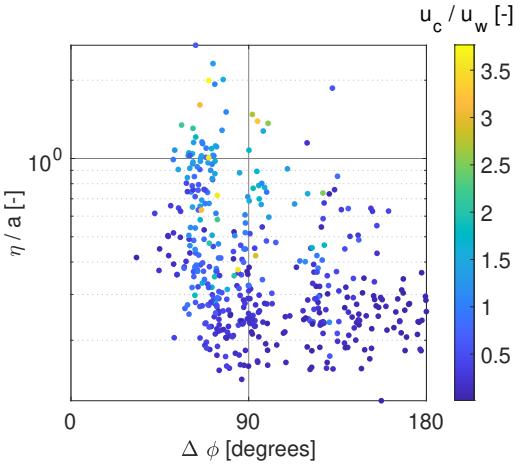


**(a)** The relation for the dimensionless ripple height.

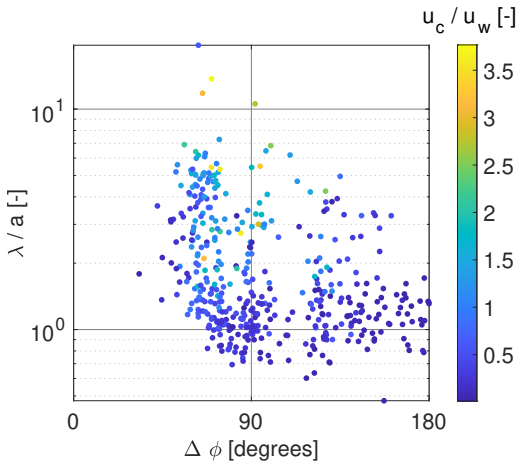


**(b)** The relation for the dimensionless ripple wavelength.

**Figure A.1:** The angle between the current and wave-orbital direction is compared with the dimensionless ripple geometries.

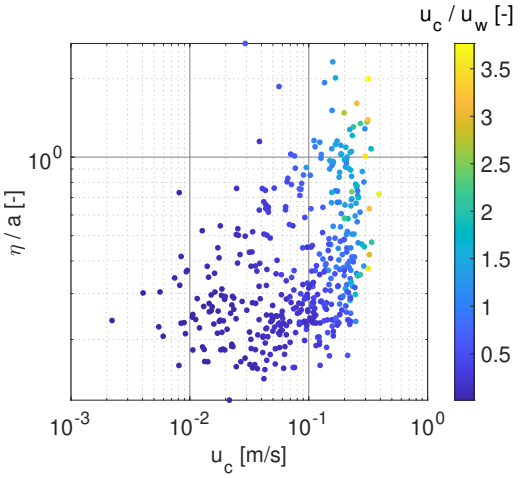


**(a)** Current velocity against the dimensionless ripple height

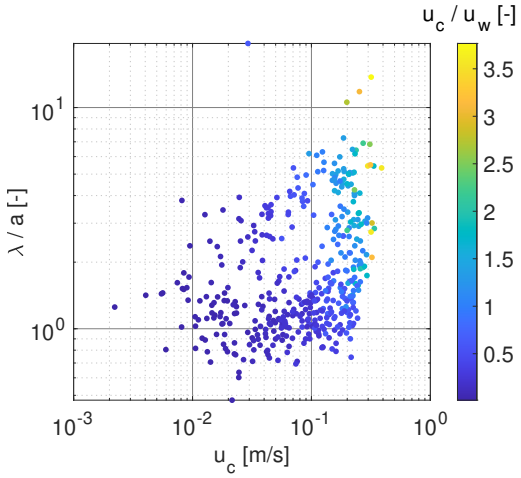


**(b)** Current velocity against the dimensionless wavelength

**Figure A.2:** Dimensionless ripple geometry for the current velocity and color graded for the current-wave-orbital velocity fraction.

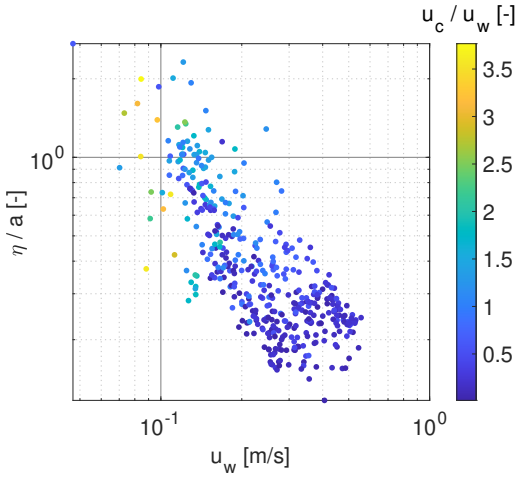


(a) Wave-orbital velocity against the dimensionless ripple height

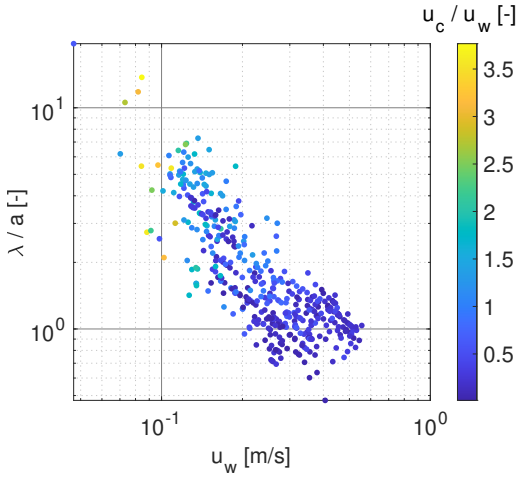


(b) Wave-orbital velocity against the dimensionless wavelength

**Figure A.3:** Dimensionless ripple geometry for the wave-orbital velocity and color graded for the current-wave-orbital velocity fraction.

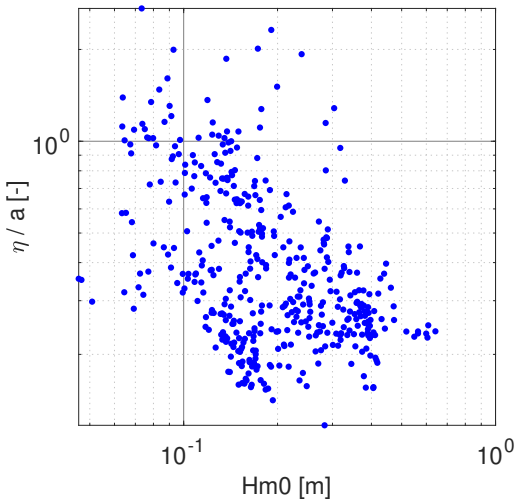


(a) Dimensionless ripple height

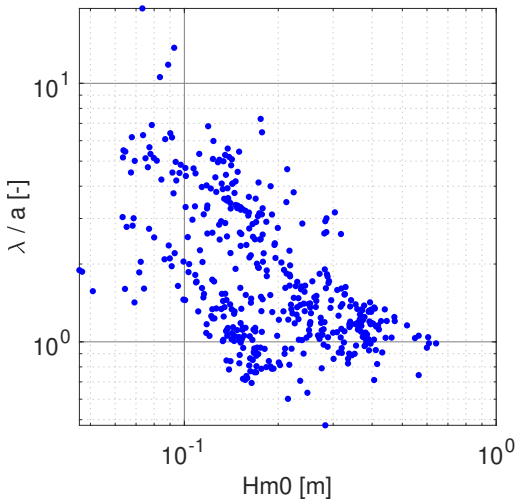


(b) Dimensionless wave length

**Figure A.4:** Dimensionless ripple geometry for the wave-orbital velocity

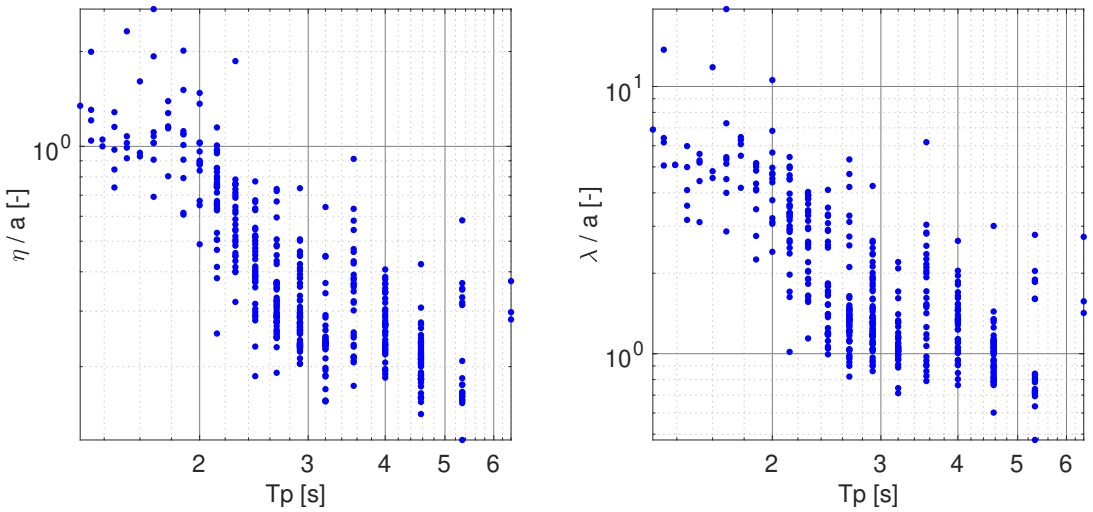


**(a)** Dimensionless ripple height **(b)** Dimensionless wave length

**Figure A.5:** Dimensionless ripple geometry for the peak period.

# B | Ripple predicted time series

This appendix shows an overview of predicted ripple dimensions and corresponding parameters for the entire measurement series.

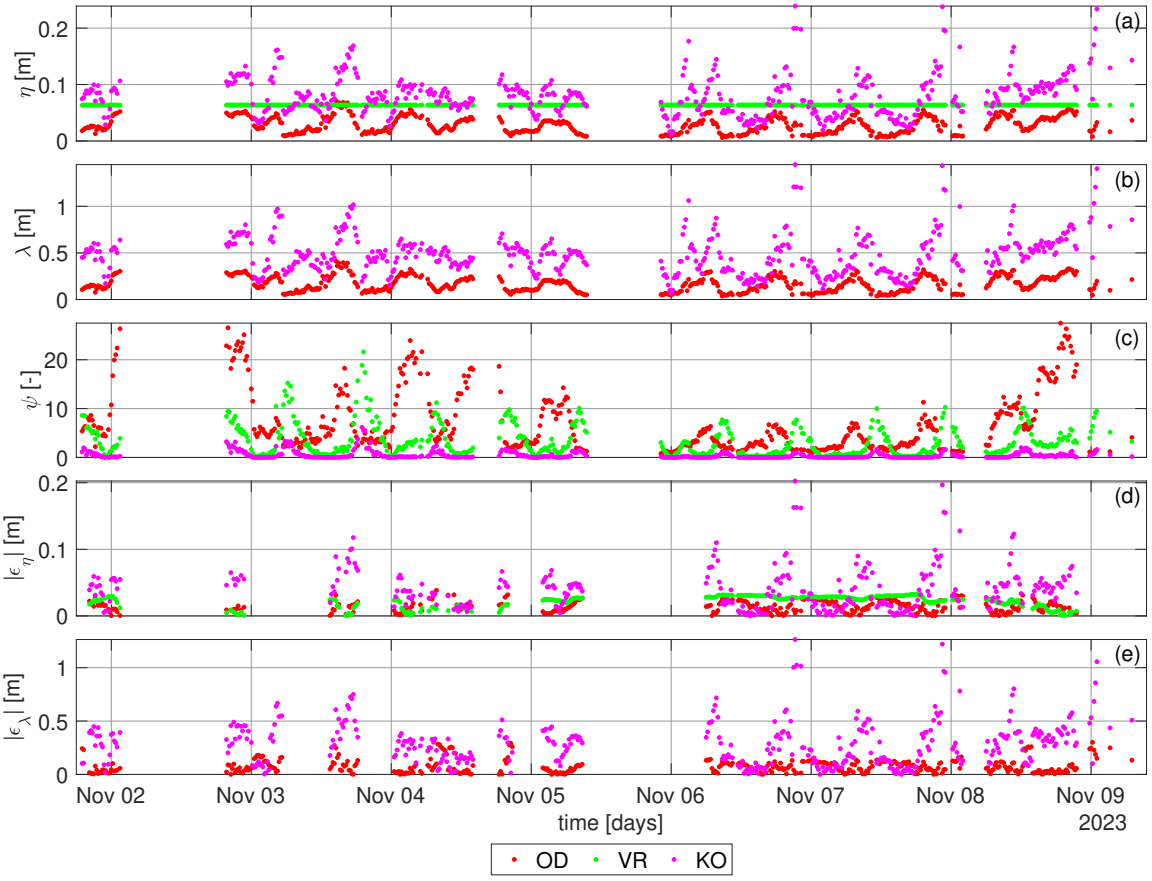

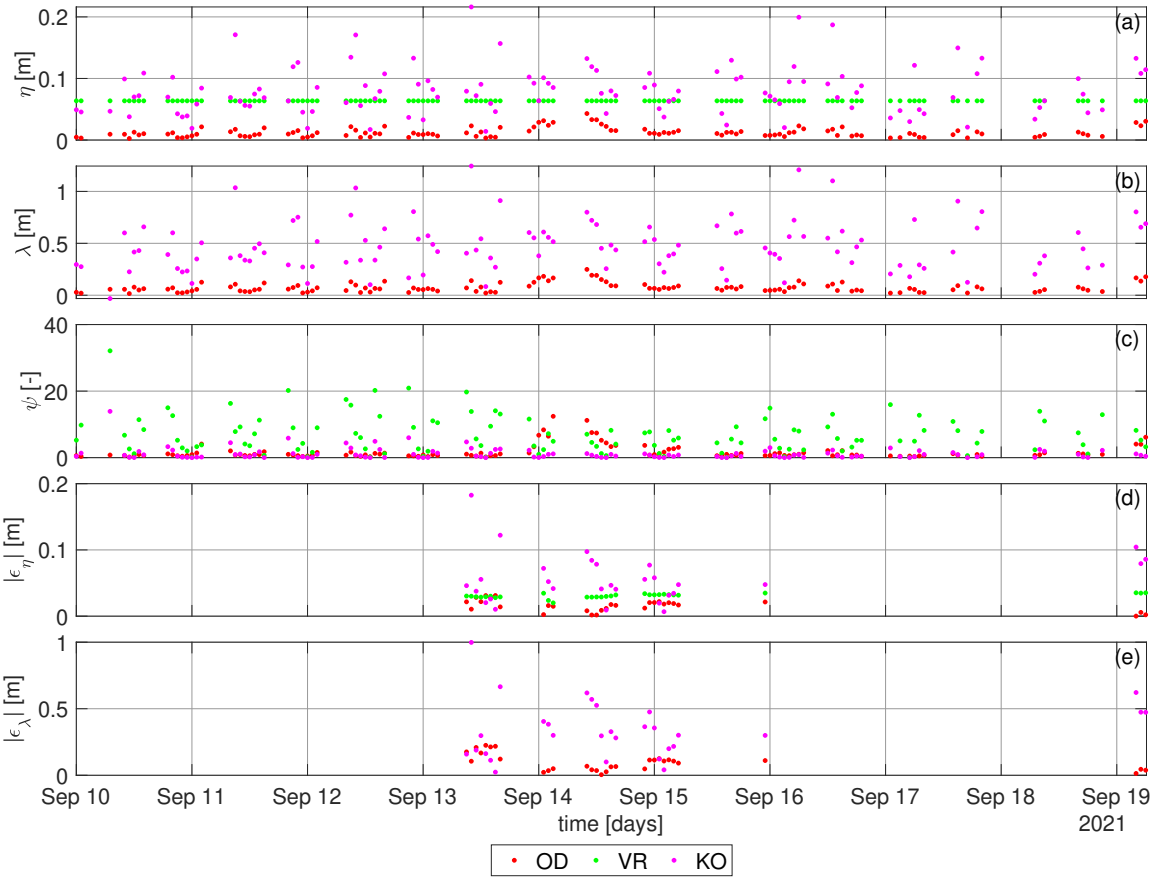
(a)
(b)
(c)
(d)
(e)
$\eta$ [m]
$\lambda$ [m]
$\psi$ [-]
$|\epsilon_\eta|$ [m]
$|\epsilon_\lambda|$ [m]
0.2
0.1
0
1
0.5
40
20
Sep 10
Sep 11
Sep 12
Sep 13
Sep 14
Sep 15
Sep 16
Sep 17
Sep 18
Sep 19
2021
time [days]
OD
VR
KO

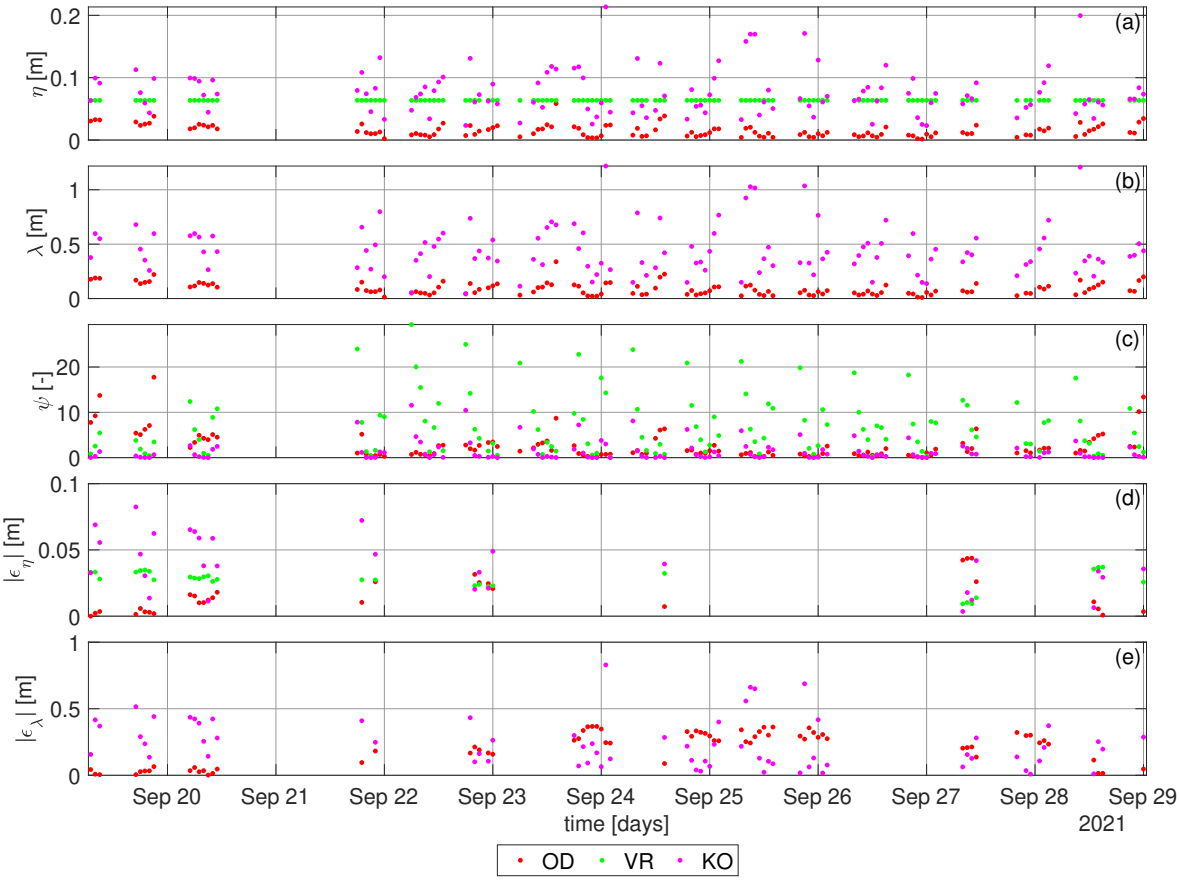
(a)
(b)
(c)
(d)
(e)
$\eta$ [m]
$\lambda$ [m]
$\psi$ [-]
$|\epsilon_\eta|$ [m]
$|\epsilon_\lambda|$ [m]
Sep 20
Sep 21
Sep 22
Sep 23
Sep 24
Sep 25
Sep 26
Sep 27
Sep 28
Sep 29
2021
time [days]
OD
VR
KO

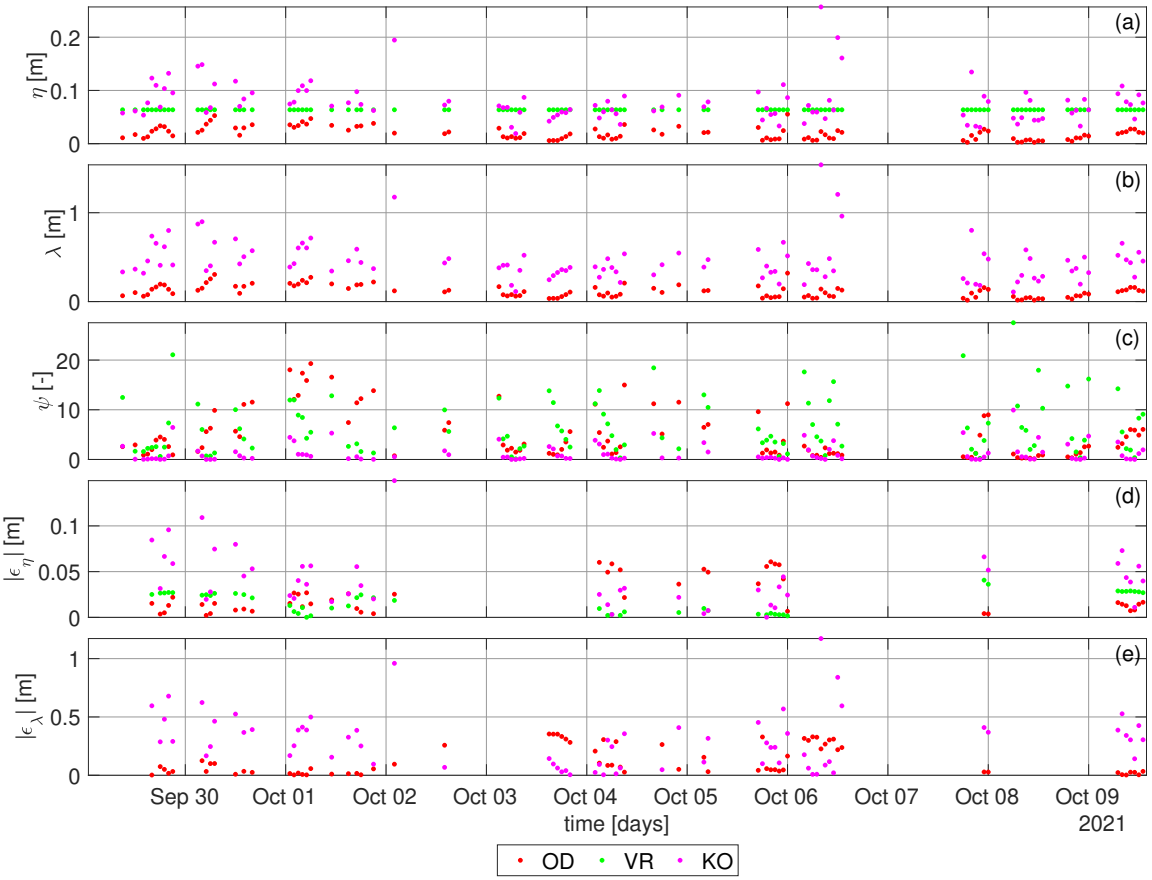
(a)
$\eta$ [m]
0.2
0.1
0
(b)
$\lambda$ [m]
1
0
(c)
$\psi$ [-]
20
10
0
(d)
$|\epsilon_\eta|$ [m]
0.1
0.05
0
(e)
$|\epsilon_\lambda|$ [m]
1
0.5
0
Sep 30
Oct 01
Oct 02
Oct 03
Oct 04
Oct 05
Oct 06
Oct 07
Oct 08
Oct 09
2021
time [days]
OD
VR
KO

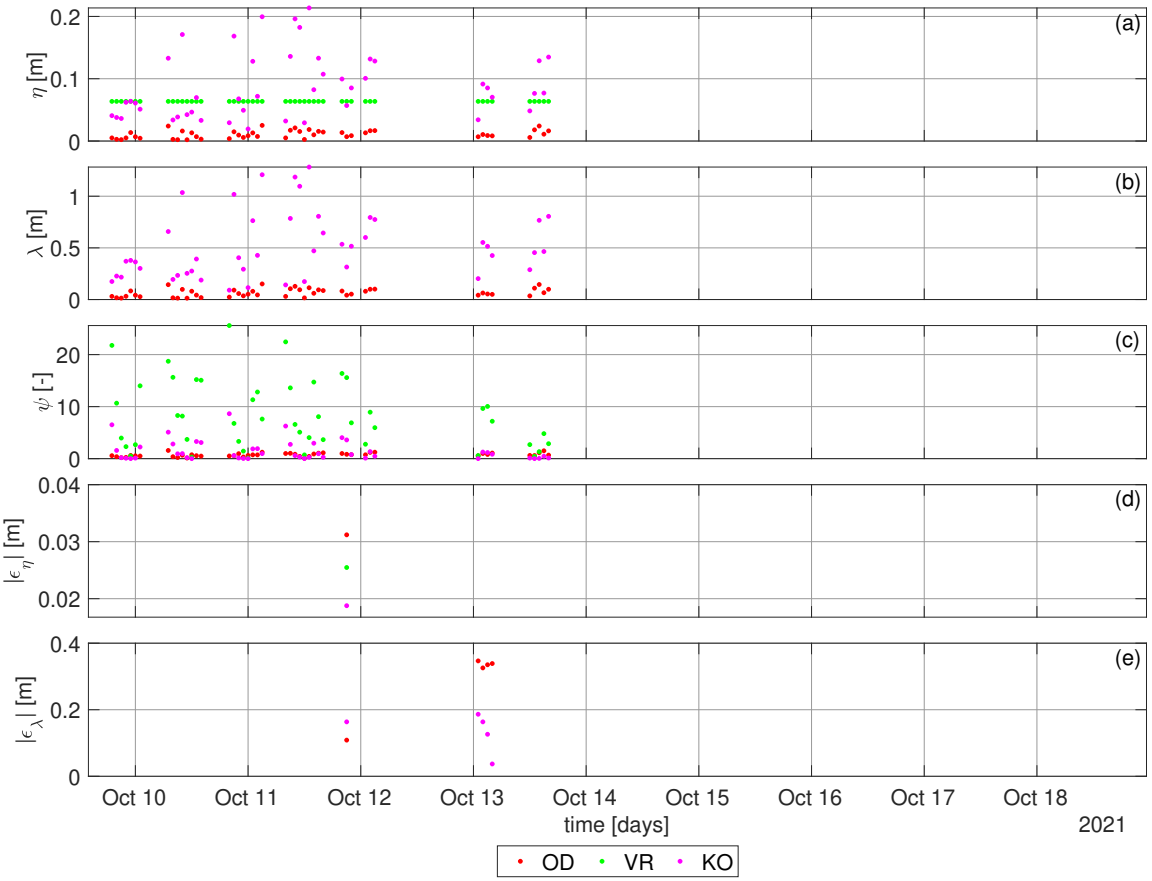


**Figure B.0:** Time series of the ripple predictors

# C | Cross-correlation procedure

In a cross-correlation, you compare a matrix, X(N by N), with another matrix, Y(M by M). The cross-correlation determines where matrix X will fit best over matrix Y. The cross-correlation is defined as (Duffy & Hughes-Clarke, 2005):

$$\begin{aligned} G &= X \otimes Y \\ G[i,j] &= \sum_{u=-k}^{k} \sum_{v=-k}^{k} X[u,v] Y[i+u, j+v] \\ \text{with: } k &= (N-1)/2 \end{aligned} \tag{C.1}$$

Here, i and j, are the column and row positions over the original matrix Y. Indexing of the matrices for cross-correlation ranges from -k to k. So, with 21 columns and rows, the left upper cell is [-10, -10]. To explain the cross-correlation, figure C.1 represents fictive matrices X and Y and in this cross-correlation step, what is determined is the cross-correlation value for the fit of the green matrix, X, over the blue matrix, Y, so that the origin of X aligns with the red cell of matrix Y. The value for this correlation is the sum of all the products of overlapping matrix elements:

$$5 \times 3 + 12 \times 4 + 1 \times 8 + 10 \times 1 + 4 \times 10 + 7 \times 7 + 13 \times 8 + 8 \times 5 + 9 \times 2 = 332 \tag{C.2}$$

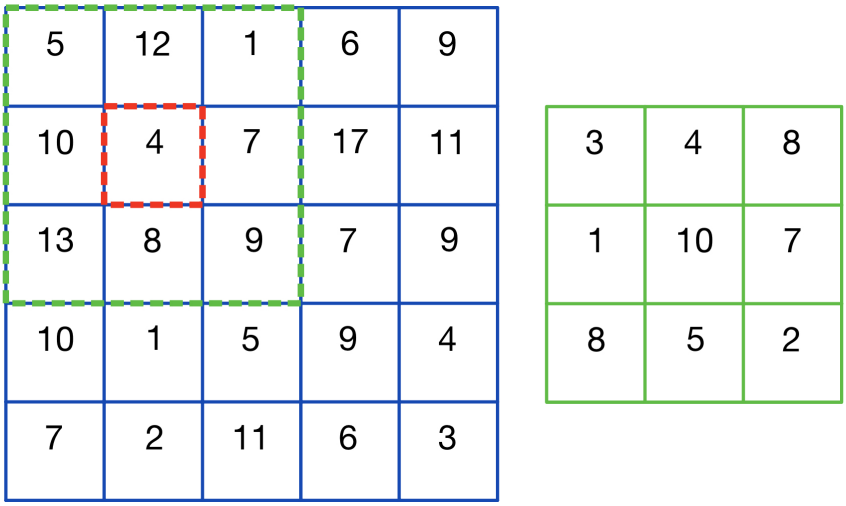


**Figure C.1:** Two random matrices. The green (right) matrix represents matrix X and the blue (left) matrix represents matrix Y.

In a full cross-correlation, this is done for every possible position of matrix X over matrix Y. For matrices of size $(N$ by $N)$ and $(M$ by $M)$ this would result in a cross-correlation matrix with size $(N+M-1$ by $N+M-1)$. This can also be applied to the bed images of figure 4.15. Take a bed image with time $t$, T0, and one with $t+\Delta t$, T1. If a cross-correlation is performed where image T0 fits best over T1, the result is a cross-correlation matrix, where the cells represent the cross-correlation value of the position for the origin of matrix T0 over T1. The highest value is the position for which the ripples align best, since this would yield the highest value for a calculation as in formula C.1.